

AD _____

Award Number: DAMD17-99-1-9034

TITLE: Ultrasound Imaging Initiative

PRINCIPAL INVESTIGATOR: J. Frederick Cornhill, Ph.D.

CONTRACTING ORGANIZATION: The Cleveland Clinic Foundation
Cleveland, Ohio 44195

REPORT DATE: January 2000

TYPE OF REPORT: Annual

PREPARED FOR: U.S. Army Medical Research and Materiel Command
Fort Detrick, Maryland 21702-5012

DISTRIBUTION STATEMENT: Approved for public release;
distribution unlimited

The views, opinions and/or findings contained in this report are
those of the author(s) and should not be construed as an official
Department of the Army position, policy or decision unless so
designated by other documentation.

20000328 047

REPORT DOCUMENTATION PAGE

Form Approved
OMB No. 074-0188

Public reporting burden for this collection of information is estimated to average 1 hour per response, including the time for reviewing instructions, searching existing data sources, gathering and maintaining the data needed, and completing and reviewing this collection of information. Send comments regarding this burden estimate or any other aspect of this collection of information, including suggestions for reducing this burden to Washington Headquarters Services, Directorate for Information Operations and Reports, 1215 Jefferson Davis Highway, Suite 1204, Arlington, VA 22202-4302, and to the Office of Management and Budget, Paperwork Reduction Project (0704-0188), Washington, DC 20503

1. AGENCY USE ONLY (Leave blank)	2. REPORT DATE	3. REPORT TYPE AND DATES COVERED	
	January 2000	Annual (21 Dec 98 - 20 Dec 99)	
4. TITLE AND SUBTITLE			5. FUNDING NUMBERS
Ultrasound Imaging Initiative			DAMD17-99-1-9034
6. AUTHOR(S)			
J. Frederick Cornhill, Ph.D.			
7. PERFORMING ORGANIZATION NAME(S) AND ADDRESS(ES)			8. PERFORMING ORGANIZATION REPORT NUMBER
The Cleveland Clinic Foundation Cleveland, Ohio 44195			
E-MAIL: cornhill@bme.ri.ccf.org			
9. SPONSORING / MONITORING AGENCY NAME(S) AND ADDRESS(ES)			10. SPONSORING / MONITORING AGENCY REPORT NUMBER
U.S. Army Medical Research and Materiel Command Fort Detrick, Maryland 21702-5012			
11. SUPPLEMENTARY NOTES			
12a. DISTRIBUTION / AVAILABILITY STATEMENT			12b. DISTRIBUTION CODE
Approved for public release; distribution unlimited			
13. ABSTRACT (Maximum 200 Words)			
<p>This objective of this project is to build a real-time 3-D ultrasound imaging system for combat casualty care. The high frame rate necessary for real-time 3-D imaging is obtained using a synthetic aperture beamforming technique. The technique uses a fraction of the transmit pulses required by a conventional imaging system and permits very rapid image acquisition with no degradation of image quality. A network of high speed digital signal processors is currently being designed to implement the beamformer. A new transducer technology is also being explored for the transducer array. This technology should permit a 25-fold increase in the acoustic power delivered by a single array element without a corresponding increase in the excitation voltage. The array will be incorporated into a compact probe head designed to rock the array for real-time 3-D imaging. Besides the scanner development, an extensive set of software tools are being developed to provide easy and accurate analysis of the resulting 3-D data. These tools will allow real-time viewing of arbitrary two-dimensional planes through the data set and will allow quantitative assessment and display of the three-dimensional anatomy.</p>			
14. SUBJECT TERMS			15. NUMBER OF PAGES
Ultrasound, 3-D Imaging, Image Processing, Synthetic Aperture			78
			16. PRICE CODE
17. SECURITY CLASSIFICATION OF REPORT	18. SECURITY CLASSIFICATION OF THIS PAGE	19. SECURITY CLASSIFICATION OF ABSTRACT	20. LIMITATION OF ABSTRACT
Unclassified	Unclassified	Unclassified	Unlimited

NSN 7540-01-280-5500

Standard Form 298 (Rev. 2-89)
Prescribed by ANSI Std. Z39-18
298-102

FOREWORD

Opinions, interpretations, conclusions and recommendations are those of the author and are not necessarily endorsed by the U.S. Army.

Where copyrighted material is quoted, permission has been obtained to use such material.

Where material from documents designated for limited distribution is quoted, permission has been obtained to use the material.

Citations of commercial organizations and trade names in this report do not constitute an official Department of Army endorsement or approval of the products or services of these organizations.

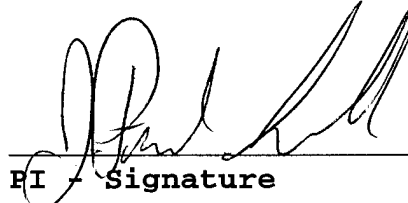
In conducting research using animals, the investigator(s) adhered to the "Guide for the Care and Use of Laboratory Animals," prepared by the Committee on Care and use of Laboratory Animals of the Institute of Laboratory Resources, national Research Council (NIH Publication No. 86-23, Revised 1985).

For the protection of human subjects, the investigator(s) adhered to policies of applicable Federal Law 45 CFR 46.

In conducting research utilizing recombinant DNA technology, the investigator(s) adhered to current guidelines promulgated by the National Institutes of Health.

In the conduct of research utilizing recombinant DNA, the investigator(s) adhered to the NIH Guidelines for Research Involving Recombinant DNA Molecules.

N/A In the conduct of research involving hazardous organisms, the investigator(s) adhered to the CDC-NIH Guide for Biosafety in Microbiological and Biomedical Laboratories.



PI - Signature _____ Date _____

TABLE OF CONTENTS

(1)	FRONT COVER	1
(2)	SF-298	2
(3)	FOREWORD	3
(4)	TABLE OF CONTENTS	4
(5)	INTRODUCTION	5
(6)	BODY	6
(7)	KEY RESEARCH ACCOMPLISHMENT.....	9
(8)	REPORTABLE OUTCOMES	9
(9)	CONCLUSIONS	10
(10)	REFERENCES	11
(11)	APPENDICES	12

INTRODUCTION

Providing accurate medical imaging at an aid station or remote field hospital is difficult. Portable ultrasound instrumentation can be designed for these applications, but the expertise required for an accurate diagnosis can only be obtained through years of training. Much of the information in an ultrasound examination is obtained by exploiting the real-time nature of the imaging modality. A successful diagnosis relies on the skill of the diagnostician to transform mentally dynamic 2-D images into the complex 3-D anatomy. Locating anatomical landmarks and moving the scan plane throughout the volume of interest are both critical components of this process. Without extensive training, it would be difficult for a medical corpsman to perform this procedure.

Researchers have started exploring tele-medicine in combination with three-dimensional (3-D) ultrasound data acquisition as a solution to this problem. This combination could potentially transfer the skill required to scan the patient and make the diagnosis from a medical corpsman to an imaging expert. Unfortunately, acquiring a 3-D ultrasound data set is difficult. Modern 3-D ultrasound systems are essentially conventional scanners modified to collect a series of 2-D images. The images are later 'stacked' to represent the 3-D anatomy. Although modern scanners are designed to collect 2-D images in real-time (20 2-D images/s), 3-D image acquisition is slow. Slow image acquisition introduces the problem of how to align adjacent 2-D images collected at different times. The patient and imaging probe can be immobilized to reduce movement of the anatomy between adjacent images. Cardiac and respiratory gating can also be applied. Even in a carefully controlled clinical setting, the resulting 3-D data set is often badly distorted. If the patient, the anatomy, or the transducer moves during 3-D image acquisition, the data must be discarded. Providing the care needed to obtain 'good' 3-D data in the clinic is troublesome, on a battlefield it would be very difficult.

We are building an ultrasound imaging system that would avoid these problems. The two key components of our system are the following: 1) a high speed scanner that can collect 3-D data 40 to 80 times faster than current 3-D imaging approaches, and 2) a set of software tools for rapid image manipulation and analysis at a remote site. Real-time 3-D image acquisition eliminates the need for patient immobilization, and cardiac and respiratory gating. A medical corpsman would simply place a small probe on the patient and position the sample volume by viewing a real-time two-dimensional image of the anatomy. Once the probe is correctly placed, a three-dimensional data set would be recorded in real-time (0.05 s for each 3-D data set). Following data acquisition, the images would be transmitted to a central hospital for post-processing and analysis. An expert clinician could 're-scan' the patient by looking at multiple 2-D planes through the data sets, or examine a computer reconstruction of the three-dimensional anatomy. The 3-D data set could also be analyzed quantitatively to calculate dynamic and/or anatomic changes in the anatomy. The entire imaging procedure, including subject preparation, would take only a few minutes.

BODY

The Statement of Work and a description of progress in each area is given below:

Phase I : Month 1 - 6

Scanner/Array Development:

- System specification - Perform a computer simulation to evaluate the radiation pattern and imaging performance of different array designs and beamforming strategies. Based on these results derive specifications for each component of the system.

COMPLETED - This work is described in the publication: "Theoretical Assessment of a Synthetic Aperture Beamformer for Real-Time 3-D Imaging", C.R. Hazard and G.R. Lockwood, IEEE Transactions on Ultrasonics, Ferroelectrics and Frequency Control, Vol. 4, pp. 972-979, 1999. (see Appendix 1)

- DSP boards - Place order with Pentek Inc. for multi processor DSP + A/D boards.

COMPLETED - The order was placed 03/25/99

- Transmit electronics - Preliminary design study for high voltage transmit circuit.

NOT COMPLETED - The specifications for the transmit circuits will be determined by the transducer technology (multi-layer vs. single layer). A decision on the transducer technology is expected in January 2000.

- Receive electronics - Preliminary design study for front end electronics (pre-amplifier, time-gain-compensation circuit and anti-aliasing filter).

COMPLETED - This work is described in a Masters Thesis by Kurtis Swinehart, "Signal Conditioning for Real-Time Three-Dimensional Echocardiography" Chapters 3-4, Case Western Reserve University, August, 1999. (see Appendix 2)

The following tasks were assigned to Tetrad Corporation under a subcontract. The subcontract was awarded 08/18/99. A report describing Tetrad's initial progress on this phase of the work was submitted in October, 99. A copy of this report is included in Appendix 3.

- Transducer development - Develop methods for dicing the stacked transducer and making interconnections.
- Verification of acoustic output capability- Build a transducer array (several elements) and test output power.
- Phased array performance optimization - Use finite element and 1-D transmission line models in conjunction with partial arrays to optimize the array design (matching layers,

- backing, cut geometry, kerf filler, lens).
- Mechanical probe design - Preliminary design of mechanical probe, identify risk areas in mechanical sector scanner and perform analysis experiments to assure the required performance can be met. This will include power and force requirements, rear seal termination method, acoustic window and fluid.
- Array interconnection - Choose a method for connecting the array elements to the cable that can be easily packaged and will tolerate a large number of oscillations at 10 Hz. Test and verify approached with bench testing.

User Interface & Image Processing Software:

- Develop general GUI with 2D and 3D interactive displays.

COMPLETED - A GUI for the display of ultrasound data was created using Tcl/Tk, Togl, C/C++ and OpenGL computer languages and toolkits. The source of the 3D ultrasound images has been Volumetrics, Inc.'s 3D ultrasound scanner located in the Department of Cardiology at the Cleveland Clinic Foundation. The choice of the programming languages and toolkits makes the GUI cross-platform. New controls will be added to this GUI to incorporate new processing features.

- Develop viewing tool for 3D ultrasound images.

COMPLETED - Multi Planar Reformatting (MPR) is one of the most common modes of viewing three and higher dimensional data. The MPR for viewing of volume data has been implemented.

- Apply texture mapping to allow interactive panning through image volumes.

COMPLETED -The above-stated MPR viewing mode requires computationally intensive trilinear interpolation of native data samples. Texture mapping is a hardware-accelerated approach to performing fast trilinear interpolation. The MPR viewing mode has been implemented using texture mapping.

Phase II: Month 7 - 12

Scanner/Array Development:

- Beamformer - configure DSP boards and write and test assembly language code for single channel.

COMPLETED - The configuration for the DSP network has been carefully planned to account for the processor to processor communication capabilities as well as the board to board communication facilities of the Pentek 4290 DSP boards. This configuration allows for optimal communication among the processors in the network. Each channel in the system has one TMS320C6201 processor which performs the required linear interpolation and a second processor which is involved in the summing and channel to channel communications. This arrangement has been evaluated using a two channel system. Assembly language code has been written for a single channel. The linear interpolation

algorithm has been tested and optimized. This code is capable of performing the required linear interpolations for both the 16 bit inphase (I) and 16 bit quadrature (Q) components of the signal at a rate of one I and Q every 5 CPU cycles. Additional code has been written to test the communication algorithms for inter-processor and inter-board communications. All of the testing has been done on an initial beta version of the DSP board which operates at a slower speed than the actual board which will be used.

- Build and test high voltage transmit electronics (single channel), design transmit delay circuit.

NOT COMPLETED - A subcontract to Queen's University to complete this work was awarded 11/10/99. We are still waiting for a decision on the transducer technology (expected Jan. 2000) to proceed with this work.

- Build and test front end electronics (single channel).

COMPLETED - See Appendix 2.

The following tasks were assigned to Tetrad Corporation. A short report describing Tetrad's progress over the last quarter is attached in Appendix 4.

- Array Design - based on results of Phase I complete a full array design.
- Purchase parts and tooling for array fabrication and built initial array prototypes.
- Generate a design for mechanical sector, test drive electronics.
- Perform life testing on cables.
- Initial acoustic testing with array in probe head.
- Specify interface requirements for the array and drive circuitry.

User Interface & Image Processing Software:

- Implement surface rendering of image volumes.

IN PROGRESS - A prerequisite for surface rendering of image volumes is that surfaces be identified within the volume. The surface identification process of image segmentation is underway. We are investigating two approaches. The first semi-automatic approach based on deformable models uses a priori shape information to capture the general shape of the structure to be segmented. This model is then deformed based on the local image features to fit the true underlying shape. The second approach is an extension of a multi-resolution bayesian approach to segment 2D ultrasound images into 3D. We expect our initial results by March 2000.

- Implement volume rendering of image volumes.

IN PROGRESS - Volume rendering of image volumes has been performed using a specialized OpenGL-based toolkit called Volumizer and a program called VolView. Similar to surface

rendering, the quality of volume rendering can be significantly improved when the result of image segmentation is available. Image segmentation, which is underway as stated above, will further aid volume rendering.

- Integrate the appropriate controls into user interface.

COMPLETED - The application GUI has been developed with extensibility as one of its design features. The use of Tk as a GUI builder language allows us to add new controls into the user interface conveniently. The controls for image segmentation, image registration and the proposed toolboxes will be added when these tasks are fully developed.

KEY RESEARCH ACCOMPLISHMENTS

- Theoretical assessment of the proposed synthetic aperture beamformer (see Appendix 1)
- Preliminary design of front end electronics (see Appendix 2)
- Identified the major technical risks for the proposed transducer technology (see Appendix 3)
- Evaluation of motion artifacts associated with the proposed synthetic aperture beamformer (see Appendix 5)
- Interactive multi-planar reformatting
- Demonstration of registration of ultrasound volumes (see Appendix 5)

REPORTABLE OUTCOMES

Manuscripts, abstracts, presentations:

- i) C.R. Hazard and G.R. Lockwood, "Theoretical assessment of a synthetic aperture beamformer for real-time 3-D imaging," *IEEE Trans. Ultrason., Ferroelect., Freq. Contr.*, vol. 46, pp. 972-979, 1999
- ii) C.R. Hazard and G.R. Lockwood, "Effects of motion on a synthetic aperture beamformer for real-time 3D ultrasound," *Proc. 1999 IEEE Ultrason. Symp.*, Lake Tahoe, Nevada, In Press.
- iii) K.A. Swinehart, "Signal conditioning for real-time three-dimensional echocardiography", Masters Thesis, Case Western Reserve University, 1999.
- iv) Vladimir Zagrodsky, Raj Shekhar, and J. Fredrick Cornhill, "Mutual information based registration of cardiac ultrasound volumes," *Proceedings of SPIE Medical Imaging 2000*, San Diego, California, In Press.

Degrees obtained:

Kurtis Andrew Swinehart, Masters of Science, Case Western Reserve University, August 1999.

CONCLUSIONS

We have developed a method for high speed ultrasound imaging. The method permits the acquisition of 40 to 80 images in the time normally required to collect a single image. The increased acquisition speed will be used to collect a 3-D data set in real-time. The objective of this proposal is to build a prototype scanner and develop the software tool required to analyze and interpret the 3-D data.

A major challenge associated with the development of this scanner is how to design an ultrasound beamformer that can process the ultrasound signals at the required frame rates. During the first year of this project we proposed a suitable beamformer architecture and theoretically evaluated the performance of our design using computer simulations. The simulations proved the validity of our approach. They also provided a tool for deriving accurate specifications for each component in the system. Based on this information we have developed a detailed design for the beamformer and have started the process of assembling the electronic hardware.

Next to the ultrasound beamformer, the ultrasound transducer array is the most important and difficult component to design. Based on our specifications for the array, Tetrad Corp. has started investigating suitable transducer technologies and array designs. Preliminary theoretical work and experimental work by Tetrad Corp. have suggested that a new multi-layer transducer design should meet or exceed our specifications. Unfortunately, fabricating a multi-layer device is significantly more difficult, and issues related fabrication and reliability are still being investigated. We expect to make a decision about the transducer technology early this year (2000).

The user interface and image analysis software development is underway alongside the scanner development. Currently, the source of 3D images is a scanner manufactured by Volumetrics, Inc. We have developed software tools to scan convert the native polar data for image analysis purposes. The development of interactive MPR viewing mode together with necessary user interface controls is complete. We have also performed preliminary volume rendering of image data.

Ultrasound image segmentation and registration algorithms are being developed. These algorithms will be core techniques for the specialized toolboxes proposed for the second year of the project.

Real-time 3-D imaging combined with tele-medicine and a set of image analysis tools will enable ultrasound imaging for forward echelon combat casualty care. This technology will be equally effective in civilian emergency care.

REFERENCES

- [1] E. A. Ashton and K. J. Parker, "Multiple resolution bayesian segmentation of ultrasound images," *Ultrasonic Imaging*, Vol. 17, pp. 291-304, 1995.
- [2] C.R.Meyer, J.L.Boes, B.Kim, P.H.Bland, G.L.Lecarpentier, J.B.Fowlkes, M.A.Roubidoux, and P.L.Carson, "Semiautomatic registration of volumetric ultrasound scans", *Ultrasound in Medicine and Biology*, Vol. 25(3), pp.339-347, 1999.

APPENDICES

Appendix 1: Reprint of the publication - C.R. Hazard and G.R. Lockwood, "Theoretical assessment of a synthetic aperture beamformer for real-time 3-D imaging," *IEEE Trans. Ultrason., Ferroelect., Freq. Contr.*, vol. 46, pp. 972-979, 1999.

Appendix 2: Title page and chapters 3 and 4 of Kurtis Andrew Swinehart's Masters Thesis titled, "Signal conditioning for real-time three-dimensional echocardiography".

Appendix 3: Progress report from Tetrad Corporation.

Appendix 4: 1999 Q4 progress report from Tetrad Corporation

Appendix 5: Preprint of the publication - C.R. Hazard and G.R. Lockwood, "Effects of motion on a synthetic aperture beamformer for real-time 3D ultrasound," *Proc. 1999 IEEE Ultrason. Symp.*, Lake Tahoe, Nevada, In Press.

Appendix 6: Preprint of the publication - Vladimir Zagrodsky, Raj Shekhar, and J. Fredrick Cornhill, "Mutual information based registration of cardiac ultrasound volumes," *Proceedings of SPIE Medical Imaging 2000*, San Diego, California, In Press.

Theoretical Assessment of a Synthetic Aperture Beamformer for Real-Time 3-D Imaging

Christopher R. Hazard and Geoffrey R. Lockwood, *Member, IEEE*

Abstract—A real-time 3-D imaging system requires the development of a beamformer that can generate many beams simultaneously. In this paper, we discuss and evaluate a suitable synthetic aperture beamformer. The proposed beamformer is based on a pipelined network of high speed digital signal processors (DSP). By using simple interpolation-based beamforming, only a few calculations per pixel are required for each channel, and an entire 2-D synthetic aperture image can be formed in the time of one transmit event. The performance of this beamformer was explored using a computer simulation of the radiation pattern. The simulations were done for a full 64-element array and a sparse array with the same receive aperture but only five transmit elements. We assessed the effects of changing the sampling rate and amplitude quantization by comparing the relative levels of secondary lobes in the radiation patterns. The results show that the proposed beamformer produces a radiation pattern equivalent to a conventional beamformer using baseband demodulation, provided that the sampling rate is approximately 10 times the center frequency of the transducer (34% bandwidth pulse). The simulations also show that the sparse array is not significantly more sensitive to delay or amplitude quantization than the full array.

I. INTRODUCTION

REAL-TIME 3-D ultrasound imaging has the potential to provide unique clinical information for the diagnosis and treatment of disease. We recently described a method for real-time 3-D imaging using a sparse linear phased array and synthetic aperture beamforming [1], [2]. A real-time 3-D data set is collected by mechanically rocking the transducer array in the elevation direction and rapidly acquiring 2-D images. Computer simulations showed that frame rates as high as one thousand two-dimensional images per second can be achieved using synthetic aperture beamforming without a reduction in the signal-to-noise ratio and with little degradation of image contrast and resolution. However, developing this real-time 3-D system will require a beamformer capable of generating many beams simultaneously. Most modern beamformers use a dedicated beamformer channel for each active receive element. This allows parallel processing of the received signals and real-time beamforming. Because only one beam is generated at a time, the same beamformer hardware can be used for subsequent lines in the image by simply varying the

delay and apodization pattern. This approach is not practical for a real-time 3-D imaging system. If a conventional beamformer were simply duplicated to generate the beams required for real-time 3-D imaging, the resulting system would be massive. A beamformer for a 64-element array generating 80 receive beams simultaneously would require 5120 beamformer channels. Some reduction in hardware can be achieved by separating the expensive focusing delays and the fixed steering delays. This allows the same focusing delays to be shared by adjacent beams provided the angular spacing is not too great. This innovative approach was first introduced by von Ramm *et al.* [3] and Shattuck *et al.* [4] and was used for a real-time 3-D imaging system based on a 2-D transducer array. Unfortunately, this technique is not appropriate for the proposed synthetic aperture system because the beams must be formed simultaneously throughout the entire image.

The need to generate multiple receive beams simultaneously can be avoided by storing the signals from each element in random access memory. Once the signals are stored, an image can be formed by adding points from memory locations selected to provide the samples closest to the desired delayed values. This nearest neighbor approach to beamforming has three advantages. First, the complexity of the beamformer is reduced because only those points that contribute directly to each pixel are used. Second, the pixels can be generated on a rectangular grid and displayed without a separate scan conversion. Finally, and most importantly, storing the digitized data in a random access memory allows serial processing of the pixels. Serial processing avoids the hardware duplication associated with parallel beam formation. However, for real-time 3-D imaging the processing speed must be increased in proportion to the number of beams. Corl and Kino [6] and others [5], [7], [8] developed a nearest neighbor beamformer for a 2-D synthetic aperture imaging system in 1978. Because of hardware limitations, the signals were sampled at close to the Nyquist frequency, and only a single receive signal was recorded for each transmit event. The resulting delay accuracy of the system was too coarse to provide adequate suppression of secondary lobes in the radiation pattern, and the images were not suitable for medical applications.

Modern digital beamformers avoid the problem of excessive sampling by using a combination of coarse and fine delays. Coarse delays are determined by the sampling period, and fine delays are generated within the beamformer. Many different methods have been suggested for generating fine delays based on up-sampling or interpolating the

Manuscript received July 17, 1998; accepted February 19, 1999.

The authors are with The Cleveland Clinic Foundation, Department of Biomedical Engineering, Cleveland, OH 44195 (e-mail: hazard@bme.ri.ccf.org).

data, and a variety of clever hardware designs have been proposed [9]–[13]. Although up-sampling or interpolation reduces the speed required for the analog-to-digital converters (A/D), the number of points that must be generated and processed by the beamformer is still large. A common alternative to up-sampling is to heterodyne the signals to an intermediate frequency or baseband before beamforming [14]–[23]. Simple delay and add processing at data rates much closer to the Nyquist frequency can then be used, provided the phase of each signal is adjusted appropriately. Heterodyning reduces the data rate, but additional costs associated with mixing and filtering the signals may negate this advantage. Newer beamforming techniques based on oversampling delta-sigma A/D offer promise for the future [24]–[26], but current digital beamformers are still large and expensive. Excellent reviews of digital beamforming techniques are given by Thomenius [27] and Mucci [28].

In this paper, we investigate a synthetic aperture beamformer architecture suitable for real-time 3-D imaging. The beamformer is similar to the synthetic aperture beamformer proposed by Corl and Kino with the addition of a fine delay correction and use of receive signals from all elements for each transmit event. We show that these modifications allow high quality beam formation with little increase in the sampling rate and only a moderate increase in the complexity of the beamformer. The performance of the proposed beamformer as a function of the sampling rate and amplitude quantization was evaluated using a computer simulation of the radiation pattern. The results are compared with those for a nearest neighbor beamformer and a modern beamformer using baseband interpolation.

II. SYNTHETIC APERTURE BEAMFORMER DESIGN

The beamformer proposed by Corl and Kino [6] for 2-D synthetic aperture imaging has many features that are attractive for a real-time 3-D imaging system. However, the technology available in 1978 limited the sampling frequency, did not allow multiple receive channels, and prevented real-time interpolation of the synthetic aperture data. For a medical ultrasound beamformer, interpolation is essential to provide the fine delays required for adequate suppression of secondary lobes and to avoid excessive oversampling. Unfortunately, the cost of interpolating the data for a real-time 3-D system is large. For example, 3.2 billion interpolations per second would be required for real-time (~ 0.2 ms) generation of the inphase and quadrature components associated with a 5000 pixel image made using a 64-element array. Obviously, the number of calculations required for each interpolated point must be minimized. Another problem associated with real-time interpolation of a synthetic aperture data set is that the samples are not processed in the order received. Samples may be used for more than one pixel or not used at all. A synthetic aperture beamformer must have the flexibility to adjust the order in which samples are processed. This sorting re-

quirement makes it difficult and inefficient to use a conventional up-sampling or heterodyning approach for fine delay generation.

DSP offer an attractive solution to these problems. DSP provide on-chip memory storage and the memory management needed to sort the data for each pixel. Modern DSP also provide the processing speed necessary for real-time interpolation. Fig. 1 shows a block diagram of the proposed beamformer. The beamformer has two parallel chains with a pair of DSP associated with each array element. The memory inside each DSP is arranged into three separate blocks. One block is used to store the digitized data, and two blocks are organized as stacks that contain the memory addresses corresponding to the coarse delays and the coefficients for interpolation and apodization. The coarse delays and interpolation and apodization coefficients are calculated ahead of time and loaded into memory when the system is turned on. Because data can be randomly accessed from memory, each DSP can work on a different pixel, and the order of calculations can be arranged for pipelined addition.

Fig. 2 illustrates the flow of data and the timing of calculations for the proposed beamformer. The calculation of each pixel begins with the first DSP at the top of the pipeline and continues through the chain until signals from each array element have been added. For each calculation cycle, each DSP must calculate an interpolated value (${}^p y_c$, the interpolated value for pixel p at channel c) and add it to an accumulating sum (${}^p S_c$, the sum for pixel p at channel c). The interpolated value is calculated by first fetching two data points from memory that are closest to the desired delay value. A fine delay correction is introduced by linearly interpolating between the two points. Once this calculation is complete, the interpolated value is added to the accumulating sum that was passed down from the upstream channels. The updated sum, ${}^p S_c$, is then passed to the next DSP. If v_1 and v_2 represent the sample values surrounding the desired delayed value, the new value of the accumulating sum, ${}^p S_c$, is given by:

$${}^p S_c = {}^p y_c + {}^p S_{c-1} = \gamma((v_2 - v_1)\Delta t + v_1) + {}^p S_{c-1} \quad (1)$$

where γ is the apodization coefficient, Δt is the fraction of the sample period corresponding to the desired fine delay, and ${}^p S_{c-1}$ is the accumulating sum passed down from the upstream DSP. Many DSP are optimized to calculate a multiply and add operation in a single cycle. Consequently, it is useful to rearrange (1) into two multiply and add operations:

$$S_{\text{temp}} = \alpha v_1 + {}^p S_{c-1} \text{ and} \quad (2)$$

$${}^p S_c = \beta v_2 + S_{\text{temp}} \quad (3)$$

where $\alpha = \gamma(1 - \Delta t)$ and $\beta = \gamma(\Delta t)$. Assuming the coefficients α and β are calculated ahead of time and stored in memory, only two multiply and add operations per channel are required to interpolate and apodize the inphase or quadrature component of a pixel. In comparison, a simple

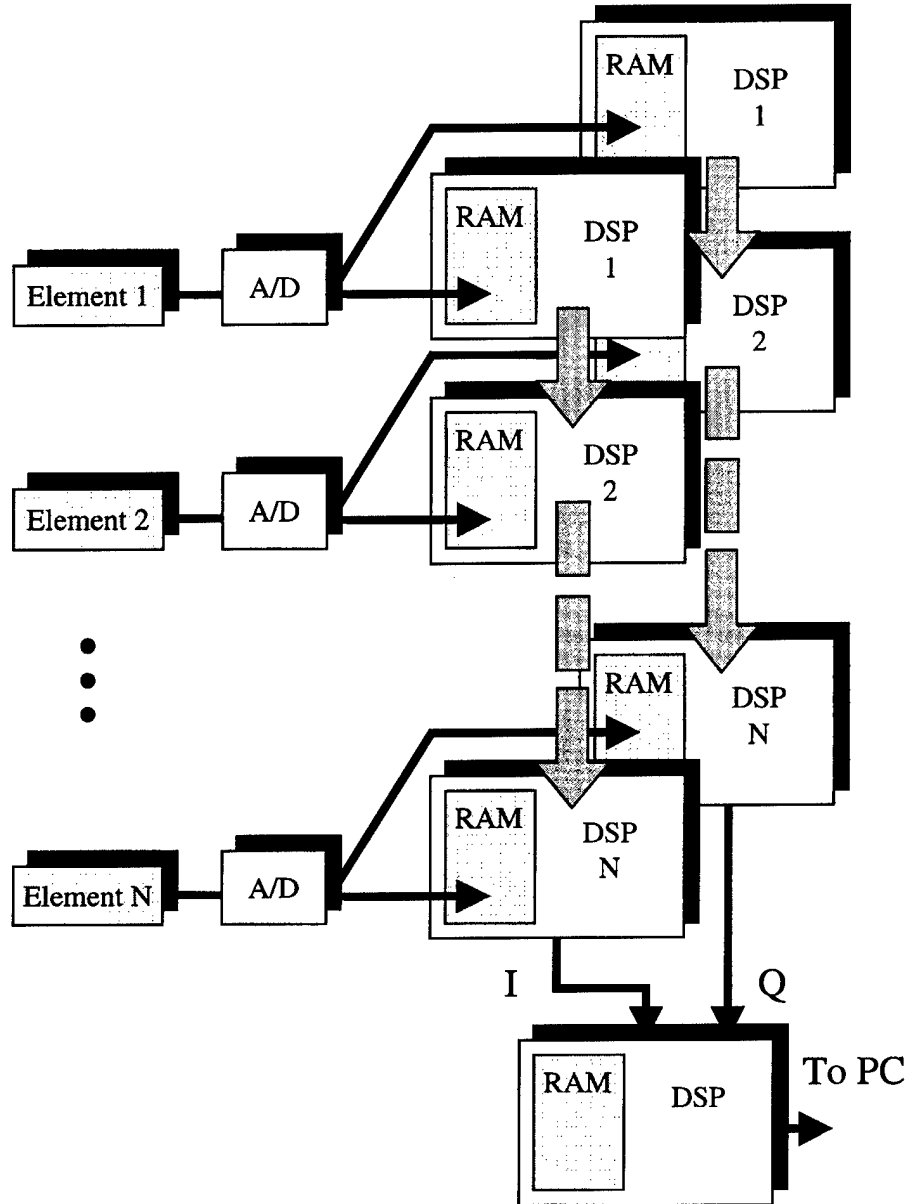


Fig. 1. Proposed synthetic aperture beamformer architecture. The signals received by each element are digitized and stored in memory. A network of DSP is used to delay signals using linear interpolation. The network of DSP is arranged in a pipeline architecture to facilitate summing of the delayed signals.

20-tap FIR interpolation filter would require 10 times as many calculations. Another advantage of this approach is that different values of α and β can be stored in each DSP for every pixel in the image. This provides dynamic control over the aperture shape and delay pattern for every transmit-receive event and optimal focusing at every pixel.

The final task of the beamformer is to detect the envelope of the signal. Second-order sampling provides an efficient estimate of the envelope at a given pixel [17], [29]. Parallel processing streams are used to calculate two interpolated values at each array element. One value, called the inphase component (I), is calculated for the desired delay, and a second beamformed value, called the quadrature component (Q), is calculated with an additional delay of

one-quarter of a period. Assuming that the envelope varies slowly, the envelope can be approximated as the square root of the sum of the squares:

$$\text{Envelope} = \sqrt{I^2 + Q^2}. \quad (4)$$

A final DSP at the end of the pipeline is used to add the I and Q values from multiple transmit events and to calculate the envelope value for each pixel. Because second-order sampling requires that two interpolated values be calculated for each pixel for each receive channel, the total cost per channel for calculating a pixel is four multiply and add operations, which is small enough to permit real-time 3-D beamforming using existing DSP technology. For example, the fixed point TMS320C6x manufactured by

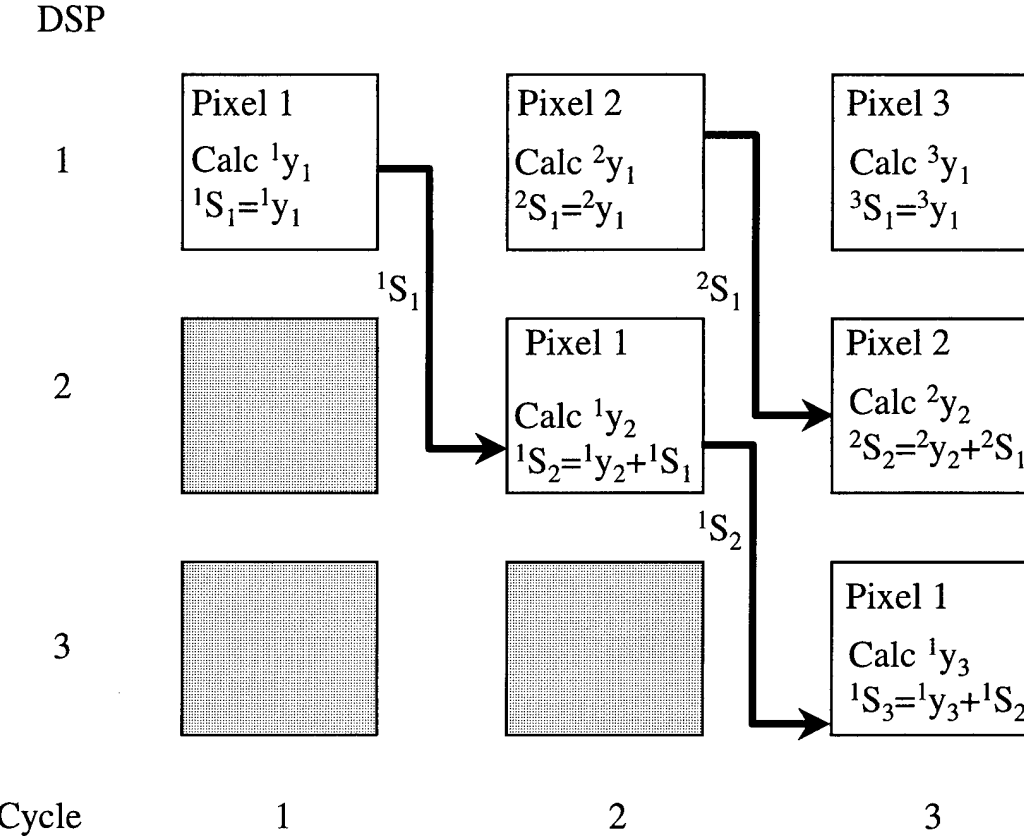


Fig. 2. Diagram showing the flow of data and the timing for the calculation of a pixel using the proposed linear interpolation beamformer. ${}^p y_{c,t}$ is the interpolated contribution to pixel p for channel c , and ${}^p S_{c,t}$ is the accumulating sum for pixel p at channel c .

Texas Instruments (Dallas, TX) can process 400 million multiply and add operations every second.

Linear interpolation provides an efficient method for generating a fine delay, provided the sampling frequency is adequate. The success of this approach will ultimately depend on how fast the data must be sampled for suppression of secondary lobes (less than -60 dB). Many researchers have investigated the impact of amplitude and delay quantization on secondary lobes [8], [14], [15], [22], [27], [28], [30]–[36]. A variety of system parameters, including the bandwidth of the pulse; the number, spacing, and apodization of the transmit and receive elements; and the beamforming algorithm, have all been shown to affect the amplitude of secondary lobes. Generally, there is an inverse relationship between the complexity of the beamformer and the required sampling frequency. Unfortunately, accurately predicting the amplitude of secondary lobes for a given system is difficult. In the next section, we use a computer simulation to investigate the performance of the proposed beamformer as a function of sampling frequency and amplitude quantization.

III. COMPUTER SIMULATIONS

The effects of amplitude quantization and discrete time sampling on the radiation pattern of an array were examined for three synthetic aperture beamformers: the nearest neighbor approach introduced by Corl and Kino [5]–[8], the

proposed linear interpolation beamformer, and a baseband demodulation beamformer using the method outlined by O'Donnell *et al.* [14]. The nearest neighbor approach is the simplest and least expensive computationally, but a prohibitively high sampling rate is needed for adequate delay accuracy. At the other extreme, baseband demodulation requires a modest sampling rate (4 to 10 times the bandwidth of the pulse), but the required mixing, filtering, and phase rotation operations associated with shifting the signal to baseband are computationally expensive. The proposed linear interpolation beamformer offers a compromise between the nearest neighbor and heterodyning approaches in the sampling rate and the number of computations per pixel.

For each of the three different beamforming approaches, two different transducer arrays were simulated: a full array using 64 transmit and receive elements (0.95 $\lambda/2$ element spacing) and a sparse array with the same receive aperture (64 elements) but only 5 active transmit elements [transmit spacing 11(0.95) $\lambda/2$]. The center frequency of the transducer array was 3.5 MHz, and a raised cosine apodization was used for both arrays. The speed of a synthetic aperture imaging system is determined ultimately by the number of transmit elements. By using only a few transmit events per image, the frame rates necessary for real-time 3-D imaging can be obtained. The signal loss associated with fewer transmit pulses can be reduced by

increasing the power delivered to each transmit element and by using multiple transmit elements for each transmit pulse [1], [37]. Although a full array with 64 transmit elements would be too slow to acquire a 3-D synthetic aperture data set in real-time, the radiation pattern of the full array provides a useful benchmark for comparing the performance of the sparse array.

The broadband, two-way radiation pattern for each array was evaluated numerically by simulating a sector scan of a point target. Attenuation was ignored in this simulation, and a uniform element directivity was assumed. The point target was placed in front of the array at a distance equal to four times the receive aperture width. Signals received from the point target were calculated for every transmitter-receiver pair and then discretely sampled in time and quantized in amplitude to represent analog-to-digital conversion at the front end of the beamformer. Radial scan lines were formed from -45° to 45° in steps of 1° . The amplitude of the signal at each point in the sector scan was calculated by summing an appropriately delayed and weighted pulse over each transmit and receive element and then approximating the envelope using second-order sampling. The pulse was a Gaussian-modulated sinusoid with a center frequency of 3.5 MHz and a -6 dB bandwidth of 34%. Beamforming delays were introduced using one of the three beamforming approaches. We repeated the simulations using different sampling frequencies (from 20 to 100 MHz) and varying levels of amplitude quantization (from 8 to 14 bits). The radiation patterns were displayed by plotting the maximum value of the demodulated signal along each scan line as a function of the scan angle. This ensures that the worst case secondary lobes are displayed.

The effects of amplitude and delay quantization were considered separately. In section A, the radiation patterns were calculated with varying levels of amplitude quantization, but no delay quantization. In section B, delay quantization is introduced with no amplitude quantization.

A. Amplitude Quantization

Fig. 3 shows the radiation patterns for the sparse array with different levels of amplitude quantization. Perfect beamforming (no amplitude quantization or sampling) is also included as a baseline for comparison. The main lobe of the pattern is identical to the perfect beamforming case for all levels of quantization down to -60 dB. For 8-bit quantization, the secondary lobes are around -70 dB; for 10 bits, they are approximately -80 dB; at 12 bits, they are suppressed to -90 dB. At 14 bits, the radiation pattern is similar to the perfect beamforming case; therefore, the secondary lobes are limited by the number of array elements and not the amplitude quantization.

Fig. 4 shows the effect of the different levels of amplitude quantization on the full array. The main lobe is again identical to the perfect beamforming case down to -60 dB. By increasing the number of transmit elements from 5 to 64, the level of quantization-limited secondary lobes is improved by approximately 5 to 10 dB. For the full array, the

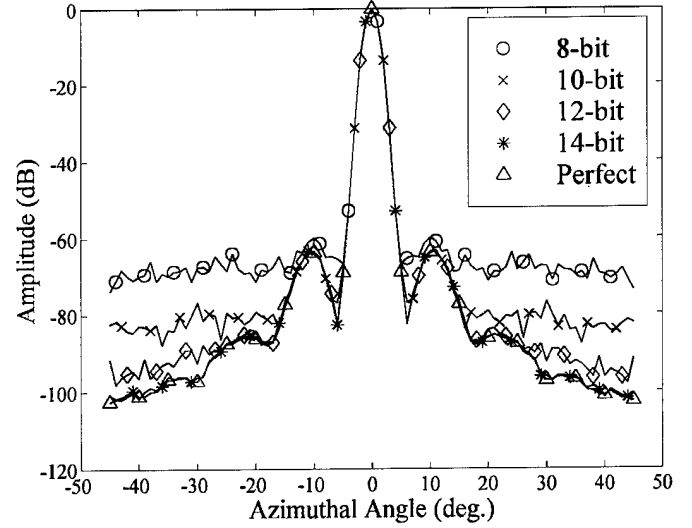


Fig. 3. Normalized radiation patterns for the sparse array (5 transmit elements, 64 receive elements) using 8-, 10-, 12-, and 14-bit quantization. The unquantized radiation pattern is also shown for comparison.

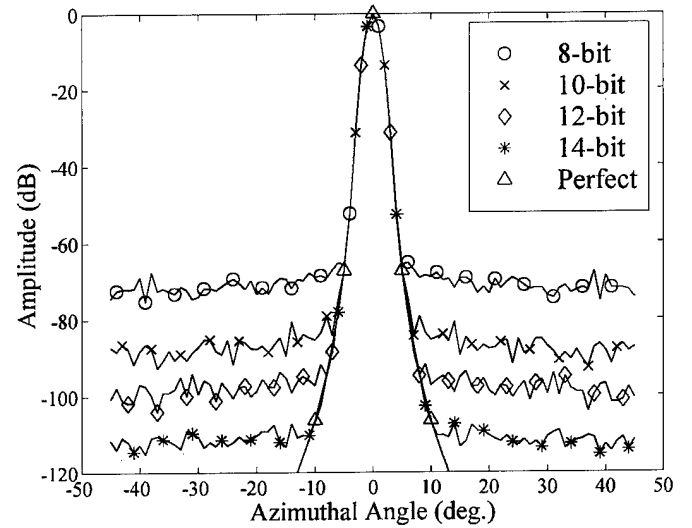


Fig. 4. Normalized radiation patterns for the full array (64 transmit and receive elements) using 8-, 10-, 12-, and 14-bit quantization. The unquantized radiation pattern is also shown for comparison.

radiation pattern with 14-bit quantization is similar to the perfect beamforming pattern down to -110 dB.

B. Sampling Rate

The effects of sampling rate on secondary lobes were explored for the three beamforming strategies: nearest neighbor, linear interpolation, and baseband demodulation. Each interpolation method was evaluated at sampling rates from 20 to 100 MHz. Fig. 5 shows the resulting secondary lobe levels for the sparse array using nearest neighbor, linear interpolation, and baseband demodulation beamforming. Sampling rates of 20, 60, and 100 MHz are shown in Figs. 5(a)–(c), respectively. Figs. 6(a)–(c) show

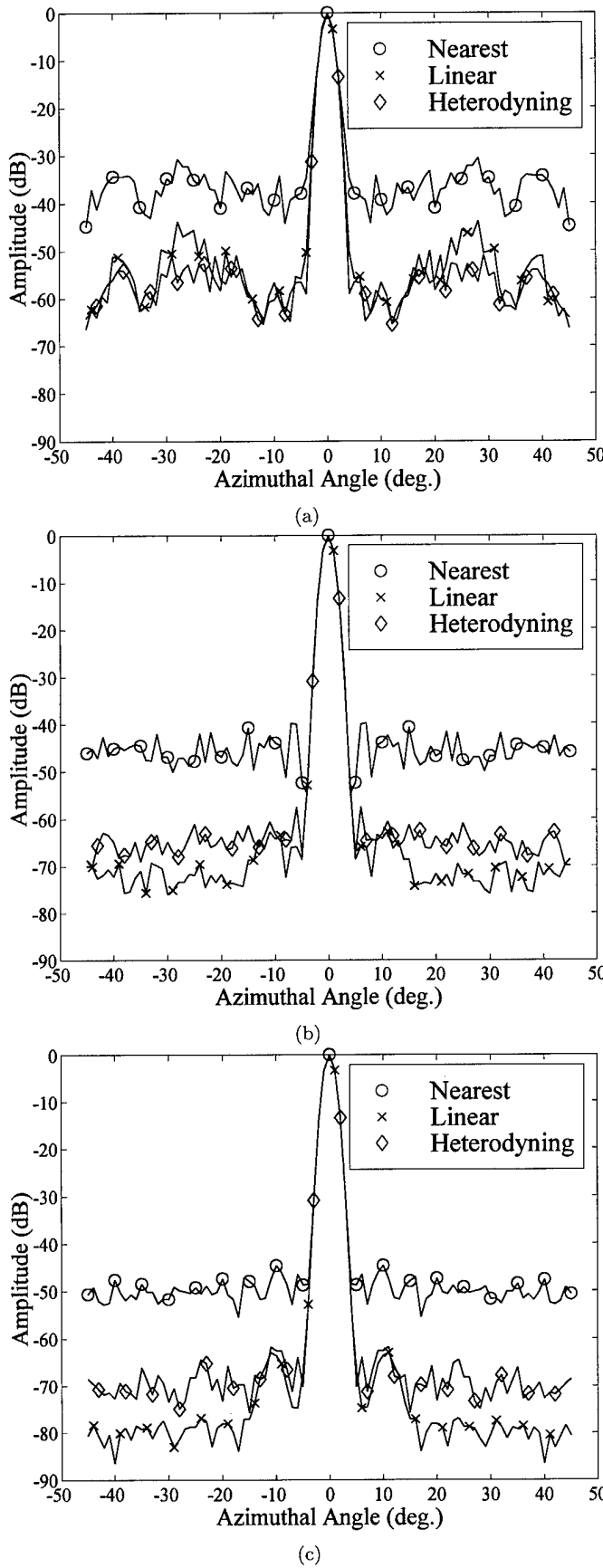


Fig. 5. Sparse array radiation patterns for nearest neighbor, linear interpolation, and heterodyning (baseband demodulation) beamformers with sampling rates of (a) 20, (b) 60, and (c) 100 MHz.

the corresponding results for the full array with 64 transmit elements.

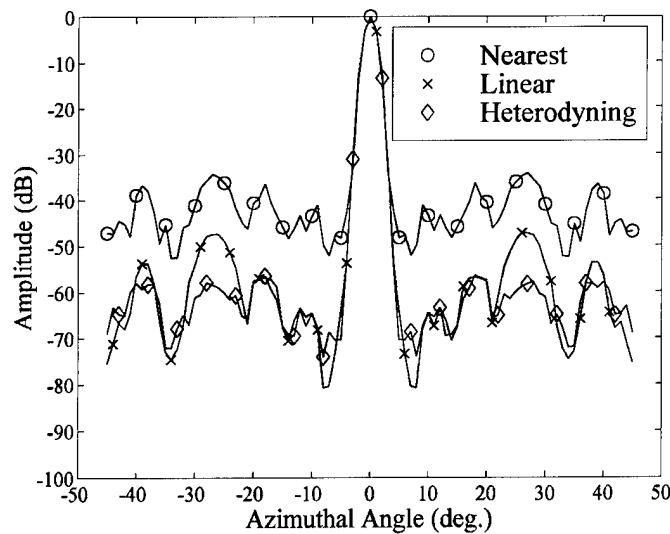
Using nearest neighbor beamforming, the secondary lobes for the sparse array (Fig. 5) range from about -35 dB at a 20 MHz sampling rate to approximately -50 dB at 100 MHz. The results for the full array (Fig. 6) are only slightly better with secondary lobe levels from -35 to -60 dB over the same range of sampling frequencies. A prohibitive sampling rate of about 400 MHz is required to achieve secondary lobe levels below -60 dB using nearest neighbor beamforming. At a sampling rate of 20 MHz [Fig. 5(a), 6(a)], baseband demodulation and linear interpolation beamforming produce similar radiation patterns for both the full and sparse arrays. At higher sampling rates, linear interpolation beamforming produces lower secondary lobes than baseband demodulation beamforming. There is a much greater improvement in the radiation pattern as a function of sampling rate for the linear interpolation beamformer than for the baseband demodulation beamformer. At sampling rates greater than 20 MHz, the secondary lobes are below -60 dB for linear interpolation and baseband beamforming. The sparse array was not significantly more sensitive to changes in the sampling rate than the full array. This was true for both linear interpolation and baseband demodulation.

Fig. 7 shows the radiation pattern for the sparse array using linear interpolation beamforming with a sampling rate of 40 MHz and 10-bit amplitude quantization. Combining the effects of amplitude quantization and sampling further degrades the radiation pattern, but secondary lobes are still below -60 dB at all angles.

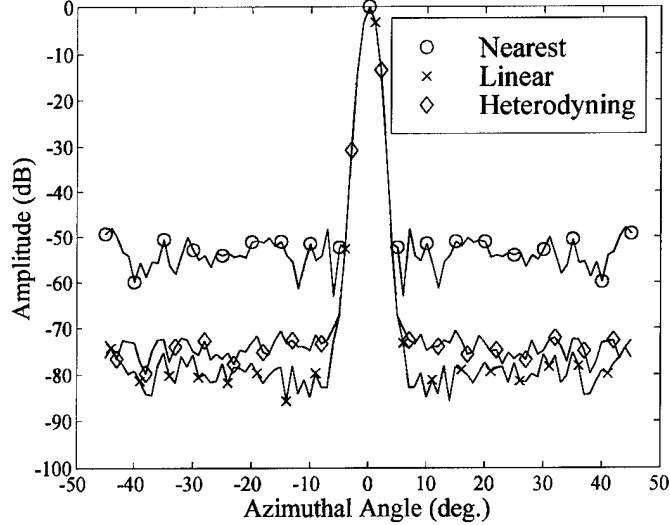
IV. SUMMARY AND CONCLUSIONS

In this paper, we described a beamformer suitable for real-time 3-D synthetic aperture imaging. The beamformer is realized using a network of digital signal processors. Modern DSP provide the speed and the memory management required for sorting and interpolating the data in real time. By controlling the order in which pixels are generated, the DSP network can be arranged in a pipeline structure to allow efficient summing of the contributions from each receive channel. A unique set of interpolation coefficients is used to calculate the interpolated samples required for each pixel in the image. By precalculating the coefficients and using second-order sampling for envelope detection, only four multiply and add operations per channel are required for each pixel, independent of the sampling rate. This strategy provides an accurate and very efficient estimate of the interpolated samples without the proliferation of samples associated with up-sampling or the complexity of a heterodyning approach.

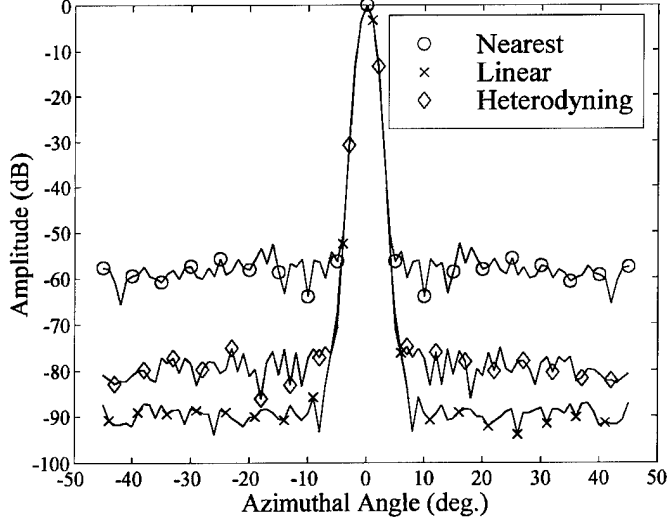
The success of the proposed linear interpolation beamformer will depend on the sampling frequency and amplitude quantization levels needed to suppress secondary lobes adequately. A real-time 3-D synthetic aperture system requires the use of a sparse array. Because fewer



(a)



(b)



(c)

Fig. 6. Full array (64 transmit and receive elements) radiation patterns for nearest neighbor, linear interpolation, and heterodyning (baseband demodulation) beamformers with sampling rates of (a) 20, (b) 60, and (c) 100 MHz.

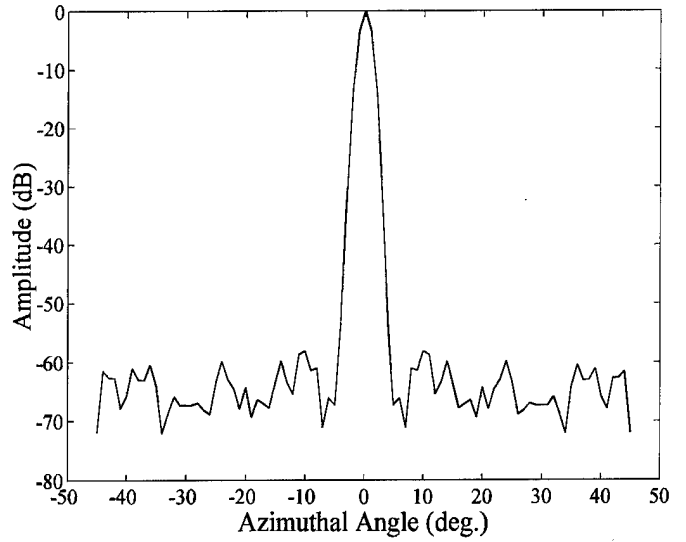


Fig. 7. The normalized radiation pattern for the sparse array (5 transmit elements, 64 receive elements) digitizing at 40 MHz with 10 bits of accuracy and using linear interpolation beamforming.

transmit-receive events are used in beamforming, it is particularly important to evaluate the sensitivity of the system to amplitude and delay quantization. The effects of sampling and amplitude quantization were examined using computer simulations of the beamformer. The simulations assumed a Gaussian-shaped pulse, centered at 3.5 MHz with a -6 dB bandwidth of 34%. Similar results were obtained for a pulse with a -6 dB bandwidth of 68%. The results show that a 10-bit A/D would provide sufficient dynamic range to keep secondary lobes below -70 dB for the sparse array (5 transmit elements, 64 receive elements). At finer levels of amplitude quantization, secondary lobes are limited by the number of array elements and not by the amplitude quantization. The secondary lobes in the radiation pattern of the linear interpolation beamformer were found to be suppressed approximately 20 dB compared with the nearest neighbor beamformer. At a sampling rate of 20 MHz, baseband demodulation and linear interpolation have similar performance. At higher sampling rates, linear interpolation outperforms baseband demodulation. The sparse array was not found to be significantly more sensitive to amplitude and delay quantization than the full array (64 transmit and receive elements). The difference between the amplitude of the secondary lobes for the full and sparse arrays was usually less than 10 dB.

The simulations demonstrate that a simple linear interpolation beamformer can produce a high quality radiation pattern with secondary lobes below -60 dB for a sparse array. Such a system is feasible with present technology and could theoretically achieve frame rates as high as one thousand 2-D images per second.

REFERENCES

[1] G. R. Lockwood, J. R. Talman, and S. S. Brunke, "Real-time 3-D ultrasound imaging using sparse synthetic aperture beam-

forming," *IEEE Trans. Ultrason., Ferroelect., Freq. Contr.*, vol. 45, no. 4, pp. 980-988, Jul. 1998.

[2] G. R. Lockwood and F. S. Foster, "Design of sparse array imaging systems," *Proc. 1995 IEEE Ultrason. Symp.*, Seattle, WA, pp. 1237-1243.

[3] O. T. von Ramm, S. W. Smith, and H. G. Pavay, Jr., "High-speed ultrasound volumetric imaging system—Part II: Parallel processing and image display," *IEEE Trans. Ultrason., Ferroelect., Freq. Contr.*, vol. 38, no. 2, pp. 109-115, Mar. 1991.

[4] D. P. Shattuck, M. D. Weinshenker, S. W. Smith, and O. T. von Ramm, "Explososcan: A parallel processing technique for high speed ultrasound imaging with linear phased arrays," *J. Acoust. Soc. Amer.*, vol. 75, no. 4, pp. 1273-1282, 1984.

[5] P. D. Corl, G. S. Kino, C. S. DeSilets, and P. M. Grant, "A digital synthetic focus acoustic imaging system," in *Acoustic Imaging*, vol. 8, A. F. Metherell, Ed. New York: Plenum, 1980, pp. 39-53.

[6] P. D. Corl and G. S. Kino, "A real-time synthetic aperture imaging system," in *Acoustic Imaging*, vol. 9, K. Y. Wang, Ed. New York: Plenum, 1980, pp. 341-355.

[7] S. Bennett, D. K. Peterson, P. D. Corl, and G. S. Kino, "A real-time synthetic aperture digital acoustic imaging system," in *Acoustic Imaging*, vol. 10, P. Alais and A. F. Metherell, Eds. New York: Plenum, 1982, pp. 669-692.

[8] D. K. Peterson and G. S. Kino, "Real-time digital image reconstruction: a description of imaging hardware and an analysis of quantization errors," *IEEE Trans. Sonics Ultrason.*, vol. SU-31, no. 4, pp. 337-351, Jul. 1984.

[9] M. Karaman, A. Atalar, and H. Koymen, "VLSI circuits for adaptive digital beamforming ultrasound imaging," *IEEE Trans. Med. Imag.*, vol. 12, no. 4, pp. 711-720, Dec. 1993.

[10] X. Bernard, "Ultrasonic echography apparatus utilizing a digital device for forming channels in the receiving mode," U.S. Patent 5088496, Feb. 18, 1992.

[11] U. Saugeon, "Method and apparatus for digital delay of ultrasound signals upon reception therof," U.S. Patent 4787392, Nov. 29, 1988.

[12] D. Lipschutz, "Delay interpolator for digital phased array ultrasound beamformers," U.S. Patent 5345426, Sep. 6, 1994.

[13] Y. C. Lim and S. R. Parker, "FIR filter design over a discrete powers-of-two coefficient space," *IEEE Trans. Acoust., Speech, Signal Processing*, vol. ASSP-31, no. 3, pp. 583-591, Jun. 1983.

[14] M. O'Donnell, W. E. Engeler, J. T. Pedicone, A. M. Itani, S. E. Noujaim, R. J. Dunki-Jacobs, W. M. Leve, C. L. Chalek, L. S. Smith, J. E. Piel, R. L. Harris, K. B. Wells, and W. L. Hinrichs, "Real-time phased array imaging using digital beam forming and autonomous channel control," *Proc. 1990 IEEE Ultrason. Symp.*, Honolulu, HI, pp. 1499-1502.

[15] B. D. Steinberg, "Digital beamforming in ultrasound," *IEEE Trans. Ultrason., Ferroelect., Freq. Contr.*, vol. 39, no. 6, pp. 716-721, Nov. 1992.

[16] S. H. Chang, S. B. Park, and G. H. Cho, "Phase-error-free quadrature sampling technique in the ultrasonic B-scan imaging system and its application to the synthetic focusing system," *IEEE Trans. Ultrason., Ferroelect., Freq. Contr.*, vol. 40, no. 3, pp. 216-223, May 1993.

[17] T. K. Song and S. B. Park, "A new digital phased array system for dynamic focusing and steering with reduced sampling rate," *Ultrason. Imaging*, vol. 12, pp. 1-16, 1990.

[18] J. H. Kim, T. K. Song, and S. B. Park, "Pipelined sampled-delay focusing in ultrasound imaging systems," *Ultrason. Imaging*, vol. 9, pp. 75-91, 1987.

[19] J. E. Powers, D. J. Phillips, M. A. Bramdestini, and R. A. Sigelmann, "Ultrasound phased array delay lines based on quadrature sampling techniques," *IEEE Trans. Sonics Ultrason.*, vol. SU-27, no. 6, pp. 287-295, Nov. 1980.

[20] R. Lutolf, A. Vieli, and S. Basler, "Ultrasonic phased-array scanner with digital echo synthesis for doppler echocardiography," *IEEE Trans. Ultrason., Ferroelect., Freq. Contr.*, vol. 35, no. 5, pp. 494-506, Sep. 1989.

[21] G. Manes, P. Tortoli, and F. Andreuccetti, "Synchronous dynamic focusing for ultrasound imaging," *IEEE Trans. Ultrason., Ferroelect., Freq. Contr.*, vol. 35, pp. 14-20, Jan. 1988.

[22] G. Manes, C. Atzeni, and C. Susini, "Design of a simplified delay system for ultrasound phased array imaging," *IEEE Trans. Sonics Ultrason.*, vol. SU-30, no. 6, pp. 350-354, Nov. 1983.

[23] R. G. Pridham and R. A. Mucci, "Digital interpolation beamforming for low-pass and bandpass signals," *Proc. IEEE*, vol. 67, pp. 904-919, Jun. 1979.

[24] S. E. Noujaim, S. E. Garverick, and M. O'Donnell, "Phased array ultrasonic beam forming using oversampled A/D converters," U.S. Patent 5203335, Apr. 20, 1993.

[25] M. Dean, "Digital beamforming array," U.S. Patent 5461389, Oct. 24, 1995.

[26] S. R. Freeman, M. K. Quick, M. A. Morin, R. C. Anderson, C. S. DeSilets, T. E. Linnenbrink, and M. O'Donnell, "An ultrasound beamformer using oversampling," *Proc. 1997 IEEE Ultrason. Symp.*, Ontario, Canada, pp. 1687-1690.

[27] K. E. Thomenius, "Evolution of ultrasound beamformers," *Proc. 1996 IEEE Ultrason. Symp.*, San Antonio, TX, pp. 1615-1622.

[28] R. A. Mucci, "A comparison of efficient beamforming algorithms," *IEEE Trans. Acoust., Speech, Signal Processing*, vol. ASSP-32, no. 3, pp. 548-558, Jun. 1984.

[29] F. S. Foster, J. D. Larson, R. J. Pittaro, P. D. Corl, A. P. Greenstein, and P. K. Lum, "A digital annular array prototype scanner for realtime ultrasound imaging," *Ultrason. Med. Biol.*, vol. 15, no. 7, pp. 661-672, 1989.

[30] W. L. Beaver, "Phase error effects in phased array beam steering," *Proc. 1977 IEEE Ultrason. Symp.*, Phoenix, AZ, pp. 264-267.

[31] D. K. Peterson, S. D. Bennett, and G. S. Kino, "Reducing sidelobe levels of a synthetic aperture digital acoustic imaging system," *Proc. 1982 IEEE Ultrason. Symp.*, San Diego, CA, pp. 815-820.

[32] C. R. Cooley and B. S. Robinson, "Synthetic focus imaging using partial datasets," *Proc. 1994 IEEE Ultrason. Symp.*, Cannes, France, pp. 1539-1542.

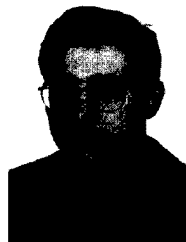
[33] M. Nikoonahad, "Synthetic focused image reconstruction in the presence of a finite delay noise," *Proc. 1986 IEEE Ultrason. Symp.*, Williamsburg, VA, pp. 819-824.

[34] P. A. Magnin, O. T. von Ramm, and F. L. Thurstone, "Delay quantization error in phased array images," *IEEE Trans. Sonics Ultrason.*, vol. SU-28, no. 5, pp. 305-310, Sep. 1981.

[35] K. N. Bates, "Tolerance analysis for phased arrays," in *Acoustic Imaging*, vol. 9, K. Y. Wang, Ed. New York: Plenum, 1980, pp. 239-262.

[36] K. Watanabe, T. Noda, A. Shiba, A. Iida, K. Murakami, and T. Shimura, "The effect of delay error on the sidelobe level in synthetic aperture imaging," *Proc. 1996 IEEE Ultrason. Symp.*, San Antonio, TX, pp. 1559-1562.

[37] M. Karaman, P. Li, and M. O'Donnell, "Synthetic aperture imaging for small scale systems," *IEEE Trans. Ultrason., Ferroelect., Freq. Contr.*, vol. 42, no. 3, pp. 429-442, May 1995.



Christopher R. Hazard was born in Cincinnati, OH on June 7, 1973. He received the B.S. degree in applied physics from Xavier University in 1995 and the M.S. degree in biomedical engineering from The Ohio State University in 1997. He is currently working toward the Ph.D. degree in biomedical engineering from The Ohio State University at the Cleveland Clinic Foundation in Cleveland, OH.

Mr. Hazard's research interests include high frequency imaging, intravascular ultrasound, and real-time 3-D ultrasound imaging.



Geoffrey R. Lockwood (M'95) was born in Toronto, ON, Canada in 1961. He received the B.A.Sc. degree in electrical engineering from the University of Toronto in 1985 and the M.Sc. and Ph.D. degrees in medical bio-physics from the University of Toronto in 1988 and 1992, respectively.

Dr. Lockwood presently holds a joint appointment as a staff scientist at the Cleveland Clinic and as an assistant professor of mechanical engineering at The Ohio State University. His research interests include high frequency ultrasound imaging and real-time 3-D ultrasound imaging.

**SIGNAL CONDITIONING FOR REAL-TIME
THREE-DIMENSIONAL ECHOCARDIOGRAPHY**

by

KURTIS ANDREW SWINEHART

Submitted in partial fulfillment of the requirements
for the degree of Master of Science

Thesis Adviser: Dr. Steven L. Garverick

Department of Electrical Engineering

CASE WESTERN RESERVE UNIVERSITY

August, 1999

3. DESIGN AND SIMULATION

3.1 Circuit Architecture

The first step in designing the front end circuitry for the system is determining the most difficult and most important specifications to achieve and select parts and topologies which will make these specifications easier to meet. The most important specification was the time-gain control with 45-dB range. The second most important consideration was the noise requirement. With these two considerations in mind, the Analog Devices part AD604 was selected for its programmable gain from 0 dB to 48 dB and its “ultralow” input referred noise ($0.8 \text{ nV}/\sqrt{\text{Hz}}$) [8].

The third most important design consideration was the high voltage protection circuitry. A topology was found in a paper by Lockwood and Hazard [9] describing a method of protecting the pre-amplifier from high-voltage pulses. The final consideration was ensuring that the analog-to-digital converter’s full scale range was utilized. A simple operational amplifier circuit was determined to have an adequate gain-bandwidth for this application.

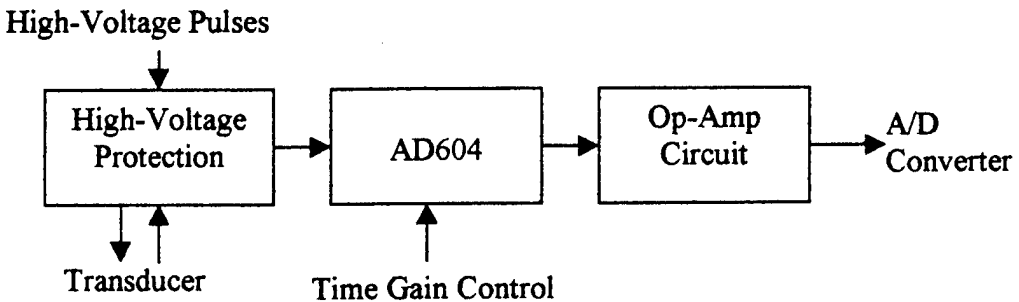


Figure 15. Circuit Architecture

3.2 Transducer Simulation Model

In order to optimally design the high-voltage protection circuitry, the behavior of the ultrasonic transducer had to be considered. The model used in this work, provided by Dr. Lockwood, is based on the KLM model for ultrasonic transducers [10,11]. The model uses the ABCD network parameters of basic elements to build the transducer. These ABCD network parameters are a matrix representation of a two port element. These two-by-two matrices relate the voltage and current at the input to the voltage and current at the output by the equation

$$\begin{bmatrix} V_{IN} \\ I_{IN} \end{bmatrix} = \begin{bmatrix} A & B \\ C & D \end{bmatrix} \cdot \begin{bmatrix} V_{OUT} \\ -I_{OUT} \end{bmatrix}.$$

An entire system can be represented by multiplying these network parameter matrices together. As shown in Figure 16, the transducer model is represented by a series bulk electrical impedance followed by a transformer from electrical to acoustic terms followed by an acoustic transmission line in parallel terminated by an impedance representing the sound transmitted though the back of the transducer followed by two series transmission lines representing the matching layers of the transducer. The Matlab code used for simulation can be found in Appendix A.

The input and output impedances, as well as the maximum output voltage of the transducer, are critical parameters. The input and output impedances of the transducer can be determined from the product of all of the ABCD networks by dividing A by C of the transmit simulation for the input impedance of the transducer, and dividing D by B to determine the output impedance [11]. The input and output

impedance are the same if the transducer medium acts like an infinitely long transmission line.

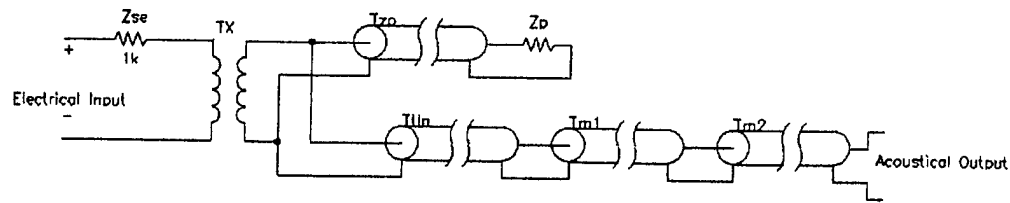


Figure 16. Transducer KLM Model

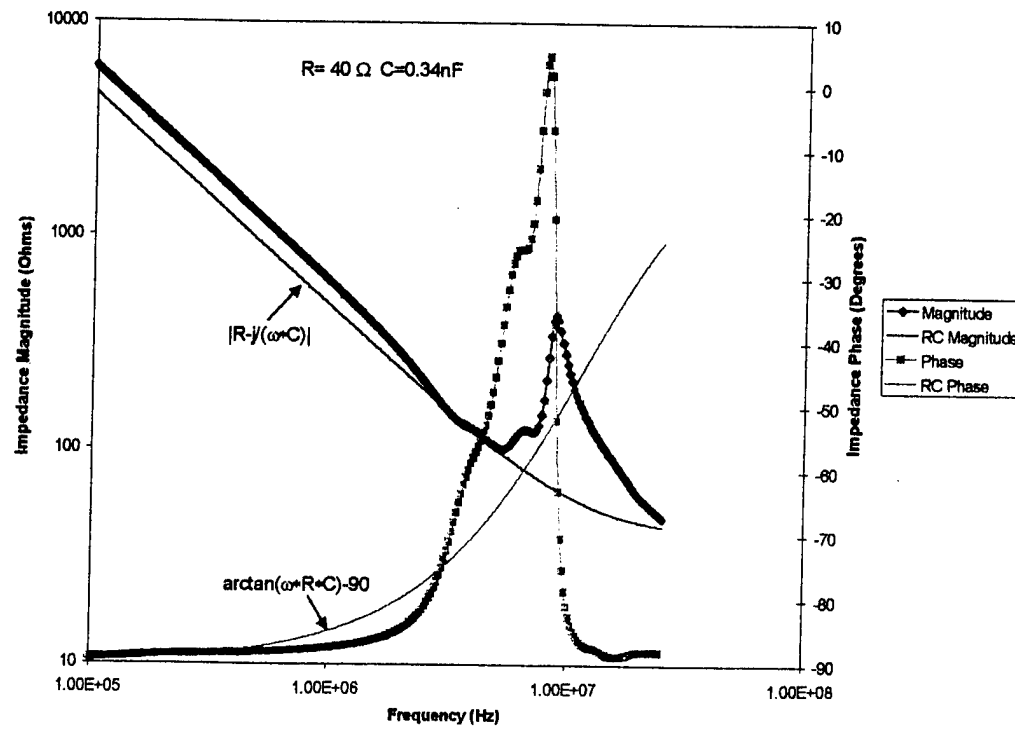


Figure 17. Transducer Input and Output Impedance vs. Frequency

After the input and output impedance was determined in Matlab, a SPICE model was constructed. In SPICE the transducer was modeled as a transconductance with magnitude and phase from a lookup table. The values in the table came from the results of the Matlab simulation. The input and output impedance versus frequency is plotted in Figure 17. For frequencies less than 3 MHz, the transducer behaves mostly like a capacitor and can be modeled accurately as a 0.34-nF capacitor in series with a 40- Ω resistance.

3.3 High-Voltage Protection Circuit

The topology for the high-voltage protection circuit described by Lockwood and Hazard [9] uses four diodes and a capacitor to isolate the high-voltage pulse from the amplifiers as shown in Figure 18. Pairs of diodes are connected in parallel with opposite polarities to form two bi-directional voltage clamps. A capacitor couples the output from the transducer to the amplifier input. One diode clamp (D3/D4) limits the voltage applied to the pre-amplifier during the high-voltage pulsing, while the other (D1/D2) isolates the pulse generator from the relatively weak signals returning from the transducer.

The circuit operates on the principle that a high-voltage pulse turns on all of the diode clamps, so there is a conducting path from the pulse generator to the transducer and a path from the amplifier input to ground. This ensures that the voltage at the input of the amplifier is limited to the on-voltage of the diodes. When the high-voltage pulse is released, the diode clamps turn off and the pulse generator

input does not have a conducting path to the circuit and the transducer is capacitively coupled to the input of the amplifier.

The selection of the capacitor value is a trade-off between the power coupled to the transducer during a high-voltage pulse and the attenuation of the received signal from the transducer. As the capacitor size increases, the power received by the transducer decreases but the attenuation of the signal from the transducer decreases.

Another consideration when selecting the capacitor size is the peak current through the diodes. An order of magnitude calculation was performed to determine a relative size of capacitor required for the circuit to work well. For $50\text{-}\Omega$ coaxial cables much shorter than the wavelength of the signals on the cable, the cables can be modeled by a capacitor equal to 30 pF/ft [14]. By modeling the transducer with the SPICE model derived from the Matlab simulation, modeling the coaxial cables as capacitors of value 300 pF , and using the input impedance of the AD604 ($300 \text{ K}\Omega$ in parallel with 8 pF), the coupling capacitor needed to be greater than 500 pF . Using 500 pF and the default SPICE diode model, it was determined that the diodes need to carry over 50 Amps of peak current during a high-voltage pulse. From this consideration, the Vishay Lite-on S3A diodes were selected. These were the smallest 100-A maximum surge current diodes available.

After these diodes were selected simulations were run to determine the optimum capacitance value for the circuit, so that the current through the D3/D4 clamp is as small as possible during a high-voltage pulse and the voltage at the input to the amplifier has the least attenuation during the receive phase. The value selected

was 3 nF. After an initial prototype was constructed, it was found that the coupling capacitor to the input of the AD604 created a floating node, so a resistor was needed to center the node at 0 V. The resistor size selected was 50 Ω . This value was chosen for several reasons. The first reason was it's low Johnson thermal noise, given by

$$\frac{\bar{v}_i^2}{\Delta f} = 4kTR.$$

So, a 50- Ω resistor has 0.89 nV/ \sqrt{Hz} of thermal noise. The second reason for choosing 50 Ω is the high pass filter it creates with the 3-nF capacitor. The high pass corner frequency for this is approximately 1 MHz. The third reason for selecting 50 Ω was to terminate the 50- Ω coaxial cable from the transducer at high frequencies. After the addition of the 50- Ω resistor, a second set of simulations determined that 3 nF was still the optimum value.

Figure 20 shows the current distribution when a high-voltage pulse is applied to the high-voltage input. Figures 19 and 21 show the main function of the circuit. Figure 19 shows a high-voltage pulse being applied to the transducer. The high-voltage pulses used in simulations are single-cycle sine waves multiplied by raised-cosine window functions. Figure 21 shows the input of the amplifier being limited to by the D3/D4 clamp ± 1 V when a 600-V pulse is applied to the transducer. Figure 22 shows the attenuation of a signal received from the transducer at the input of the amplifier.

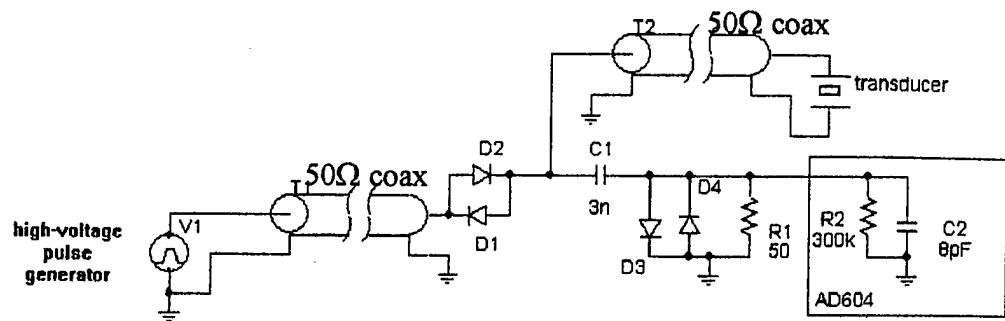


Figure 18. High-Voltage Protection Circuit Diagram

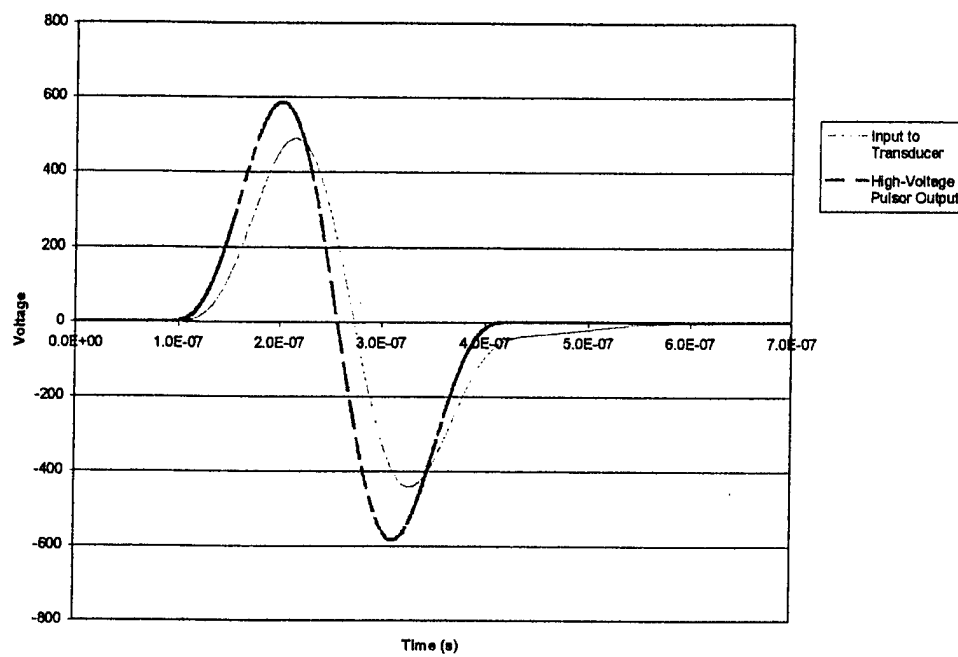


Figure 19. Simulated Voltage Across the Transducer When High-Voltage Pulse is Applied

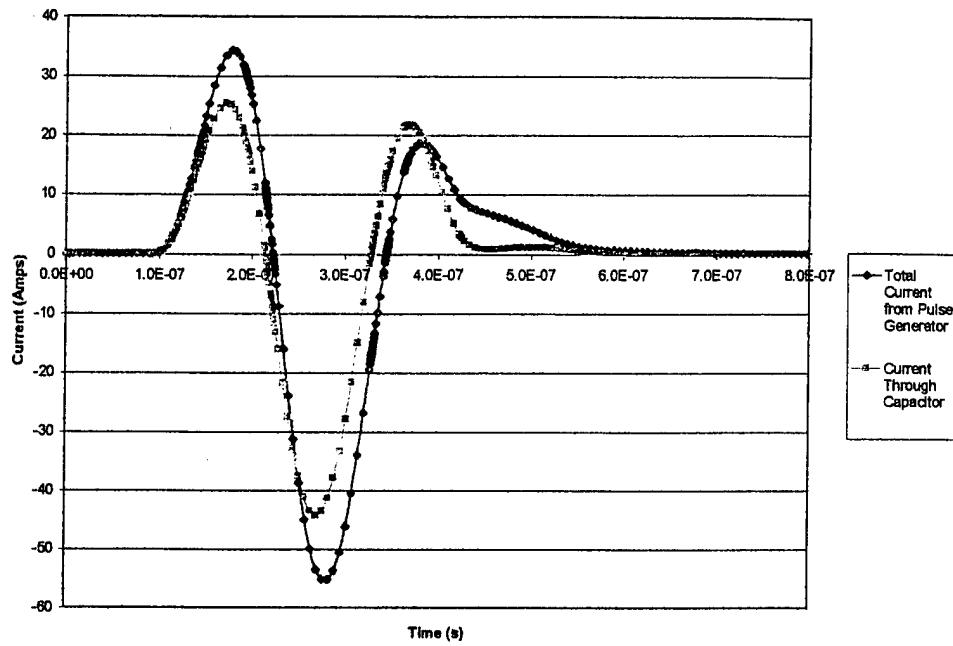


Figure 20. Current Through D1/D2 Clamp and C1 When High-Voltage Pulse is Applied

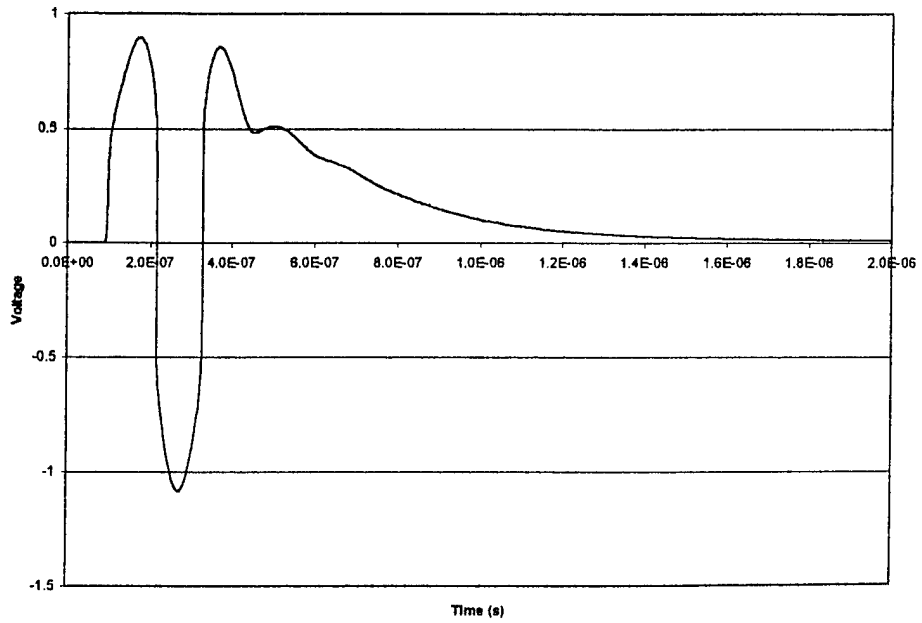


Figure 21. Voltage at Input of Amplifier When a High-Voltage Pulse is Applied

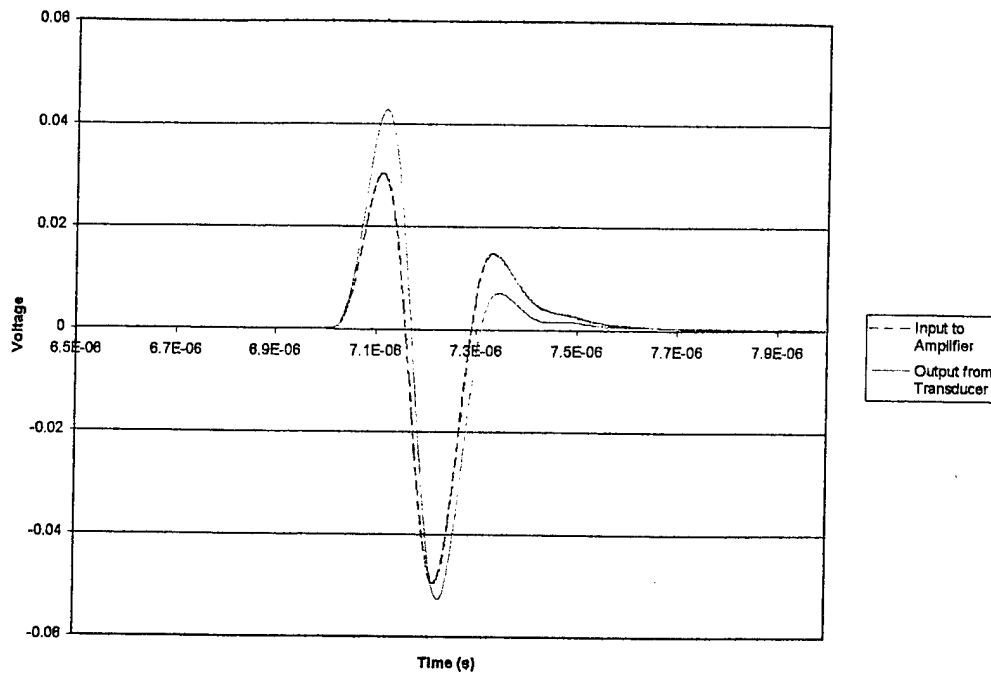


Figure 22. Voltage at Output of Transducer Compared to Voltage at Input of Amplifier when a Received Signal is Simulated

3.4 AD604 Peripheral Components

The Analog Devices part AD604 [8] is a 24-pin chip with two ultra-low noise, variable-gain amplifiers. Each amplifier has 11 pins of its own and there are two pins that are shared by the two amplifiers. The basic architecture of each amplifier includes an op-amp in a non-inverting configuration with a gain of either +14 dB or +20 dB depending on whether the feedback pin (FBK) is shorted to the pre-amp output pin (PAO) or left unconnected. The pre-amp is followed by a differential attenuating resistive network with inputs +DSX and -DSX. This network is internally connected to an amplifier with a gain of +34.4 dB which is connected to the output pin (OUT). The attenuation of the resistive network is set by the gain control pin

(VGN). Each amplifier has three power supply pins, consisting of a positive supply (POS), a negative supply (NEG), and a ground (COM). The shared pins are the common mode output voltage level pin (VOCM) and the gain control reference voltage (VREF).

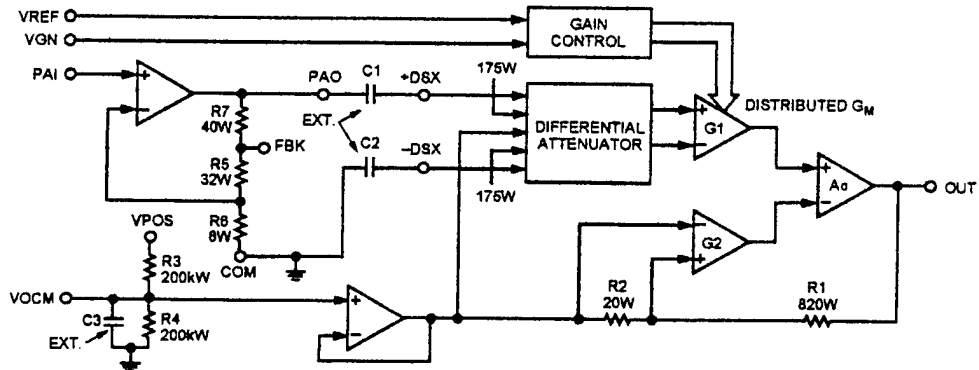


Figure 23. Simplified Block Diagram of Single Channel of AD604 [8]

For this application it was determined that the +14 dB gain would be used by shorting the FBK pin to the PAO pin because the lower gain allows for a larger signal to be amplified in case the amplitude from the transducer was greater than expected. The +DSX and -DSX inputs are capacitively coupled to the PAO and ground respectively. The +DSX and -DSX inputs both have an input resistance of $175\ \Omega$, so the coupling capacitor sizes must be chosen so the high-pass corner created by the capacitors and resistance is less than 2 MHz. 20-nF capacitors were chosen to set the corner at 50 kHz, so that the input would not be affected by the roll-off in the signal bandwidth and so the amplifiers would not distort the signal. The VOCM has an internal reference circuit that sets the common mode of the output to 2.5 V when a capacitor is connected between the VOCM and ground, so a $0.1\text{-}\mu\text{F}$ capacitor was

used. The VREF pin does not have this internal reference, so a 2.5-V external reference is generated by a ZETEX ZRA250A03 micro-power voltage reference, as shown in Figure 24. The output of the AD604 is centered about 2.5 V set by the VOCM voltage, but for the Pentek model 9158 A/D converter the input is assumed to be centered about 0 V. To remedy this, the output of the AD604 is capacitively coupled to the second stage amplifier. The gain control (VGN) is provided by an external power supply or signal generator.

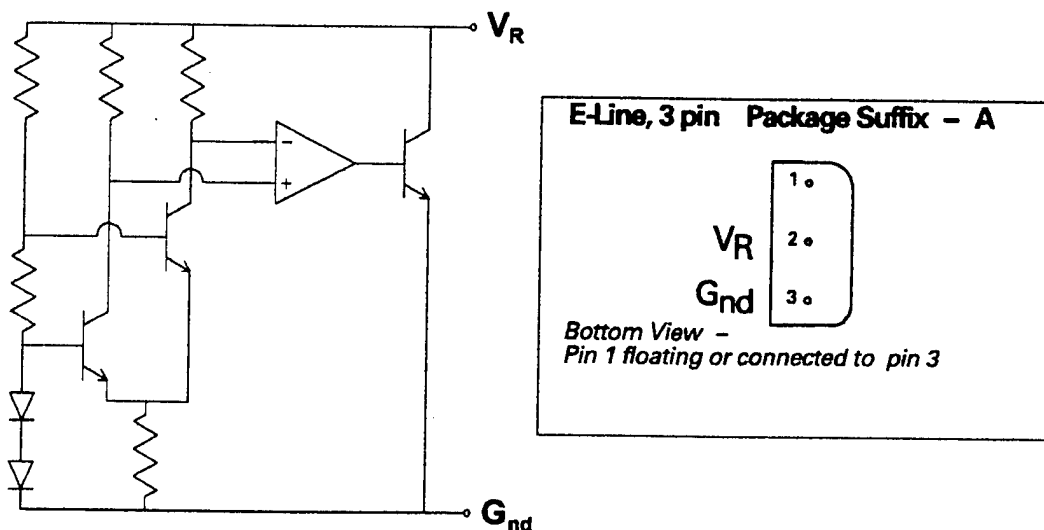


Figure 24. ZRA250A03 Circuit Diagram and Package [12]

3.5 Second Stage Amplifier Design

In order to fill the full scale range of the A/D converter, i.e. -1 V to +1 V a gain of at least +20 dB was required. Since the polarity of the signal in this application does not matter, and inverting amplifiers have superior performance to non-inverting, an inverting op-amp configuration was used, as shown in Figure 25.

Since the output of the AD604 is optimally terminated by a $500\text{-}\Omega$ resistor, the resistance values used were $500\ \Omega$ and $5000\ \Omega$. The coupling capacitor was selected to be 3 nF between the output of the AD604 and the $500\text{-}\Omega$ resistor. This sets the high-pass corner at 100 kHz . The gain-bandwidth of the op-amp is required to be over 60 MHz , so at a gain of $10x$, the bandwidth of the amplifier is at least 6 MHz . The National Semiconductor CLC428 was selected for its low noise characteristics, 160-MHz gain-bandwidth, and the fact that there are two amplifiers per chip. A $50\text{-}\Omega$ resistor was added to the output of the amplifier to isolate it from the large capacitance of the coaxial cable to the A/D converter. This value was selected because it provides proper termination for the cable.

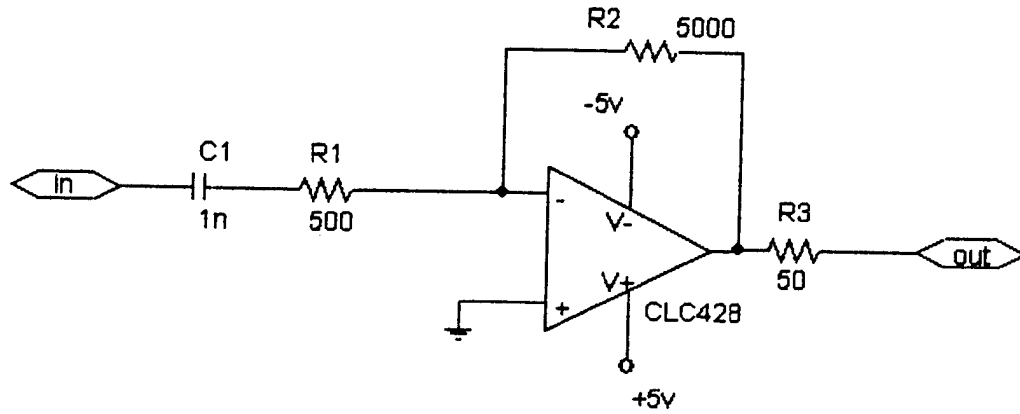


Figure 25. Inverting Op-amp Configuration.

3.6 Noise Requirements

The maximum input to the A/D converter is 1 V. The maximum noise at the output to the amplifier is therefore 55 dB less than 1 V or 1.7 mV. The maximum noise at the input of the amplifier when it is at its highest gain setting is 65 dB less than 2.5 mV, or 1 μ V. Since there are 11 transducers creating each transmit pulse the input referred noise can be $\sqrt{11}$ more than 1 μ V, or 3.4 μ V.

3.7 Entire Circuit Simulations

All simulations were done using the SPICE models of the parts available on the manufacturers web-sites. Figure 26 shows the circuit model for the entire circuit. The magnitude response of the interface circuit from the transducer input to the output with the high-voltage input grounded is shown in Figure 27. The phase response is shown in Figure 28. Figures 29 and 30 show the magnitude and phase response for the signal bandwidth. By taking the negative derivative of the phase the group delay was found for Figure 31. Figure 32 shows the input referred noise of the circuit for the highest gain setting verses frequency. The total input referred noise was found by integrating the square over the signal bandwidth and taking the square root. This value is 1.5 μ Vrms. The magnitude response and phase response were zoomed in to the 2 to 4 MHz signal band to show the flatness of the magnitude response and linearity of the phase response. Figure 33 shows the response of the circuit when a high-voltage is applied and a receive signal is simulated within 5 μ s of the transmit pulse.

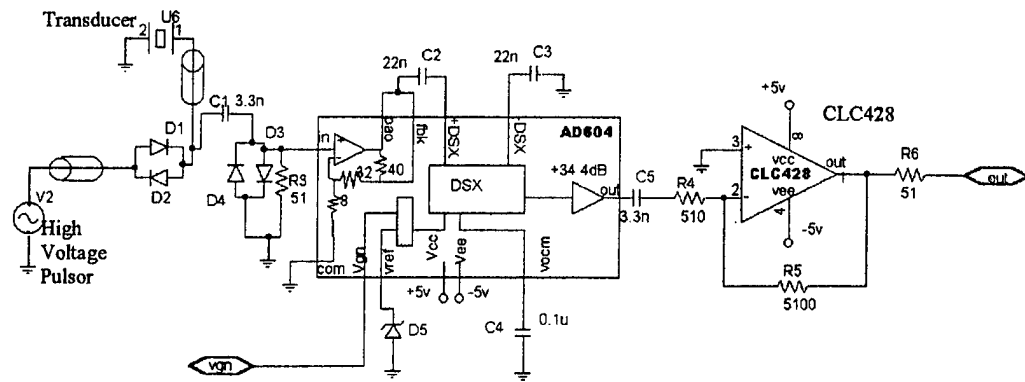


Figure 26. Entire Circuit Schematic

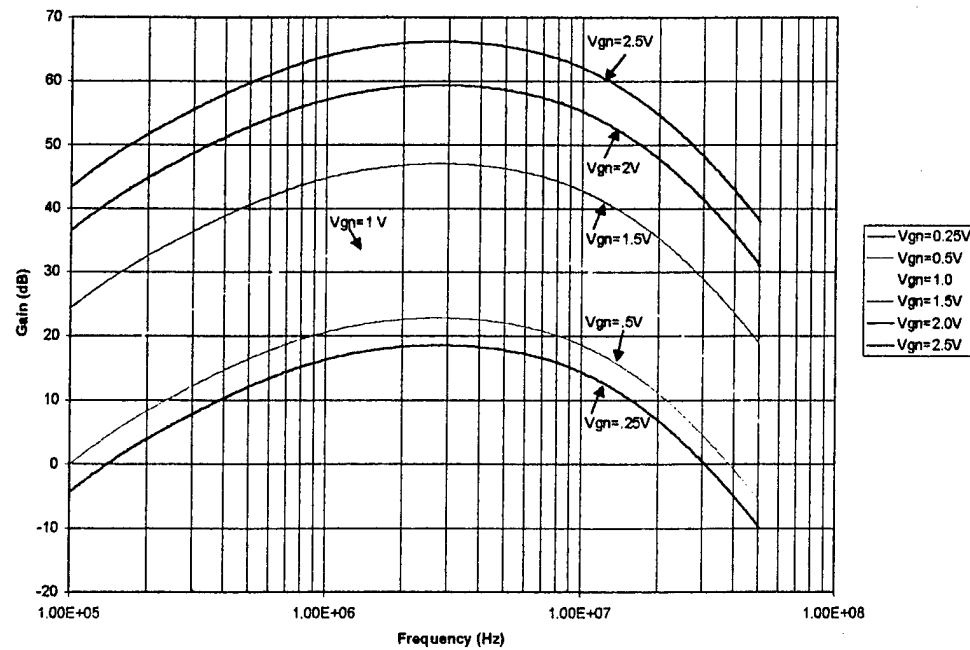


Figure 27. Magnitude Response of Circuit.

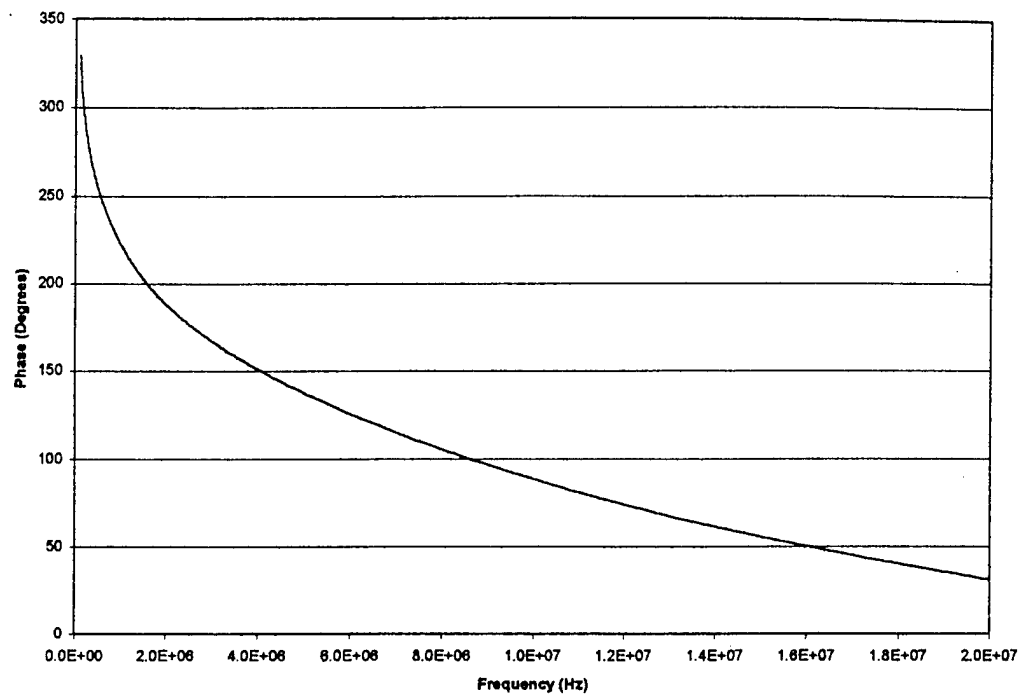


Figure 28. Phase Response of Circuit

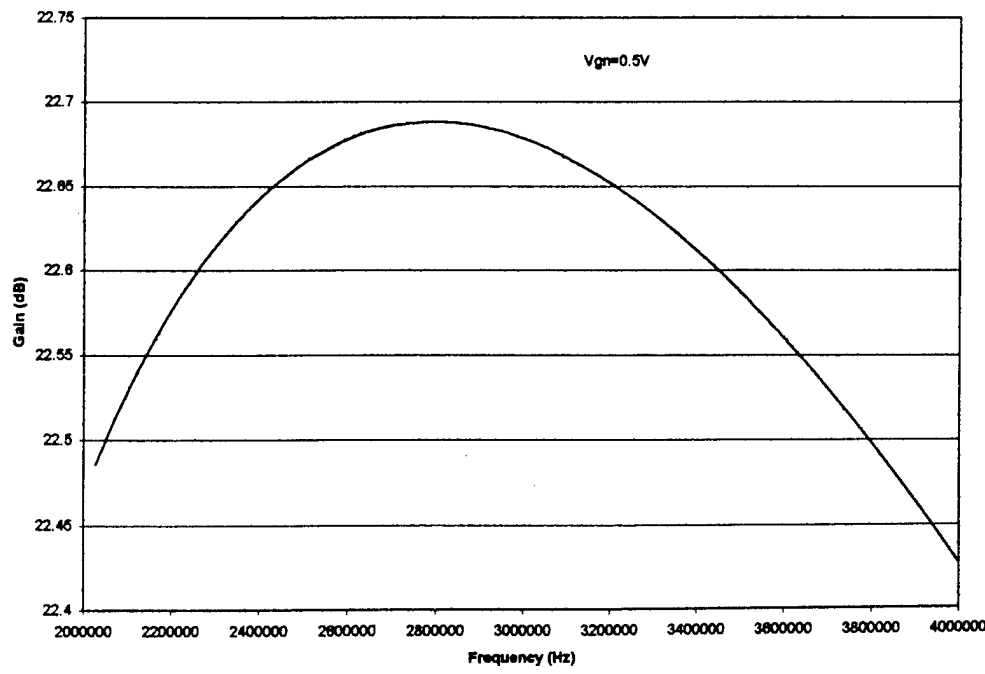


Figure 29. Magnitude Response in 2-4 MHz Signal Bandwidth

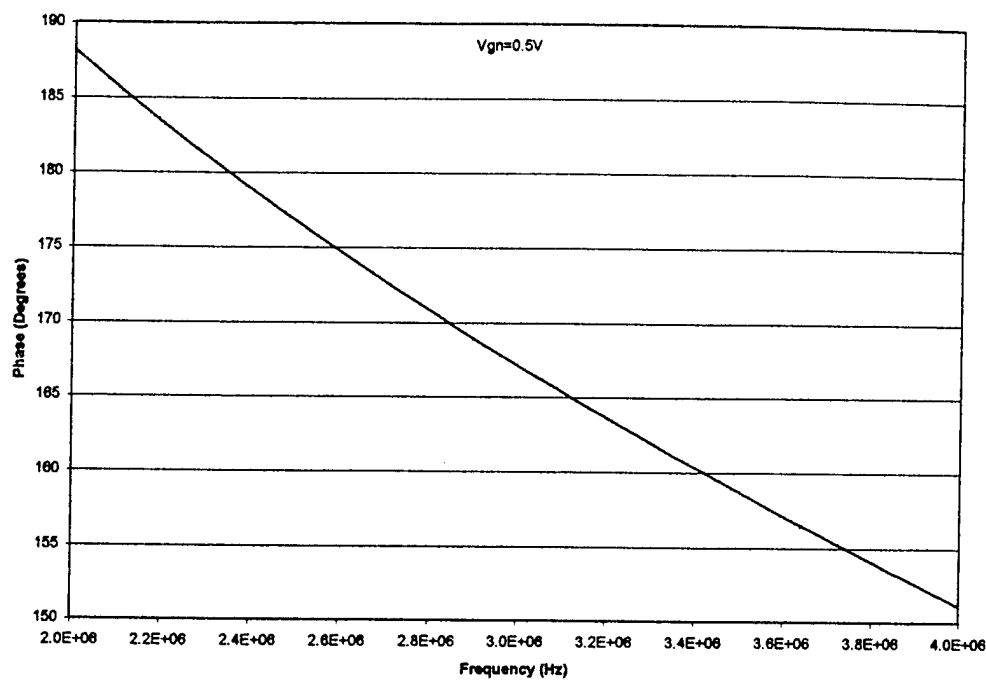


Figure 30. Phase Response for 2-4 MHz Signal Bandwidth

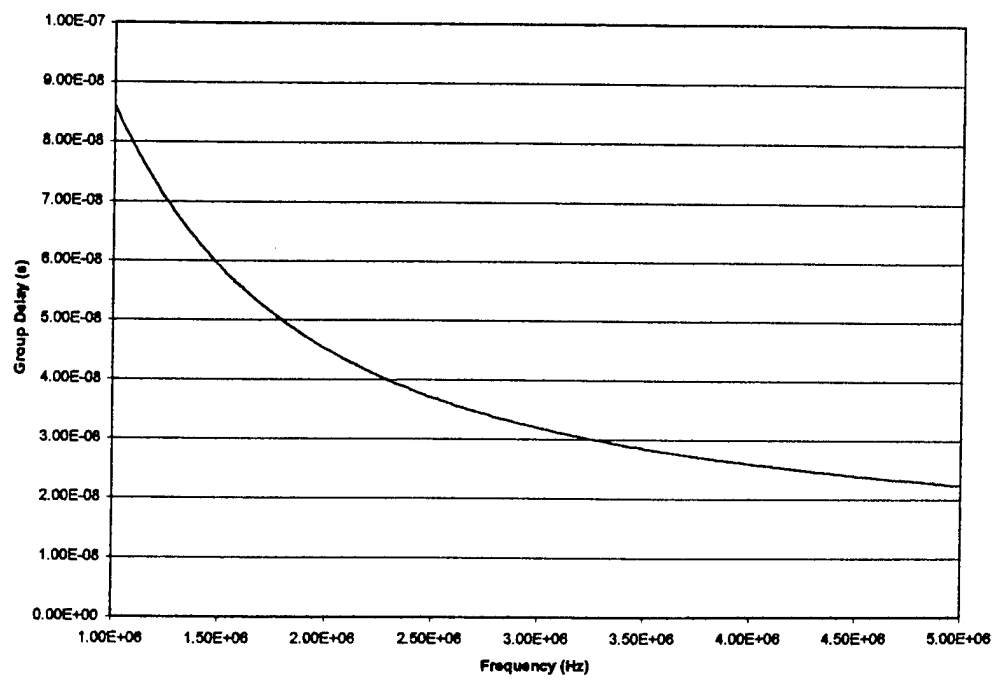


Figure 31. Group Delay of Circuit

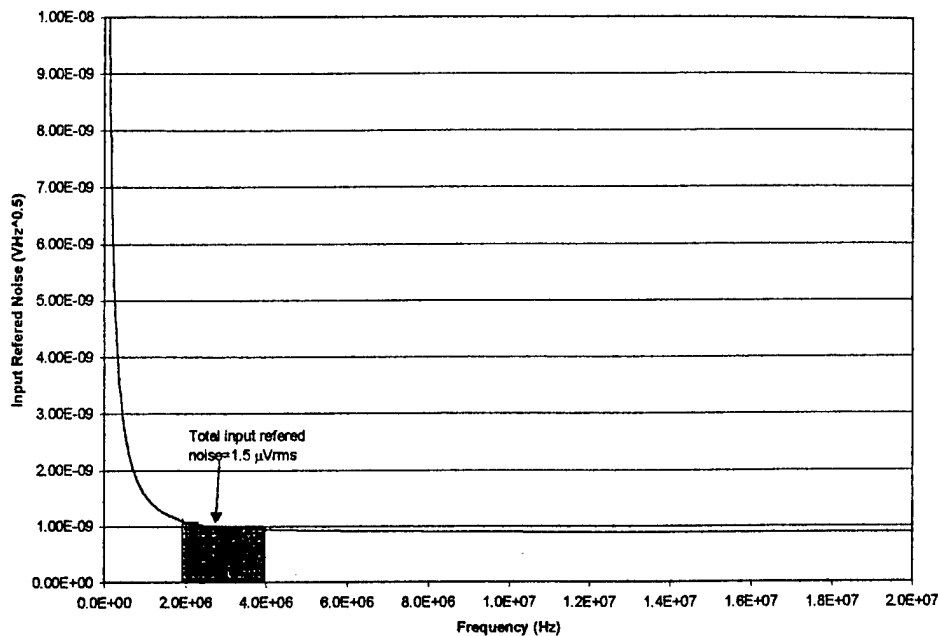


Figure 32. Input Referred Noise vs. Frequency

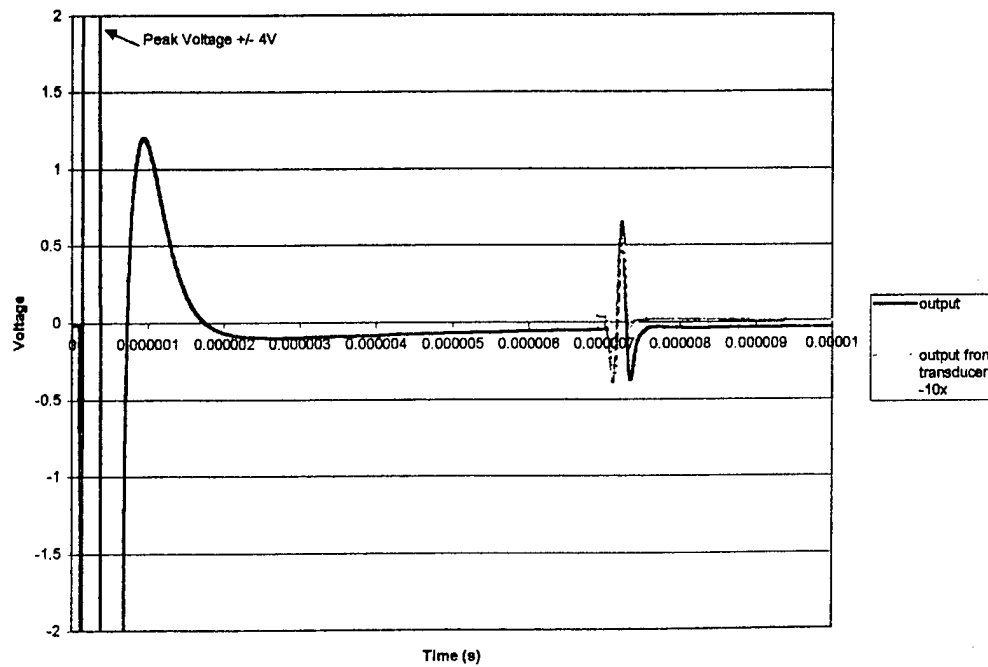


Figure 33. Output of the Circuit when a High-Voltage Pulse is Applied Followed by a Receive Signal

4. FABRICATION AND TEST

4.1 Prototype Design and Fabrication

A two-channel prototype of the front-end circuitry was designed to verify the simulations. Since both the AD604 and CLC428 are dual chips, a two-channel design was the logical choice, but requires careful consideration of cross-talk. When designing a system in discrete components as with any real world electrical design, electromagnetic interference and signal coupling are major concerns. By using surface mount components, there is less inductance in the leads of devices which means there is less of an antenna to pick up radio frequency interference. Using a ground plane with surface mount components helps reduce both interference and coupling. The ground plane does not allow radio waves to couple into the circuit through loops created by power supplies going through chips. The ground plane also reduces the fringe fields of components, so the components do not interfere with each other and create oscillations.

Printed circuit board (PCB) trace placement is extremely important for reducing interference. Traces carrying small signals must stay far away from traces carrying large interference signals to avoid capacitive coupling. Making sure that traces do not form loops and/or ground plane islands reduce the inductance that picks up external electromagnetic radiation.

In this design, special attention was given to power supply lines. Because of the large gains used, any power supply noise or interference would be amplified

tremendously and appear in the output signal. Using bypass capacitors for each chip filters out some of the high frequency noise going into the chips. Also, it is extremely important to not have the power supply lines too close to the output of the amplifiers. This keeps the output from coupling to the power supply, creating a feedback path which could lead to instability and oscillations.

Ground connections are also very important. It is very easy to inadvertently make loops in ground connections. Special care must be taken to ensure that ground connections are made to the correct ground. Signal grounds connected to instrument grounds, etc. can make ground loops via the building steel. Ground loops can be very inductive, and the AD604 is very sensitive to inductance on the ground node.

Choosing the proper technology for each of the components in the design involved some trade-offs. For all of the resistors in the design, surface-mount thick-film chip resistors were used. These were selected because of the availability of sizes needed, small size, and low cost.

The capacitor in the high voltage protection circuit is a ceramic disc capacitor rated at 2 kV. There are no surface mount capacitors available that can withstand the voltages used in this application. The rest of the capacitors in the design are surface-mount multi-layer ceramic chip capacitors, which have adequate high frequency performance. Thin film capacitors were used for a preliminary prototype, but when soldering them to the PCB they were very easy to melt and some times did not have the correct capacitance after soldering. Ceramic is much more resistive to heat, and therefore much easier to solder to the PCB.

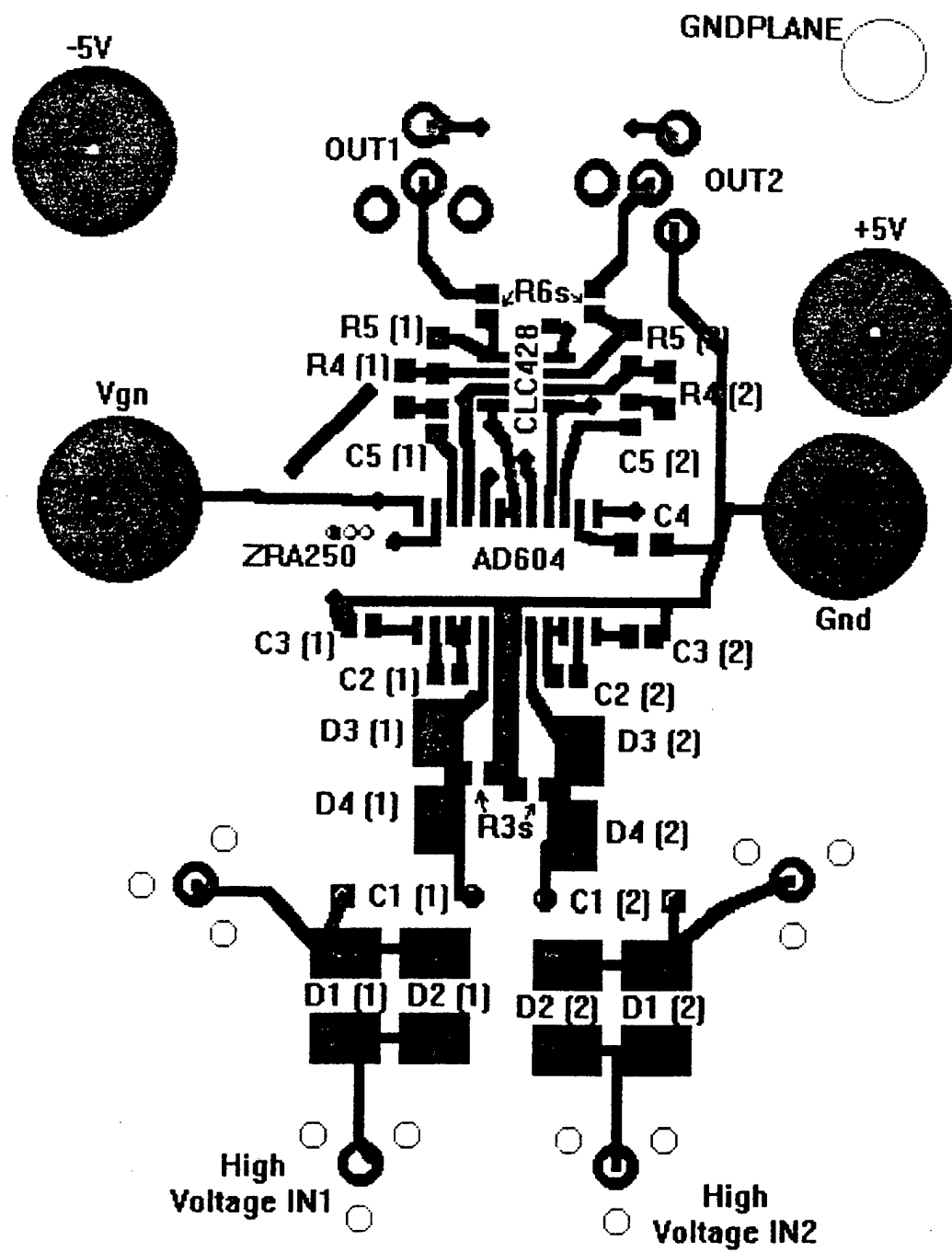


Figure 34. Component Side PCB Layout

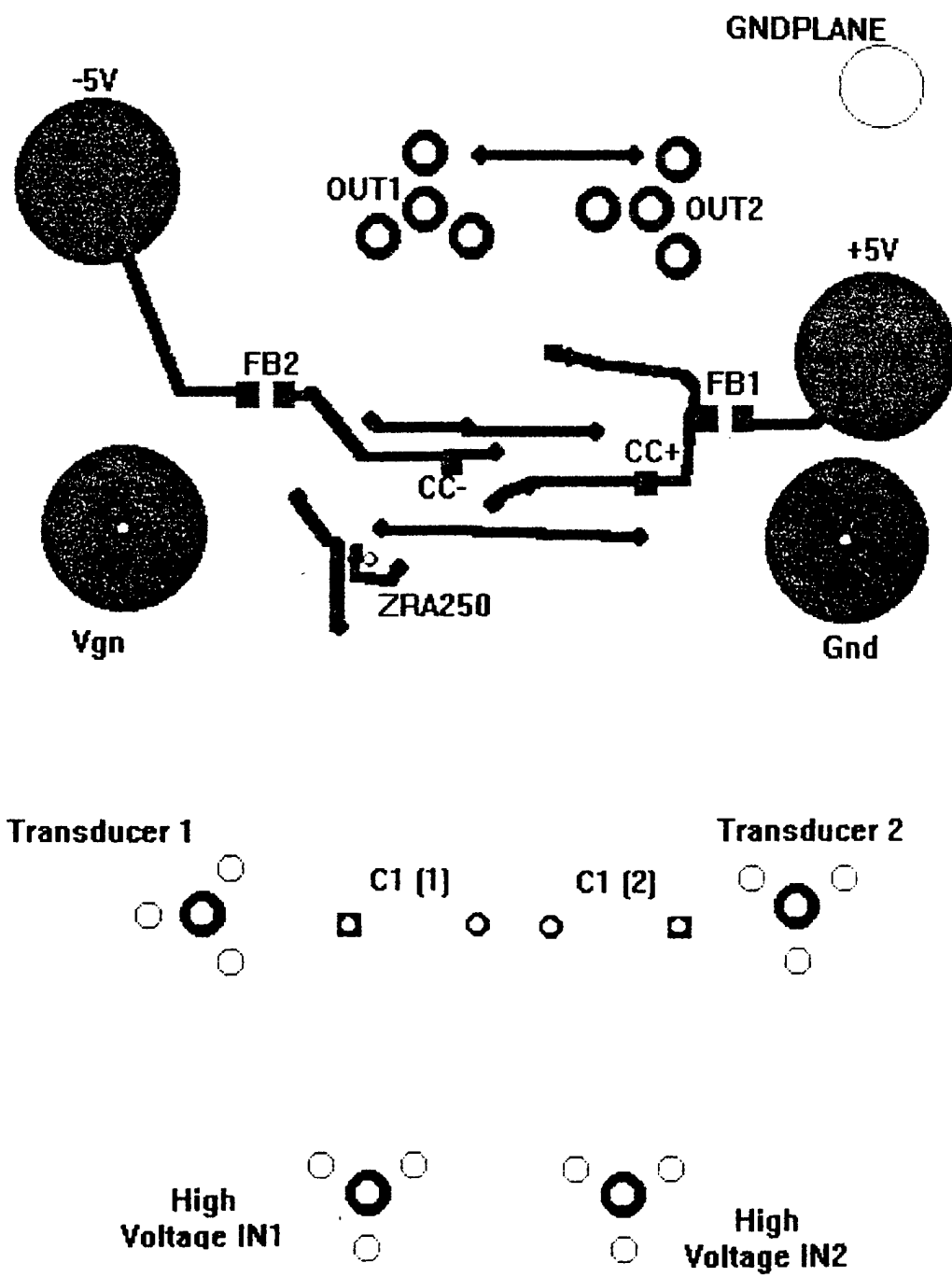


Figure 35. Solder Side PCB Layout

The 24-pin Small Outline Integrated Circuit (SOIC) package of the AD604 variable-gain amplifier was chosen because it is surface mount, relatively small, and readily available. The CLC428 op-amp is packaged in an 8-pin SOIC. The power supplies, grounds, and gain control voltages are all connected to the board using banana jacks. The transducer input, high-voltage input, and output are connected to the board by $50\text{-}\Omega$ PC mount BNC connectors.

The printed circuit board was designed using the MicroSim PCBoards program, a part of the MicroSim DesignLab suite. The board has two layers with a minimum trace spacing of 8 mils (8/1000 inch). Traces in this design were not required to be very dense, so a trace width of 30 mils was used for all traces. The boards were fabricated using a T-Tech Quick Circuit milling machine. The copper traces were milled out of the double-sided copper clad boards, and the ground plane was left where the boards were not milled. The boards were populated using a PACE soldering station with tools for surface-mount soldering.

4.2 Test setup

The two-channel prototype was tested in a lab environment. A Hewlett Packard (HP) E3631 triple-output power supply was used to provide ± 5 V, ground, and the gain control voltage, V_{gn} . The +15-V output was set to +5 V, the -15-V output was set to -5 V, and the +6 V output was varied to set the gain. An HP 3314A function generator/arbitrary waveform generator was used to generate sine waves used in the tests. This model was used because of its ability to generate signals from

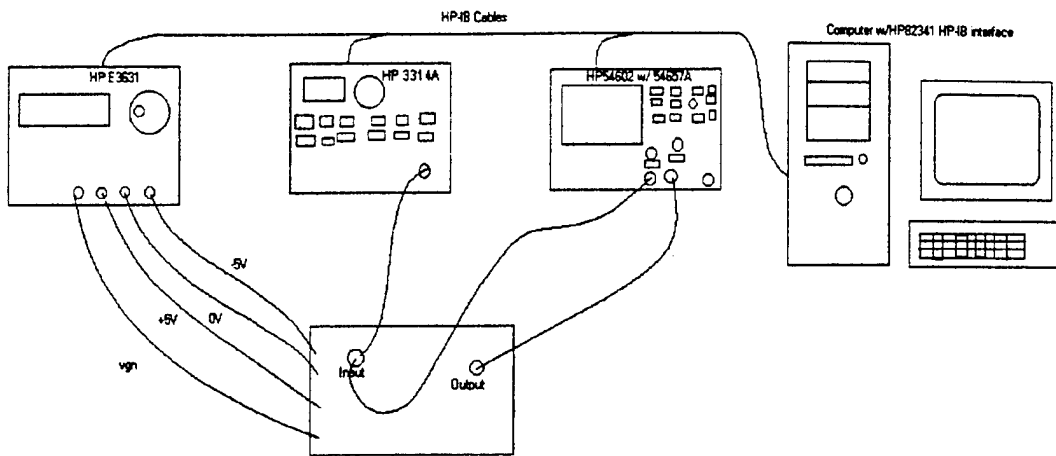


Figure 36. Test Setup

0.1 mVp to 10 Vp. All measurements were done using an HP 54602 oscilloscope with an HP 54657 HP-IB measurement and storage module connected. All three of these instruments were connected to a Pentium PC with an HP 82341 HP-IB interface card.

Banana plugs were used to connect the power supplies and gain control voltages to the power supply. BNC cables were used to connect the signal generator and oscilloscope to the circuit. Since the output was affected by capacitive loading, a relatively short 1-ft. BNC cable was used to connect the output of the circuit to the oscilloscope. The length of the other two BNC cables that connect from the function generator to the input of the circuit and from the input of the circuit to the oscilloscope did not affect the performance of the circuit.

4.3 Frequency Response Tests

A program was written in Visual Basic in Excel to control stimulus and

collect data for measurement of the frequency response. The source code is located in Appendix B. The HP-IB interface routines were called to control the oscilloscope and function generator to find the magnitude and phase response of the circuit. The macro sets a frequency on the function generator, then it auto-scales the oscilloscope so the input and output signals are measurable by the scope at which point it queries the oscilloscope to find the amplitude of the input and output signals and the phase difference between channel 1 and channel 2. The macro then repeats this procedure for all of the frequencies to be tested.

Before taking measurements, the amplitude of the input sine wave from the signal generator was adjusted so that the output was 1 Vp-p when a 3-MHz sine wave was applied to ensure that the output did not saturate the CLC428 op-amp. The program was run for five different values of V_{gn} , the gain control voltage. The results of the magnitude measurements are shown in Figure 37 and 38. Figure 38 shows that the variation in gain over the 2-4 MHz signal bandwidth is less than 0.7 dB. Figure 39 shows the 3-dB bandwidth for several gain settings, calculated from the magnitude response of the circuit from Figure 37.

The phase response for when $V_{gn}=0.5$ V is shown in Figure 40 and 41. Figures 39 and 40 show the magnitude and phase response of the circuit showing more detail around the signal bandwidth. In Figure 41, a logarithmic curve fit was found to accurately match the phase response in the signal bandwidth. From this regression the estimated group delay was found by computing the negative derivative of the phase with respect to frequency. This result is shown in Figure 42.

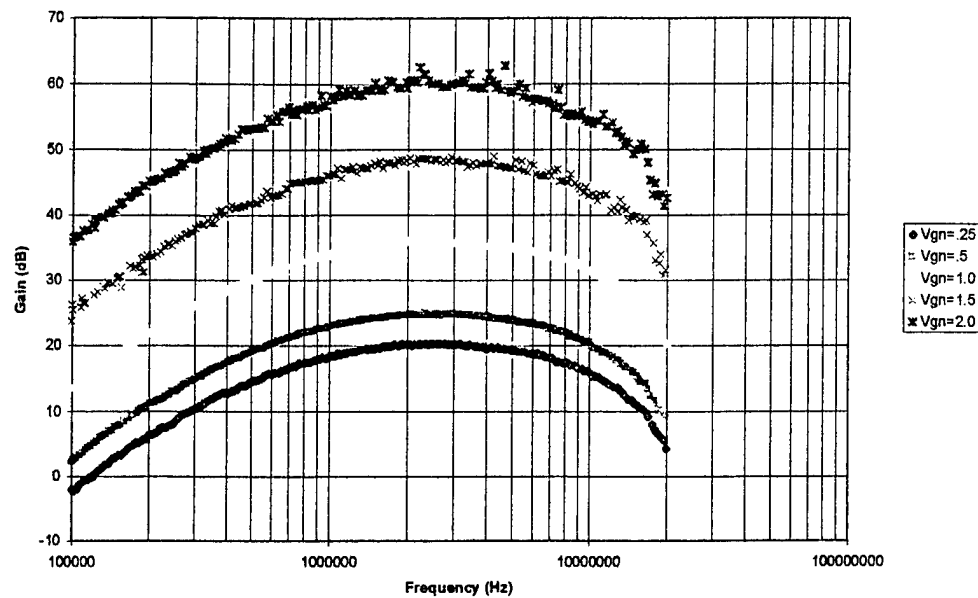


Figure 37. Measured Magnitude Response for Several Gain Settings

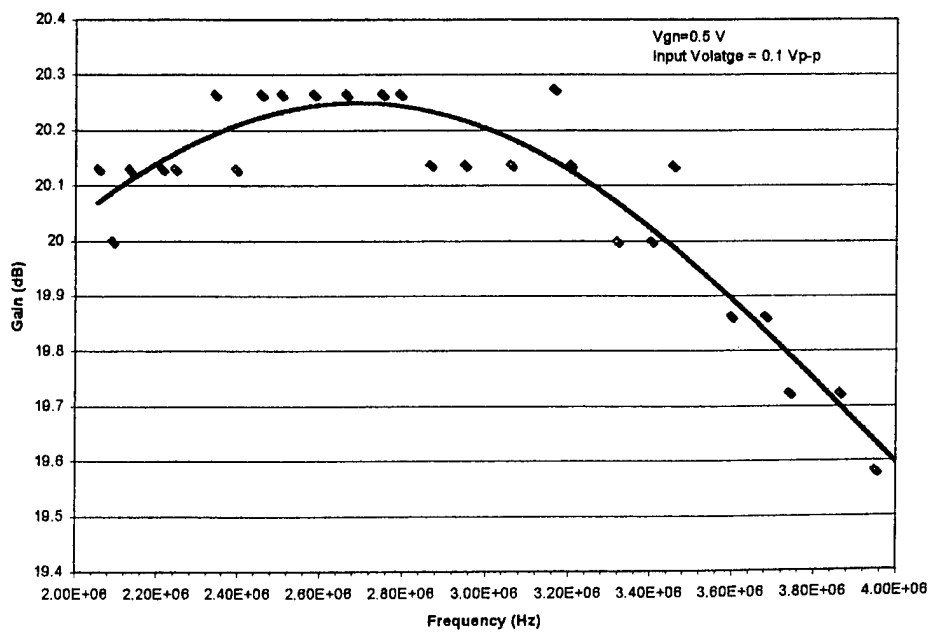


Figure 38. Measured Magnitude Response for 2-4 MHz Signal Bandwidth

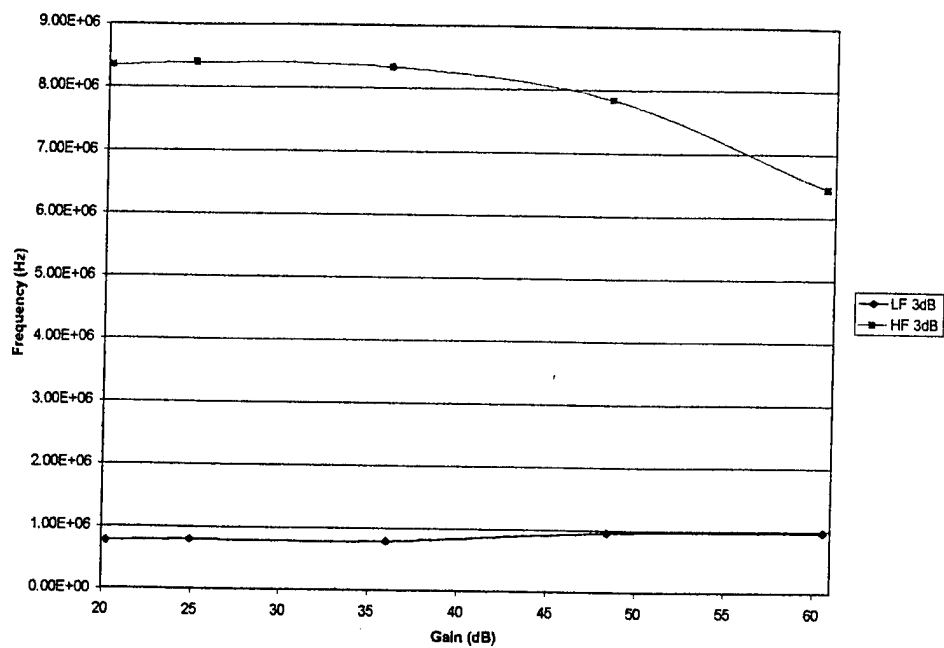


Figure 39. Measured Bandwidth versus Gain

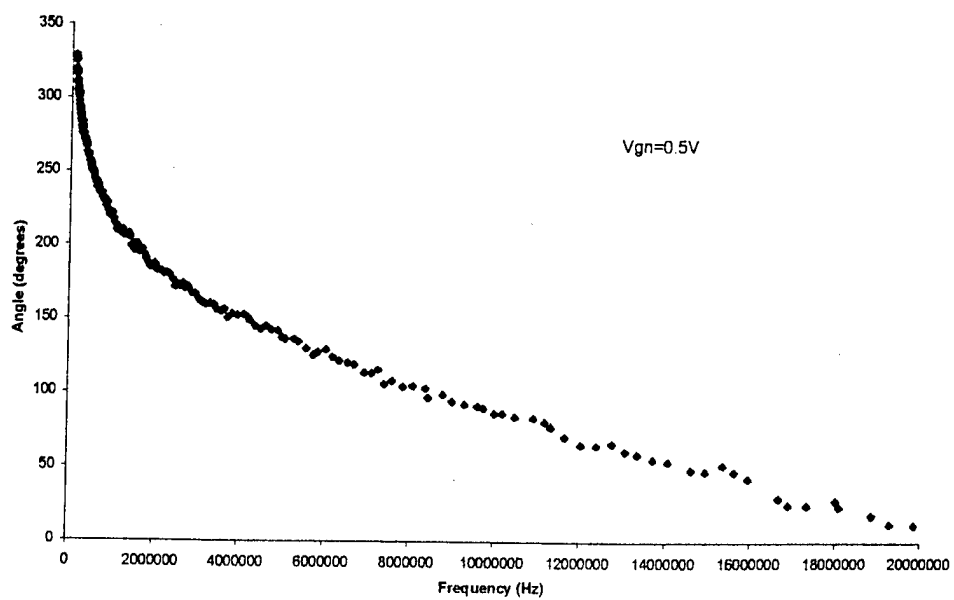


Figure 40. Measured Phase Response

4.4 Gain Control, Noise, and Cross-Talk Tests

The dependence of gain on the gain control voltage was measured. The setup was exactly the same as for the frequency response. The function generator was set to a 5-mVp-p, 3-MHz sine wave and connected to the transducer input of the circuit. Measurements were taken as the gain control voltage was increased from 0.25 to 2.27 V. At the higher gain settings (greater than 55 dB), the CLC428 op-amps began to saturate, and the function generator amplitude was decreased to 0.5 mVp-p. The results are shown in Figure 43.

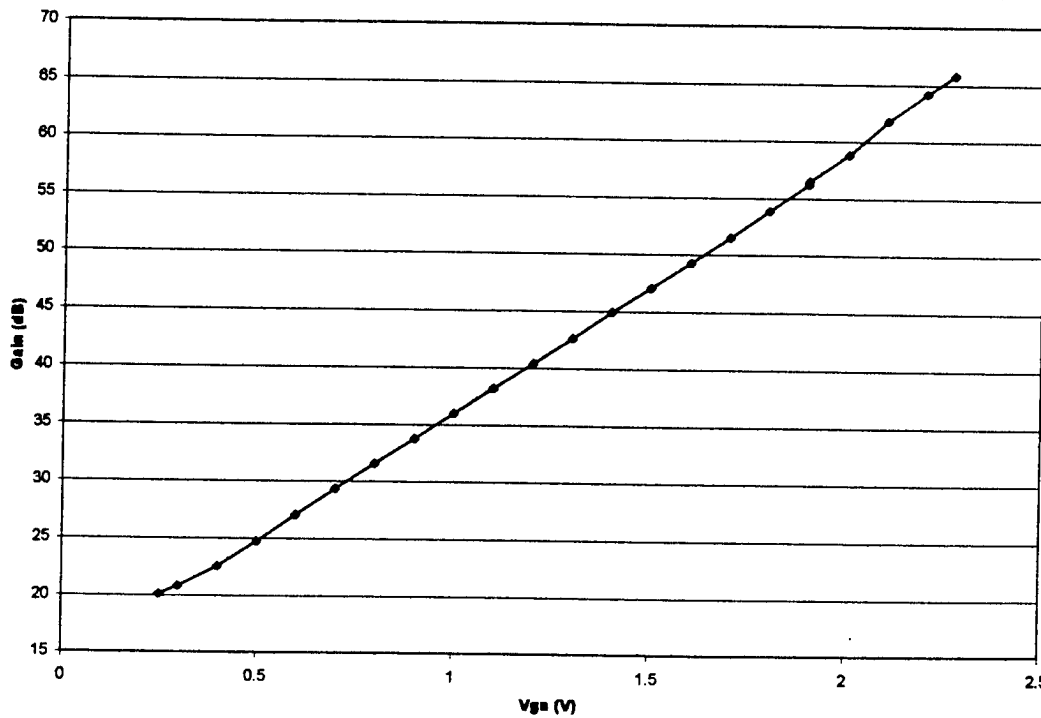


Figure 43. Gain versus Gain Control Voltage

A test was performed to determine the total input referred noise of the system. In this test, all of the inputs were tied to ground and the gain was set to maximum (65 dB). The output was then analyzed using the FFT function of the oscilloscope. The input referred noise in the circuit bandwidth was calculated by dividing the FFT output by the bandwidth of each point and the gain in the signal band. The total noise was found by integrating the mean square values over the circuit bandwidth. The total input referred noise was found to be $2.3 \mu\text{V}_{\text{rms}}$. The FFT is shown in Figure 44.

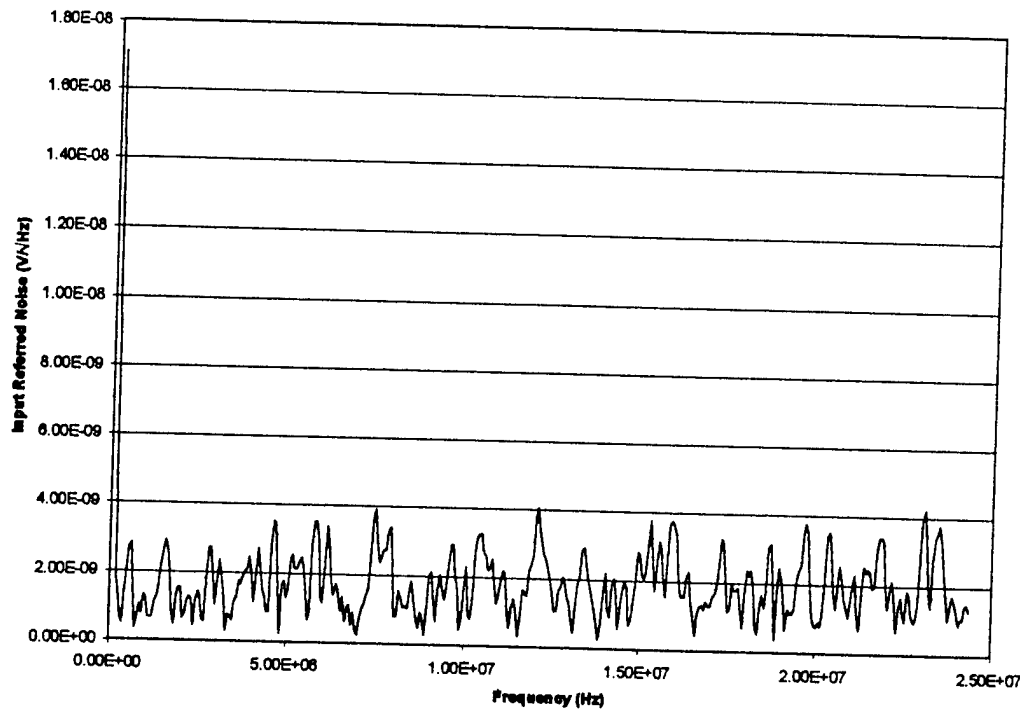


Figure 44. FFT Showing Input Noise Spectrum

The cross-talk between the two channels of the prototype was measured. In this test, a sine wave was applied to the transducer input of one channel of the circuit, with a magnitude such that the output was 2 Vp-p. The output from the second

channel was measured and compared to the output of the first channel. The cross-talk was then measured for several gain settings and the results are shown in Figure 45. These measurements are very close to the specifications for cross-talk in the AD604.

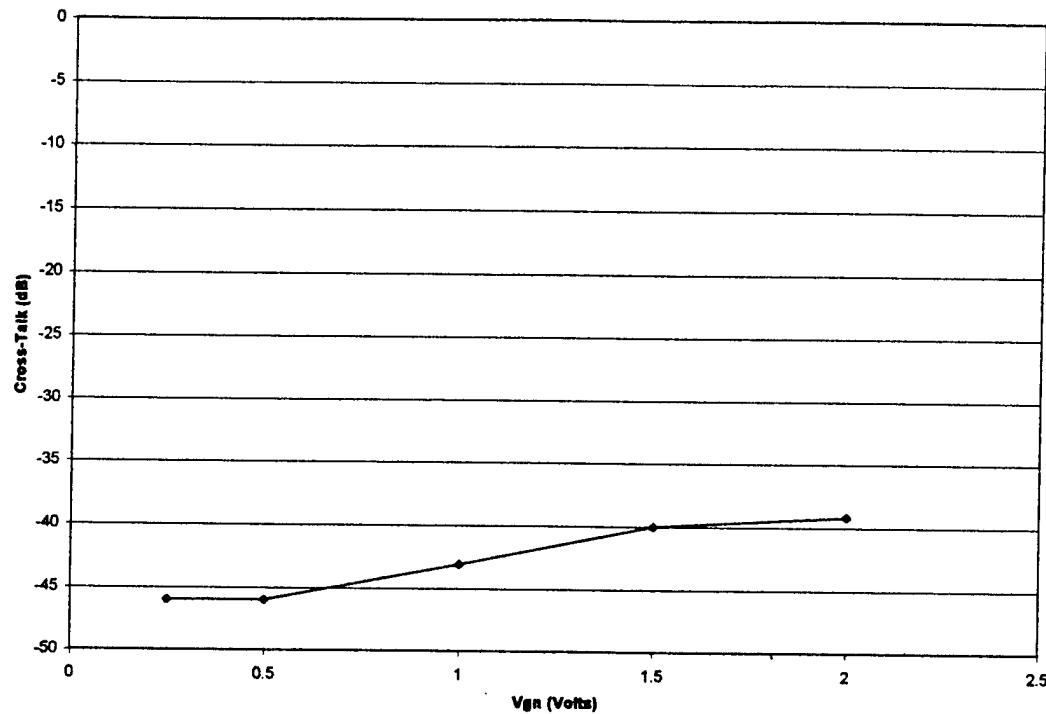


Figure 45. Measured Cross-Talk

4.5 High-Voltage Protection Tests

The high-voltage protection circuitry was not accurately tested because the function generators necessary to apply high voltages were unavailable. With a 10-V pulse applied to the high voltage input, the voltage at the transducer output was about 9 V and at the input of the amplifier was about 1 V. This result was similar to what was expected. A qualitative trial at the Cleveland Clinic, using a real transducer and

the actual high-voltage generator, was performed and the high-voltage protection circuitry appeared to work properly.

4.6 Discussion

The results of the frequency response tests performed on the circuit were remarkably close to the simulation results. Figures 46, 47, and 48 show a comparison of the two results. At lower frequencies, the shape of the magnitude response of both simulation and test are very much the same, but at the higher frequencies the test results fall off more rapidly than the simulation. This roll-off can be explained by parasitic capacitance in the feedback path of the op-amp and in the coaxial cables both of which create low-pass filters. The prediction of gain for a given level of gain control voltage is very good at higher gain settings, with some inaccuracy at lower settings.

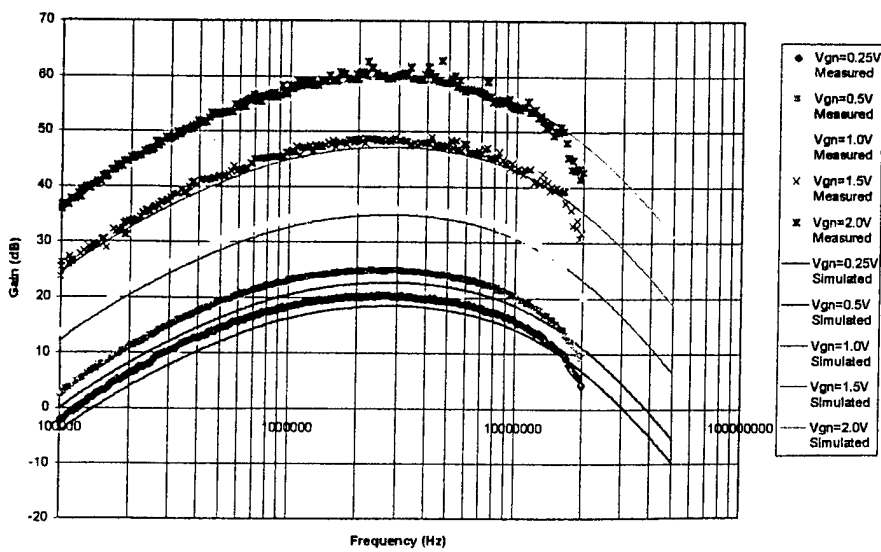


Figure 46. Simulated Magnitude Response Compared to Measured Response

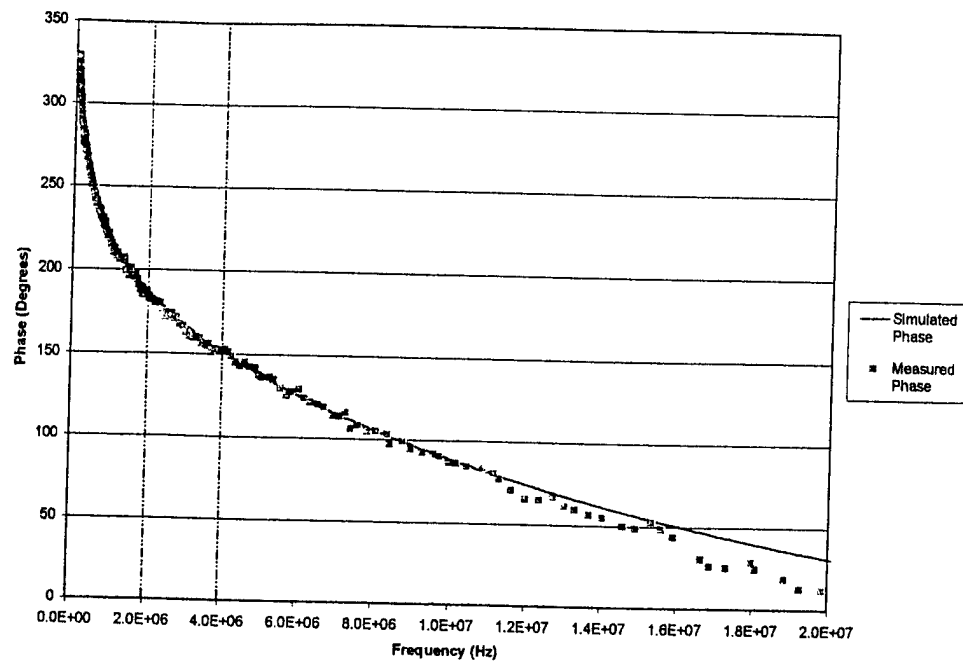


Figure 47. Simulated Phases Response Compared to Measured Response

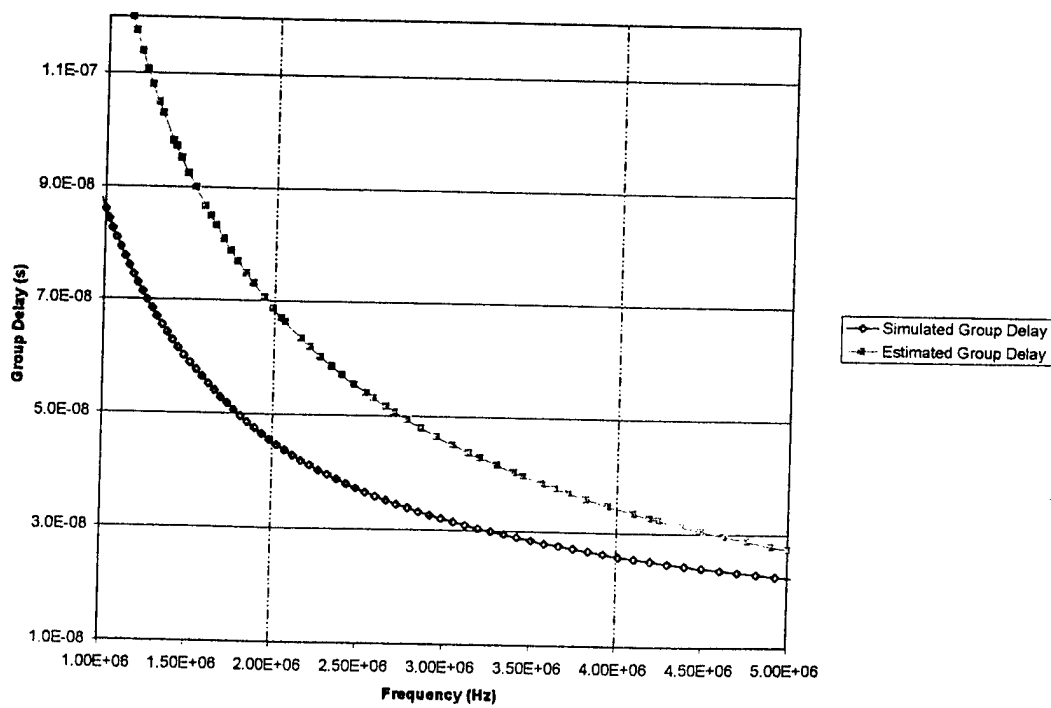


Figure 48. Simulated Group Delay Compared to Measured Response

The phase response is also affected by parasitic capacitances and agreement between simulation and measurement is best at lower frequencies. The measured group delay is greater than the simulations primarily because of the coaxial cables. Of key importance is the variation of the group delay over the signal bandwidth. The simulated variation is about 20 ns, while the measured variation is about 30 ns. This quantity in the test is less than 10 ns more than in simulation. The input referred noise in the signal bandwidth was twice as much as the simulation which is still within specifications.

The bandwidth of the circuit is a bit larger than what is necessary for this application. The bandwidth extends from 1 MHz to 8 MHz at the low gain setting and from 1 MHz to 6 MHz at the high gain setting. This large bandwidth allows for a flatter response in the signal band, but it also allows more total noise in the output signal.

The gain control voltage controls the gain in a linear-in-dB fashion as suggested by the AD604 data sheet [7], but there is a slight non-linearity at both the low and high end of the gain settings. When the signal that controls the gain is created, this non-linearity will need to be taken into account.

Project: Cleveland Clinic 3-D – Mechanically Steered Phased Array Probe
Subcontract #: _____
Report: Critical Issues Analysis
Date: September 27, 1999
Written by: Clyde Oakley
Organization: Tetrad Corporation
Address: 357 Inverness Drive South
Suite A
Englewood, CO 80112
Phone: 303-754-2315
FAX: 303-754-2329
Email: coakley@tetracorp.com

INTRODUCTION:

The purpose of this report is to describe the major technical risks associated with the completion of the objectives of the subcontract referenced above and to outline the technical approach proposed by Tetrad to ameliorate these risks. The objective of the program is to produce a working 64-element phased array that can be steered mechanically in the plane perpendicular to the array scan plane. Requirements are laid out in the specifications attached as Appendix A.

The main objectives of the probe are as follows:

- The acoustical design must be capable of producing good images over a 90 degree sector angle without excessive artifact.
- The probe must have a life time consistent with completion of a thorough evaluation of the imaging system and probe.
- The phased array must be capable of achieving a high level of transmitted energy per element to achieve the high signal to noise ratio required for effective imaging with a synthetic aperture that uses a relatively small transmitting aperture producing a diverging beam.

Each objective carries a degree of technical risk that must be addressed in the program. They are addressed separately in the sections that follow.

ACOUSTIC DESIGN ISSUES:

The mechanical steering of the array requires that it be housed inside a fluid-filled enclosure. This type of enclosure is commonly used for mechanically steered single element and annular array transducers. The acoustic problem is substantially more difficult for a phased array, however, because of the need to steer the beam through the enclosure.

Failure to achieve a good acoustic match can result in loss of signal level at steered angles and in reflections inside the probe that cloud the near field of the image.

Tetrad has begun analysis of the acoustic requirements for acoustic enclosures of varying shapes. The two shapes under most active consideration are cylindrical and a complex shape approximating a toroidal section. See Fig. 1.

The axis of the cylindrically shaped enclosure is ideally coincident with the axis about which the array moves mechanically. This causes the array to be positioned in at the same distance and with the same effective window shape regardless of the angle. This enclosure has the advantage that it is easy to construct and allows the array to be very close to the surface of the enclosure. It has the disadvantage that beam must be able to pass through at angles ranging from normal to more than 45 degrees from normal without losing significant energy or creating excessive reflections. This requires either that the enclosure be very thin or that it be well matched in both sound velocity and acoustic impedance.

The toroidal section would have one radius with a center of curvature on the axis about which the array moves mechanically and another radius centered at the center of the phased array. This creates a shape for which the rays deviate from normal by the smallest amount possible. The major advantage of this shape is that the acoustic property constraints are less severe if the enclosure is placed a reasonable distance from the array. One disadvantage is that the enclosure must be molded in this more complicated shape. More importantly, the enclosure is further from the array so any reverberation that does occur may produce artifacts deeper in the image.

The enclosure has two interfaces that must be considered. The first is between the fluid and the enclosure membrane and the second between the enclosure membrane and the body. Since most rigid membrane materials have sound velocities that are higher than most fluids, it is the fluid to membrane interface that is susceptible to critical angle problems. Fig. 2 is a plot of the critical angle for longitudinal waves as a function of the ratio of the membrane sound speed to the fluid sound speed. It is encouraging that the ratio of sound velocities must exceed 1.4 before critical angle drops below 45 degrees. A ratio of 1.4 is probably achievable in common fluids and membranes.

It is also important to consider how much reflection there is from the interface and how much energy will be transmitted through the membrane. To estimate this we have calculated the reflection and transmission coefficients for the inner interface ignoring mode conversion in the solid material. While this is not absolutely correct it will give us the right order of magnitude for evaluation. The results for a velocity ratio of 1.3 and an impedance ratio of 1.4 are shown in Fig. 3. Note that even with these ratios, the transmission loss is less than 0.3 dB and the reflection coefficient is less than -15 dB at all angles. This implies that the major loss of signal at an angle, other than the acceptance angle of the array itself, will result from the attenuation in the membrane. The path through the membrane for a 45-degree angle of incidence is larger than the path for normal incidence.

Selection of fluid is also important. The velocity and impedance must match the membrane reasonably well; the attenuation must be such that the reverberations die off quickly but low enough that signal to noise ratio is not needlessly reduced. Some fluids also are more inclined to develop small bubbles than others. This relates to the change in air solubility over the temperature range of intended use.

Based on this analysis it will be Tetrad's approach to build an initial probe enclosure with a cylindrical shape containing a simple phased array. We will do either real-time, or synthetic aperture imaging with this array to measure the signal drop off and to examine the reverberation level. If this approach can be made to work well enough with commercially available materials, it will be adopted as the approach of choice. If there is any question on performance level, Tetrad will discuss the performance the necessity for the development of the compound curvature enclosure with Goeff Lockwood. The development of the compound enclosure could become substantially more expensive than assumed in the original budgeting and may need to be assessed relative to other desirable features.

PROBE LIFE TIME

Most of the components of the mechanical system and the array have been tested in existing systems and found to be reliable. The motor, for example, should be capable of very high cycle counts. There are two exceptions to this. The first is that existing mechanical probes do not have 64 elements that must be brought out of the array through a moving interface. The highest element counts in current mechanical systems come from annular arrays that have 10 or less elements. It is possible with this low number of elements to use coax cables for the connections. With the phased array it will be necessary to go to a flex circuit interconnection. The wire connections on both ends of the flex can be well potted such that the only possible mechanism of failure would be in the flex leads themselves.

Flexes are often used in high cycle count equipment such as in laser printers. None the less, flex life is a parameter that should be tested early in the program to assure that there are no unexpected failures. To do this, we plan to have a traditional phased array built up and placed in a probe for life testing during the first six months of the program. This should establish that the life expectancy is sufficient or guide the redesign of a flex for the final delivery.

The second exception is that the phased array is not normally exposed to probe fluids. The phased arrays will be soaked in probe fluid early in the program to provide assurance that there is no degradation of materials or acoustic performance in the fluid environment.

PROVIDING HIGH TRANSMITTED ENERGY PER ELEMENT

The proposed synthetic aperture approach uses a reduced number of array elements to provide a diverging transmit beam. Analysis done by Goeff Lockwood indicated that the

signal to noise ratio could be maintained using the proposed approach if the transmit voltage could be increased by a factor of 5.

Since phased array elements may be pulsed with 200 volts or more the voltage required for the synthetic aperture approach would be 1000 volts or more if the output of the piezoelectric transducer were linear with respect to transmit voltage. However, the piezoelectric output does not increase linearly with applied E field, so it is possible that even more voltage might be required. Furthermore, the maximum E-field is high enough that it could cause depoling in the piezoelectric material if it were applied in a direction opposed to the direction of polarization. Consequently, the pulse must be unipolar. These constraints produce a significant design challenge for the transmitter.

Tetrad's initial proposal was to provide a piezoelectric array with 5 ceramic layers connected electrically in parallel and acoustically in series. This would allow the transmitter design to be similar to that of a standard phased array. Transmitting on 5 layers connected electrically in parallel with 1/5 the voltage that might be applied to a single layer material does not reduce the E field. This means that a unipolar pulse will still be required and the reduction in acoustic output due to nonlinearity will still be seen with the multilayer device.

Fig. 4 shows the relationship between E field and strain for a material similar to that which would be used for the array. The upper branch can be used to approximate the strain that will be achieved for various voltage levels. Given the stack dimensions at 3.5 MHz, the E field for 200 V and a single layer is about 4.4 KV/cm. This produces a strain of about 0.042%. If 600 V is applied to a single layer (or 200 V to a triple layer) the field is 13.2 KV/cm. This results in a strain of 0.102% or an increase of 2.4 times in strain for an increase of 3 times in E field. If 1000 V is applied to a single layer (or 200 V to five parallel layers) the field is 21.9 KV/cm and the strain is 0.138%. This is an increase of a factor of 3.3 in strain for an increase of 5 in E field. It also appears unlikely that any E field will yield an increase of a factor of 5 in strain.

This is a cause of some concern for an approach requiring five times the acoustic output whether it be attempted by application of a high voltage or use of five layers. Furthermore, one probable multilayer ceramic vendor objected to the use of five layers, saying that three layers was probably the most that could be reliably and repeatably made.

The KLM transducer model was run to evaluate the possibility of using three instead of five layers in the array. The results were rather encouraging. The model predicts that the signal to noise ratio in a three layer array is 16 dB better than that for a single layer array. When the strain nonlinearity is taken into account the improvement is 14 dB, which is exactly the factor of 5 required by the analysis done by Goeff Lockwood. Much of this improvement takes place on receive since the layered elements are much better at driving the cable than are the small single layer elements. Figs. 5 and 6 are the input/results pages from the KLM model for the single layer and triple layer array elements respectively.

There is still some risk in using even the 3-layer system since 3-layered ceramic is still not commonly available in the United States. The primary risk is that the material will not tolerate dicing without damaging at least a few elements. To reduce that risk Tetrad plans to purchase stacked ceramic from multiple sources and evaluate the dicability of the materials within the first eight months of the program. If good results can be established, work with the multilayers will proceed. If the results are not good, then Tetrad and Cleveland Clinic will reassess the requirements and attempt to determine a combination of electronics and arrays that will meet the signal to noise requirements. The requirements may again require careful financial analysis to avoid development that goes beyond the funding available.

At the time of this report Tetrad has received the first set of three layer ceramic, has diced 18 elements without apparent damage. The performance appears to be good.

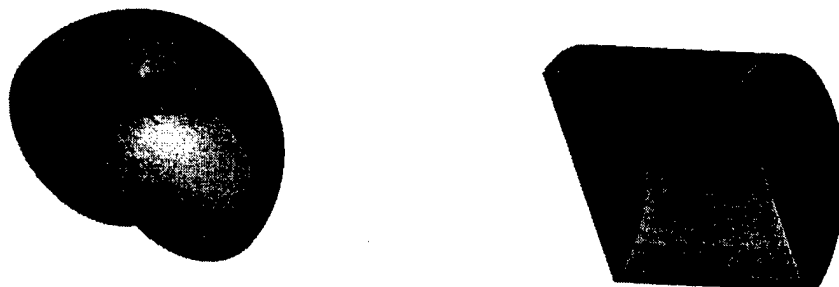
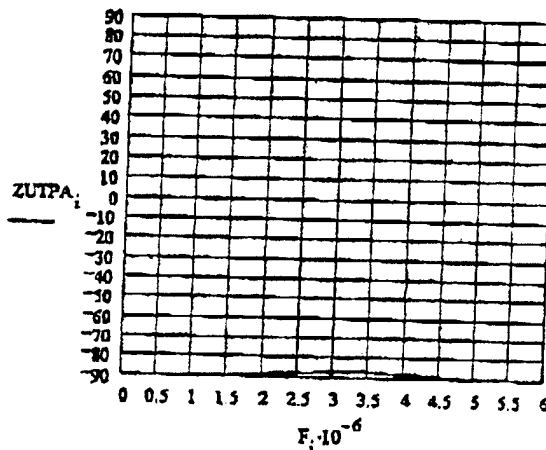
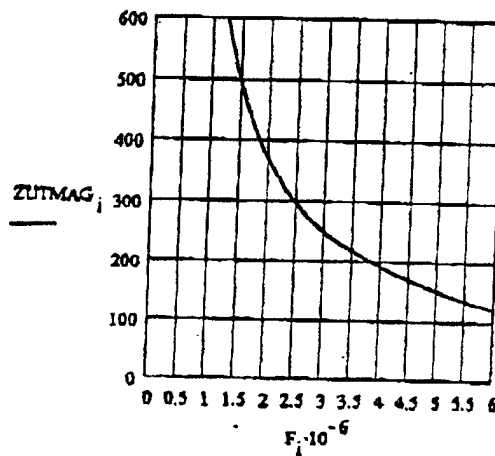
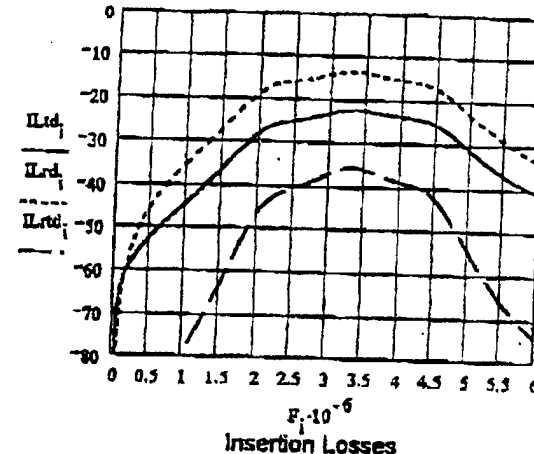
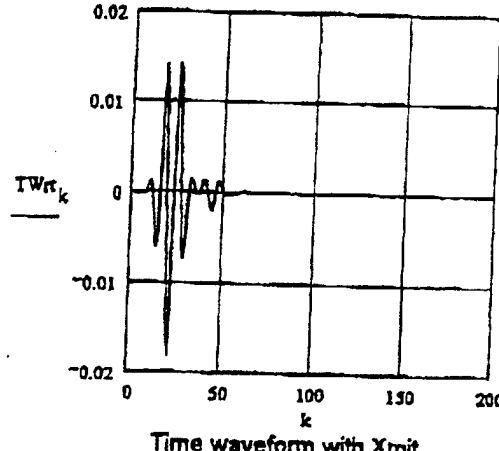


Fig. 1: Cylindrical window at left. Mechanical pivot is on the cylindrical axis. Toroidal section membrane at right. Mechanical pivot is at the center of the toroid. Phased array pivot (array center) moves on the circle that describes the center of the toroidal tube.

$U_f \cdot 10^{-6} = 3.026$ Center Frequency (MHz) $V_{recpp,2} = 0.032$ Received peak to peak voltage
 $BW\% = 57.633$ Band width (%) $V_{loss,2} = -35.833$ V_{ppin} over V_{ppout} expressed in dB
 $SNR_t = 83.467$ SNR for 2 Vpp SW Xmit $SNR_t = 95.978$ Signal to noise for 100,000 Pa transmit
 $IL_{td,i} := 10 \cdot \log(IL_{t,i})$ $IL_{rd,i} := 10 \cdot \log(IL_{r,i})$ $IL_{xtd,i} := 10 \cdot \log(IL_{t,i} \cdot IL_{r,i})$ $ZUT_{64} = 13.534 - 245.933i$



CERAMIC PARAMETERS $x=1$

$ZC = 4.78 \cdot x$ Impedance (MRays/s)
 $QC = 35$ Mechanical Q
 $6S = 1100$ Clamped relative permittivity
 $\tan\delta = 0.02$ Dielectric loss tangent
 $VC = 4.0 \cdot x$ Stiffened velocity (mm/usec)
 $KT = 0.7$ Thickness coupling
 $AC = .003$ Area in cm^2
 $TC = .45$ Thickness in mm

FILTER CHARACTERISTICS

LAYER 1 (CER SIDE) LAYER 2

$ZQW1 = 9 \cdot y$ $ZQW2 = 2.98 \cdot z$
 $VQW1 = 3.1 \cdot y$ $VQW2 = 2.6 \cdot z$
 $QQW1 = 28.7$ $QQW2 = 21.5$
 $TQW1 = .2$ $TQW2 = .18$

CABLE

$ZCAB = 50$ Z_0 (ohms) $L_s = 0$ μ Henries - None = 0
 $CCAB = 100$ Cap (pf/m) $R_s = 0$ Ohms - None = 0
 $RCAB = 1$ Res (ohm/m) PAR L (At Recv.)
 $GCAB = 0$ Cond (S/m) $L_p = 10^9$ μ Henries - None = 10^{19}
 $LEN CAB = 2$ Length (m) $R_p = 10^9$ Ohms - None = 10^{19}

FREQUENCY DATA

Run = 98713.01

$F_{start} = 0$ Start Frequency (MHz) (Usually 0)
 $F_{stop} = 6$ Stop Frequency (MHz)
FRONT LOAD
 $ZF = 1.48$ Impedance (MRays/s)
BACK LOAD
 $ZB = 3.0$ Impedance (MRays/s)
ELECTRICAL LOAD
 $R_{source} = 10$ Ohms
 $R_{load} = 100$ Ohms
 $F_1 = 20$ MHz
 $F_2 = 3$

$y = .2$ $z = .9$

Z Impedance (MRays/s)
 V Velocity (mm/usec)
 Q Mechanical Q
 T Thickness (mm)

AMPLIFIER NOISE
 $eq = 1.2 \text{ nV/Hz}^{1/2}$
 $in = 1.2 \text{ pA/Hz}^{1/2}$

$$CF \cdot 10^{-6} = 3.027$$

$$BW\% = 60.738$$

$$SNR_{rt} = 99.79$$

Center Frequency (MHz) $V_{recpp2} = 0.251$

Band width (%)

$$V_{loss2} = -17.786$$

SNR for 2 Vpp SW Xmit $SNR_r = 102.805$

$$IL_{rd_i} := 10 \cdot \log(\Pi_{L_i})$$

$$IL_{rd_i} := 10 \cdot \log(\Pi_{R_i})$$

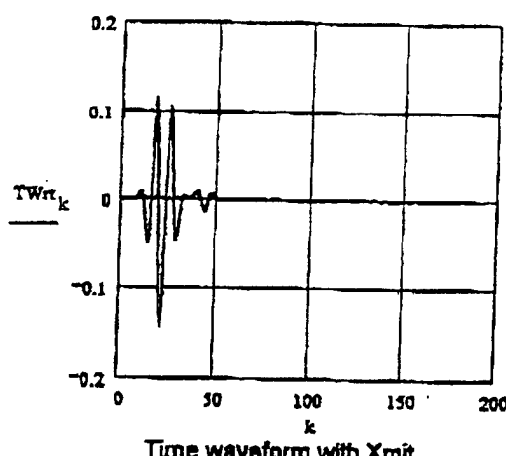
$$IL_{rd_i} := 10 \cdot \log(\Pi_{L_i} \cdot \Pi_{R_i})$$

$$ZUT_{64} = 63.259 - 167.235i$$

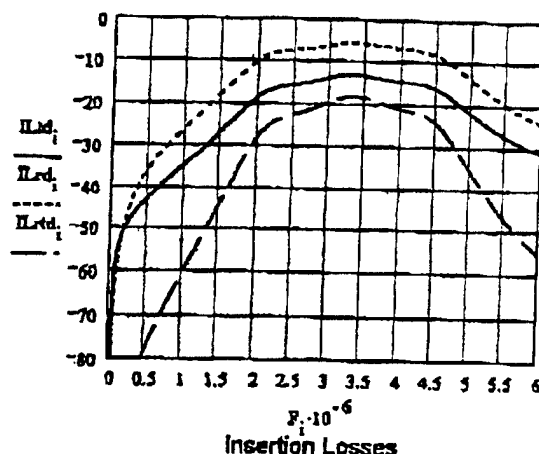
Received peak to peak voltage

Vpp in over Vppout expressed in dB

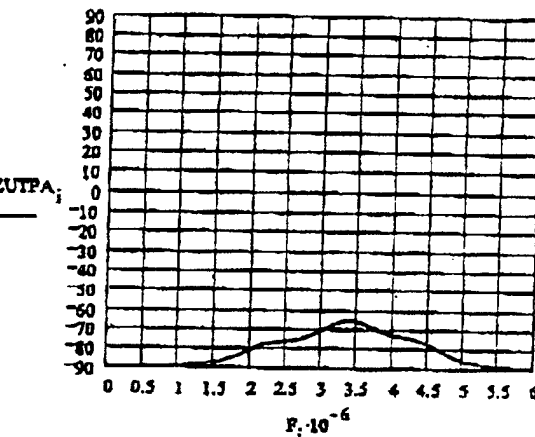
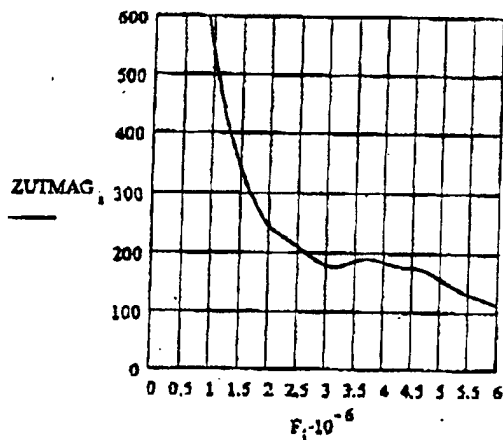
Signal to noise for 100,000 Pa transmit



Time waveform with Xmit



Insertion Losses

CERAMIC PARAMTERS $x=1$

$$ZC = 4.78 \cdot x$$

$$QC = 79$$

$$aS = 1100 \cdot 9$$

$$tmb = .02$$

$$VC = 4.0 \cdot x$$

$$KT = .7$$

$$AC = .003$$

$$TC = .45$$

$$FILTER CHARACTERISTICS$$

Impedance (MRayls)

Mechanical Q

Clamped relative permittivity

Dielectric loss tangent

Stiffened velocity (mm/usec)

Thickness coupling

Area in cm^2

Thickness in mm

Fstart = 0 Start Frequency (MHz) (Usually 0)

Fstop = 6 Stop Frequency (MHz)

FRONT LOAD

ZF = 1.44 Impedance (MRayls)

BACK LOAD

ZB = 3.0 Impedance (MRayls)

ELECTRICAL LOAD

Rsource = 10 Ohms

Rload = 100 Ohms

F1 = 20 MHz

Fh = 5 MHz

y = .8

z = .9

SERIES L (At Recv.)

Ls = 0 μ Henries - None = 0

Rs = 0 Ohms - None = 0

PAR L (At Recv.)

Lp = 10^9 μ Henries - None = 10^9 Rp = 10^9 Ohms - None = 10^9

Run = 90611.01

LAYER 1 (CER SIDE) LAYER 2

ZQW1 = 9.7 ZQW2 = 2.98

VQW1 = 3.1.7 VQW2 = 2.6.2

QQW1 = 20.7 QQW2 = 21.3

TQW1 = .2 TQW2 = .18

LAYER 3

ZQW3 = 1.54

VQW3 = 1.063

QQW3 = 30

TQW3 = .0

SERIES L (At Recv.)

Ls = 0 μ Henries - None = 0

Rs = 0 Ohms - None = 0

PAR L (At Recv.)

Lp = 10^9 μ Henries - None = 10^9 Rp = 10^9 Ohms - None = 10^9

CABLE

ZCAB = 54

CCAB = 28

RCAB = 1

GCAB = 0

LEN CAB = 2

Zo (ohms)

Cap (pF/m)

Res (ohm/m)

Cond (S/m)

Length (m)

Ls = 0 μ Henries - None = 0

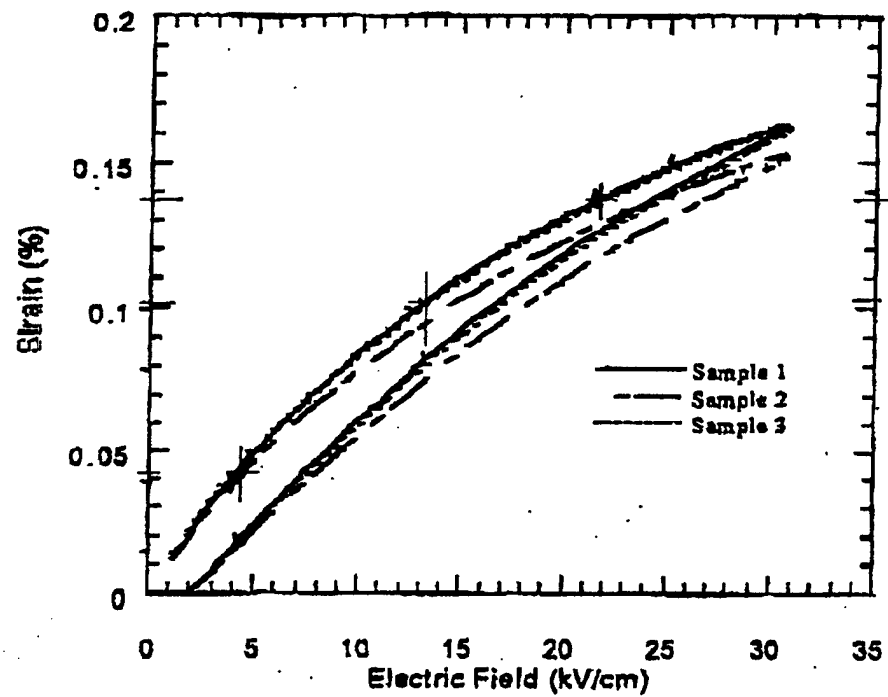
Rs = 0 Ohms - None = 0

PAR L (At Recv.)

Lp = 10^9 μ Henries - None = 10^9 Rp = 10^9 Ohms - None = 10^9

AMPLIFIER NOISE

en = 1.2 nV/Hz^{1.5}in = 1.2 pA/Hz^{1.5}



Courtesy of:
TRS Gravels

FIGURE 1

Project: Cleveland Clinic 3-D – Mechanically Steered Phased Array Probe
Subcontract #: _____
Report: 1999 Q4 Summary
Date: December 28, 1999
Written by: Clyde Oakley
Organization: Tetrad Corporation
Address: 357 Inverness Drive South
Suite A
Englewood, CO 80112
Phone: 303-754-2315
FAX: 303-754-2329
Email: coakley@tetracorp.com

The main efforts of the program during this quarter had to do with subcontracting the mechanical mechanism and continuing to investigate multilayer phased arrays.

Regarding the mechanism; the specifications were completed and the subcontract signed in early November. A single layer phased array with suitable performance for testing the probe acoustics has been developed for testing the acoustic performance of the mechanical scanner dome and fluid system. The flex circuit for attaching the array has been designed fabricated. Acoustic testing of membrane materials and fluids has been completed for materials that should be compatible the use of a phased array with a cylindrical dome. Initial prototypes for in-situ acoustic testing are being constructed.

A mechanism and motor driver has been configured for achieving 20 frames per second and life testing is in progress.

Work with the multilayer phased array is slightly behind the original schedule. The single layer phased array that was constructed as a baseline showed approximately 7 dB less sensitivity than comparable commercial units. The cause of this sensitivity loss has been identified and single units with sensitivity comparable to other commercial units can now be made consistently. Alternate lensing studies are underway to improve the sensitivity more.

One unit has been constructed using multilayer ceramic. The geometry for the multilayer is not exactly the same as it was for the single layer units but the increase in sensitivity on the best elements is on the order of 12 dB more sensitive on the multilayer units. Unfortunately some elements showed signs of losing internal electrodes. A second unit is being built using more care in selecting, handling, and dicing the multilayer units. Some units also showed signs of depoling. This appears to have been corrected after they were returned to the vendor to undergo a revised poling process.

It is our goal to reach a decision on the use of multilayers by the end of January, 2000.

Effects of Motion on a Synthetic Aperture Beamformer for Real-time 3D Ultrasound

C. R. Hazard ^{1,2} and G. R. Lockwood ^{1,3}

¹ Department of Biomedical Engineering, The Cleveland Clinic Foundation, Cleveland, OH.

² Biomedical Engineering Program, The Ohio State University, Columbus, OH.

³ Department of Physics, Queen's University, Kingston, Ontario, Canada.

Abstract--A synthetic aperture (SA) beamformer is theoretically capable of collecting volume data sets in real-time. Since SA imaging requires phase coherence over multiple transmit events, relative motion between the transducer and target is a concern, especially for a cardiac imaging system. The sensitivity to motion of a sparse transmit SA beamformer was evaluated by simulating a sector scan of a moving point target. The results were quantified by plotting the maximum value of the beamformed signal as function of scan angle. Simulations were used to examine motion in both the axial and lateral directions. Lateral motion, for the speeds simulated (≤ 2 m/s), did not significantly change the secondary lobes in the radiation patterns. Motion in the axial direction produced more distortion of the radiation pattern; however, the secondary lobes for targets moving at speeds representative of cardiac motion (< 80 mm/s) were not significantly different than those for stationary targets. For larger speeds (400-800 mm/s) the secondary lobes rose about 4 dB. These findings were verified experimentally using a 2.6 MHz array. The results indicate that SA beamforming with a sparse transmit array may be feasible for cardiac imaging.

I. INTRODUCTION

Real-time 3-D ultrasound imaging provides unique clinical information. We have previously described a method for real-time 3-D imaging using a sparse linear phased array and synthetic aperture (SA) beamforming [1], [2]. A real-time 3D data set is collected by mechanically rocking the array in the elevation direction while rapidly acquiring 2D images. Figure 1 depicts the collection sequence for a SA image. A single diverging pulse is transmitted and the

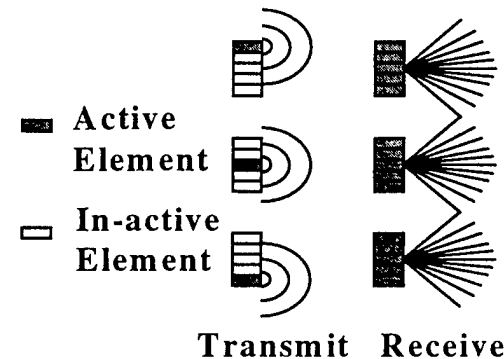


Figure 1: Collection sequence for synthetic aperture system

echoes are simultaneously collected on all receive channels. The signal for each channel is digitized and stored. This procedure is repeated for each transmit events. The stored signals are then delayed, apodized, and summed digitally to form all of the lines in the image simultaneously. Provided the transducer and target tissue are stationary during data collection, the phase coherence necessary for proper beamforming is maintained. However, if the target or transducer moves during image acquisition, the radiation pattern will be degraded. Cardiac imaging is one application in which target motion is present. The velocity of the heart wall has been reported to be between 50 mm/s and 80 mm/s in systole and lower in diastole [3]. Since the transducer is continuously rocked during the collection of a 3D data set, transducer motion is also a concern.

The problem of motion in SA imaging systems has been investigated previously, and several researchers have proposed algorithms to restore phase coherence in the presence of tissue motion [4],[5]. In this paper, we investigate how much motion can be tolerated by a sparse transmit SA imaging system

before the loss of phase coherence significantly deteriorates the radiation pattern. The motion sensitivity was investigated by simulating a sector scan of a moving point target. This computer simulation was validated using an experimental rf data set.

II. EXPERIMENTAL DATA COLLECTION

A 96 element transducer array (General Electric, model 227S), with a center frequency of 2.6 MHz and 0.28 mm element spacing, was used to collect the experimental rf data sets. 64 elements of the array were used. The array was positioned at the top of a water tank using a precision translation stage which allowed for precise up and down movement. The target was a small sealed plastic cylinder, positioned 7 cm ($\sim f/4.3$) from the face of the array with the long axis perpendicular to the image plane.

Data collection followed the sequence shown in figure 1. A single element was excited (± 40 V) and the echoes were recorded on each of the 64 elements individually. (In a real-time system the signals would be recorded simultaneously.) This procedure was repeated for each of three transmit events. The signals received by the array elements were amplified by a low noise pre-amplifier (Miteq) and digitized at 50 MHz and 8 bits by a digital oscilloscope (H.P. 54522A). An averaging feature of oscilloscope was used to increase the number of effective bits to 10. The digital data was transmitted to a PC, where the dc component was removed before beamforming.

To simulate the effect of motion, the target was moved a specified distance between transmit events. This distance was calculated by multiplying the velocity to be simulated by the time between transmits (200 μ s). Experimental rf data sets were collected for a stationary target and targets with axial speeds of 400 mm/s and 800 mm/s.

Collecting an experimental rf data set for synthetic aperture is very tedious. To facilitate exploring of a wider range of parameters, a computer was used to generate simulated rf data sets. While this simulation does not completely model the experimental environment, it provides useful information for predicting the performance of the system. The experimental data was used to validate the results of the computer simulations.

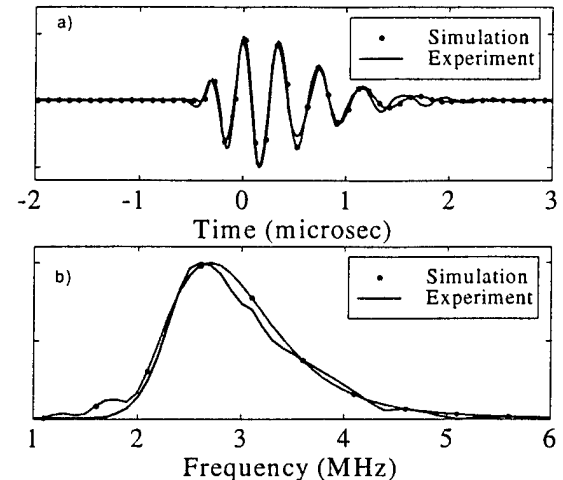


Figure 2: Simulated and Experimental pulse. a) pulse b) spectrum.

III. COMPUTER SIMULATIONS AND BEAMFORMING

We simulated an array with 64 elements spaced at 0.28 mm, and the center frequency of the simulated rf pulses was 2.6 MHz. The shape of the pulse used in the computer simulations was matched to the experimental pulse so that the resulting radiation patterns could be compared. Figure 2 compares the simulated pulse with an experimental pulse, both in the time and frequency domains. The same sparse transmit aperture used in the experiment was simulated. The signals for a point target placed at $f/4.3$ and -2.2° were calculated for each of the active transmitter-receiver pairs and sampled at 50 MHz and 10 bits. These signals were stored and used as an input to the same beamforming program that was used for the experimental data.

The beamforming program generates a sector scan from -45° to 45° . Each point in the sector scan was generated by summing appropriately delayed signals from each channel for each transmit. The delayed signal values were calculated by linearly interpolating between the two surrounding digitized data points [1]. A raised cosine apodization was used on receive and the outer transmits were given one half the weight of the central transmit. Second order sampling was used to approximate the envelope of the beamformed signals. A radiation pattern was generated by plotting the maximum value of the demodulated signal along each scan line as a function of the scan angle.

IV. RESULTS

A. Lateral Motion

A rocking array, for real-time 3D imaging at 20 volumes per second, will produce lateral velocities of about 1.6 m/s at the depth of 15 cm. Figure 3 shows the effect lateral motion on the main lobe of the radiation pattern for velocities of 0, 1 m/s, and 2 m/s. The main lobe is shifted and slightly wider in the presence of lateral motion. The secondary lobes remain unchanged in the presence of the lateral motion.

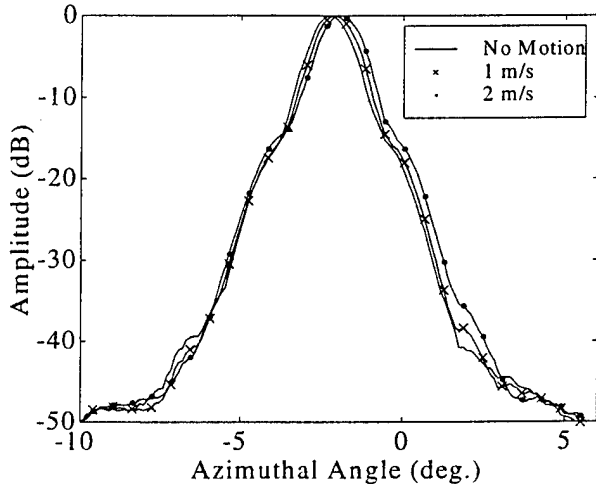


Figure 3: Effects of simulated lateral motion on the radiation pattern.

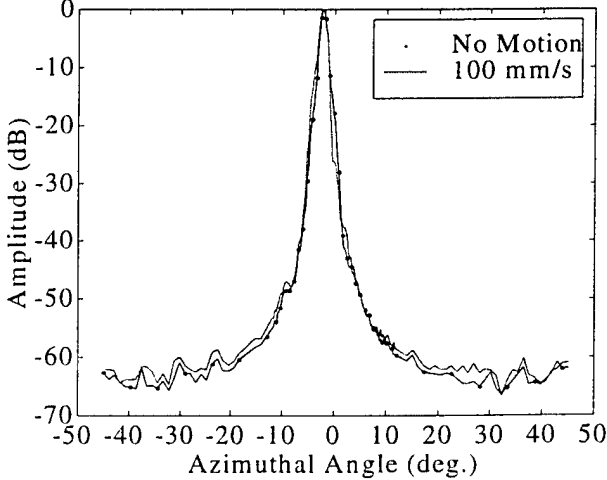


Figure 4: Comparison of the radiation patterns for axial velocity of 0 mm/s and 100 mm/s.

B. Axial Motion

Axial motion causes a more serious disruption of the phase coherence required for beamforming. This can result in a deterioration of the resolution and

contrast in a SA image. Simulations of the radiation pattern for a point target moving with an axial velocity of 0 mm/s and 100 mm/s (representative of cardiac motion) are shown in figure 4. The results show no significant difference in the level of the secondary lobes only a slight distortion of the main beam.

Figure 5 compares the theoretical and experimental radiation patterns for stationary targets and target velocities of 400 mm/s and 800 mm/s. There is good agreement between the theory and experiment down to about -50 dB. The secondary lobes are below -54 dB for all cases. The unique structures in the main lobe, caused by the axial motion, are seen in both the theory and experiment, though not quite as pronounced in the experiment. The secondary lobes for the theory are about 6 dB lower than the experimental data. Since the experimental data was collected over a long period of time, mechanical vibrations and thermal fluctuations may have contributed to this difference. Axial motion causes a shift in the location of the peak and slight widening of the main beam, in addition to the changes in the fine structure of the main beam. The level of the secondary lobes for a stationary target is about -64 dB for the simulation and -58 dB for the experiment. The secondary lobes for cases with axial motion of 400 mm/s and 800 mm/s are about 4 dB higher than those for the stationary target. However, the level of the secondary lobes for an axial target velocity of 400 mm/s is not significantly different from level for an axial velocity of 800 mm/s. This is true for both theory and experiment. The level of the secondary lobes in the presence of axial motion is -60 dB for theory and -54 dB for experiment.

V. SUMMARY AND CONCLUSIONS

In this paper, we have presented experimental and simulated evidence that motion can be tolerated in a sparse transmit synthetic aperture imaging system. In both experiment and simulation a 2.6 MHz, 64 element array with signals digitized at 10 bits and 50 MHz was evaluated with a point source at f/4.3. Linear interpolation was used to increase the delay accuracy in beamforming.

The results of the simulations show that lateral motion does not significantly distort the radiation pattern for the velocities simulated (≤ 2 m/s). There is no rise in the level of the secondary lobes

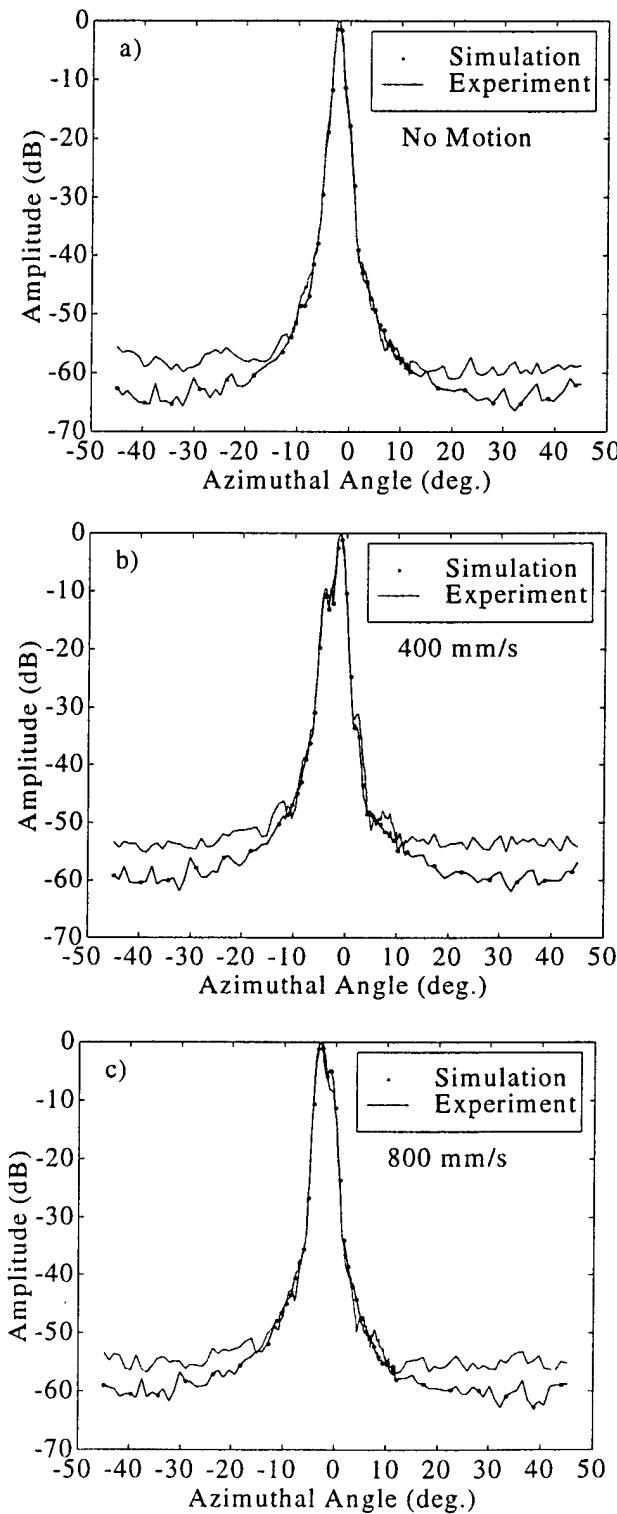


Figure 5: Effects of axial motion on the radiation pattern. Theory and experiment for a) no motion b) 400 mm/s and c) 800 mm/s.

and only a minor shift and widening of the main beam.

While axial motion is a more serious concern, simulations reveal that at speeds typical of cardiac motion (80 mm/s) there is little distortion of the main beam and virtually no increase in the level of the secondary lobes. At higher speeds (400 mm/s-800 mm/s), there is about a 4 dB increase in the level of the secondary lobes. Axial motion also produces fine structure in the main lobe and widens the beam slightly. These results were seen in both experimental data and simulation. The results suggest that real-time 3D imaging using a synthetic aperture beamformer is feasible for cardiac imaging.

VI. REFERENCES

- [1] C. R. Hazard and G. R. Lockwood, "Theoretical assessment of a synthetic aperture beamformer for real-time 3D imaging," *IEEE Trans. Ultrason., Ferroelect., Freq. Contr.*, vol. 46(4), pp. 972-980, 1999.
- [2] G. R. Lockwood, J. R. Talman, and S. S. Brunke, "Real-time 3-D ultrasound imaging using sparse synthetic aperture beamforming," *IEEE Trans. Ultrason., Ferroelect., Freq. Contr.*, vol. 45, pp. 980-988, 1998.
- [3] H. Yamada, T. Oki, T. Tabata, A. Iuchi, S. Ito, "Assessment of left ventricular systolic wall motion velocity with pulsed tissue Doppler imaging: comparison with peak dP/dt of the left ventricular pressure curve," *Journal of the American Society of Echocardiography*, vol. 11(5), pp. 442-9, 1998.
- [4] G. E. Trahey, L. F. Nock, "Synthetic receive aperture imaging with phase correction for motion and for tissue inhomogeneities--Part II: Effects of and correction for motion," *IEEE Trans. Ultrason., Ferroelect., Freq. Contr.*, vol. 39(4), pp. 496-501, 1992.
- [5] H.S. Bilge, M. Karaman, M. O'Donnell, "Motion estimation using common spatial frequencies in synthetic aperture imaging," Proc. IEEE Ultrason. Symp., pp. 1551-1554, 1996.

This work was supported by the U.S. Army Telemedicine and Advanced Technology Research Center.

Mutual information based registration of cardiac ultrasound volumes

Vladimir Zagrodsky, Raj Shekhar, J. Fredrick Cornhill

The Cleveland Clinic Foundation
Cleveland, Ohio 44195 USA

ABSTRACT

Real-time volume ultrasound imaging of the heart is a new trend, and the registration of acquired volume framesets is clinically important. This registration may be accomplished by processing a selected pair of volume frames having identical cardiac phase (preferably end diastolic) from two framesets. The registration solves for the optimal rigid transformation between selected volumes through maximization of mutual information, a voxel similarity measure. The accuracy of registration was estimated through retrieval of an artificially introduced misalignment. Two volume frames, belonging to the same frameset and separated in time by 250 ms, were selected. The secondary volume was translated by seven voxels along each axis and rotated by seven degrees about each axis relative to the primary prior to registration. The translational mismatch upon registration was within one voxel and the rotational mismatch less than two degrees. Reduction of the speckle noise by spatio-temporal averaging followed by intensity binning was a key step in successful application of mutual information approach to ultrasound imaging. The application of our method to nine framesets arising from four different patients demonstrates the feasibility of using of mutual information for automatic registration of cardiac ultrasound data.

Keywords: 3D Registration, 3D Ultrasound, Mutual Information.

1. INTRODUCTION

Real time three dimensional (3D) acquisition is one of the latest developments in the field of ultrasound imaging. The traditional ultrasound transducers produce planar images, typically at 20-30 frames per second. Before the advent of real time 3D ultrasound imaging, attempts were made to create 3D images through stacking of planar images by carefully sweeping a traditional ultrasound transducer over a 3D region¹. This approach was however prone to patient movement and transducer localization errors, and more importantly is not fast enough to image a moving anatomy such as the heart in three dimensions. In contrast, real time 3D ultrasound acquisition is capable of producing approximately 20-30 volumes per second and truly capturing the motion of the heart with a very high temporal resolution. In essence, real-time 3D ultrasound imaging is four dimensional (4D) imaging with time being the fourth dimension.

Real time 3D ultrasound enables many new applications; one of which is registration of 4D images or volume framesets. Registration of two ultrasound volume framesets taken before and after a clinically significant event can provide important diagnostic information. In this paper we present our ongoing work on the registration of cardiac volume framesets. The eventual goal of the present work is to visualize the deviations in cardiac size and shape between two ultrasound examinations. The registration is therefore limited to rigid geometric transformation described by six parameters – three associated with translation and three with rotation. An additional registration parameter is the volume frame number that depends on the accompanying electrocardiogram (ECG) and is described in detail in the next section.

There are two main approaches to image registration: segmentation based and voxel similarity based^{2,3}. Segmentation based image registration seeks to first identify matching structures in the two datasets and then fit the identified matching structures using a fitting criterion. Segmentation of real time 3D ultrasound images is a complex problem in its own right and the degree of true correspondence between the matching structures is always of suspect. This approach was therefore considered unsuitable for the present registration application. The second approach to image registration exploits the underlying data (pixel or voxel) similarity and does not depend on prior segmentation. This approach is also amenable to both intra- and inter-modality image registration with full automation. A data similarity approach was deemed most fitting for the problem at hand.

Correspondence: Raj Shekhar (Email: shekhar@bme.ri.ccf.org, Phone: 216-445-3246)

Among many data similarity measures, mutual information (MI) has been demonstrated to be most effective and robust for multi-modality registration of a structural imaging modality (MRI and CT) with a functional imaging modality (PET, SPECT, etc.)⁴⁻⁵. Our choice of mutual information as the measure of data similarity was based on its reported success. We do note that we have found only one example of the use of mutual information in ultrasound image registration⁶ so far. In general, image registration involving ultrasound data has not been investigated actively. The present study is therefore an investigation into a) the feasibility of using mutual information for ultrasound image registration and b) identification of a procedure to compute mutual information for most effective results.

2. REGISTRATION APPROACH

Before describing our technique, a word on terminology is essential due to the new imaging modality involved. We will refer real time 3D ultrasound imaging simply as 3D ultrasound imaging in the remainder of the paper. 3D ultrasound image acquisition produces a sequence of volume frames which will be called a frameset. A frameset will be considered synonymous with a 4D image. A volume frame within a frameset will be referred to as a frame.

Our objective has been to register a pair of cardiac ultrasound framesets or in other words perform 4D registration. We assume that a single 3D rigid transformation differentiates the two framesets. This is a safe and reasonable assumption given the short image acquisition duration to allow any fluctuation in the transducer orientation and breathing-related movement artifacts. Owing to rapid acquisition rate (20-30 frames per second) of 3D ultrasound imaging, a typical examination lasts less than two seconds giving forth more than one full cardiac cycle of data. The 4D registration problem can therefore be seen as consisting of two distinct parts: temporal registration and 3D spatial registration.

Temporal registration - Temporal registration is the process of establishing frame-by-frame correspondence based on cardiac phase between two given framesets. This step would not have been required if the acquisitions were ECG triggered. In the present study however, temporal registration ensured that a frame showing for example the onset of diastole in the first frameset corresponded with a frame with the same phase in the second sequence. When the frame rate is identical between the two framesets, a one-point synchronization suffices frame-by-frame matching for all the remaining frames. If the frame rate is different, data interpolation may be required along the time axis. The frame rate was kept constant in the present study eliminating any need for data interpolation for temporal registration.

3D spatial registration - 3D spatial registration is the search for the optimal 3D rigid transformation between a pair of "temporally registered" frames, called the primary and the secondary. This rigid transformation when applied to the secondary puts it in the reference frame of the primary. As explained above, we assume that this same 3D rigid transformation describes the misalignment between each pair of frames.

Any cardiac phase can be chosen to perform temporal registration and the subsequent 3D spatial registration. Theoretically, the frame rate of 3D ultrasound imaging is high enough to capture short-lived cardiac events such the onset of systole, and all phases should yield the same result. Practically, the choice of end diastolic phase wherein the heart is typically stationary in human for 200-250 ms is the most prudent selection. A small time shift error in temporal registration will have little influence on the accuracy of 3D spatial registration. Furthermore, since the temporal resolution of 3D ultrasound imaging is not infinite, the end diastolic images are expected to have the least motion artifact. The desired central end diastolic frame can be determined by analyzing ECG that accompanies routine cardiac echocardiographic examinations. We also present an alternate approach to determining the most stationary end diastolic phase by computing mutual information between adjacent frames. The more stationary the heart, the greater is the correlation, and hence, the higher is the mutual information between two adjacent frames. The frame with the highest "adjacent frame" mutual information along the sequence corresponds well with the central end diastolic phase given by ECG.

The mutual information $I(A, B)$ between two volume frames A and B depends on individual probability density functions $p(a)$ and $p(b)$, and the joint probability density function $p(a, b)$ of voxel intensities in the overlapping zone of A and B . Mathematically,

$$I(A, B) = \sum_a \sum_b p(a, b) \log \left(\frac{p(a, b)}{p(a)p(b)} \right) \quad (1)$$

Both a and b vary in the interval $[0, M]$ where M is highest possible voxel intensity value. The intensity distributions are accumulated as below:

$$p(a) = \frac{n(a)}{N}, \quad p(b) = \frac{n(b)}{N} \quad \text{and} \quad p(a, b) = \frac{n(a, b)}{N} \quad (2)$$

where $n(a)$ and $n(b)$ are number of A and B voxels with intensity a and b respectively in the overlapping zone, and $n(a, b)$ is a similar quantity for the joint distribution. N is the total number of voxels in the overlapping zone.

The general approach of 3D spatial registration is the following. The primary frame of the selected pair is kept fixed spatially whereas the secondary is subjected to a series of rigid transformations. Each successive transformation brings the secondary progressively in alignment with the primary according to a criterion function, i.e., mutual information in the present study. The process is said to have converged when mutual information is maximized and any further transformation yields a smaller mutual information value. A rigid transformation in 3D is described by a matrix of six independent parameters - three controlling translation and three rotation. During successive iterations, original voxels of the secondary do not generally coincide with those of the primary. The calculation of the criterion function is preceded by interpolation (trilinear interpolation in the present study) of the transformed secondary.

The 3D spatial registration involves an iterative search for the optimal rigid transformation that maximizes MI in a six-dimensional parameter space. There are a few important issues to keep in mind when selecting the search algorithm. It has been shown that the hypersurface defined by the MI function is generally uneven with a lot of ripples⁵. Our findings confirm this. The search algorithm should therefore be robust to local maxima and converge only to the global maximum. A robust search algorithm however takes longer to converge to the solution and can become computationally prohibitive.

A few preliminary tests were carried out to pick the most suitable algorithm for the multi-parameter optimization. The numerical gradient based techniques were found to be sensitive to function unevenness and demonstrated unstable behavior. The simulated annealing algorithm was found robust but very slow. The Nelder-Mead direct search algorithm provided most accurate results for the MI function upon reasonable selection of initial step value and termination-continuation conditions. Briefly, the Nelder-Mead direct search algorithm⁷ constructs a pyramid in the six-dimensional parameter space from seven initial trial points. During optimization, vertices of the pyramid converge toward the solution while the pyramid shrinks in size. A new candidate vertex is the mirror image of the vertex with the smallest MI value, about the directly opposite face. A new pyramid is built depending on the relative values of MI at the candidate vertex and the other six vertexes. It is easy to appreciate that the optimization will not be caught in a local maximum with dimensions smaller than the pyramid size.

A characteristic feature of ultrasound images is the presence of speckle noise that is likely responsible for the unevenness in the mutual information function. Intra-frame spatial averaging, which also improved images visually, slightly reduces this effect. Furthermore, inter-frame temporal filtering was performed that was particularly effective because speckles are at least partially uncorrelated in adjacent frames. The dynamic nature of the heart dictates that only a few adjacent frames be averaged however. Intensity binning when creating histograms for computing mutual information was another method of speckle reduction. The net effect of binning was to discard lower voxel intensity bits. The intensity binning eliminated low-power speckles and their influence on MI.

The validation of our registration technique requires that the computed results be compared to a gold standard. The only gold standard that may exist for the present application is the result of manual registration by experts. For the purposes of this preliminary study and to get an estimate of the order of error, we performed a set of intra-frameset registration experiments. The orientation of an ultrasound transducer is virtually fixed during an examination due to short acquisition duration. Therefore it is appropriate to assume that the individual frames of a frameset are perfectly registered. We picked two neighboring frames that were perfectly aligned to begin with from the same frameset, and applied to one of them a known transformation thus creating a known misalignment. The normal 3D spatial registration procedure was applied to recover the misalignment. A quantitative analysis was possible by comparing the known transformation with the solution of 3D spatial registration.

3. DATA PROCESSING

3.1. Image Acquisition

Ultrasound images used in the study were acquired on a 2.5 MHz 3D ultrasound scanner manufactured by Volumetrics, Inc. The nine framesets used in the study were images of the left ventricle of four different patients. The scanner generates volume frames that are sector scans in 3D or roughly shaped like a pyramid truncated at the top (Figure 1). The size of the pyramid is user controlled through scan depth and scan angle parameters. The framesets used in the present study all had a scan depth of 16 cm and 60 degree of angular span in both B-mode directions. In addition, the images were collected at 20 frames per second and the number of frames in a set varied from 18 to 32.

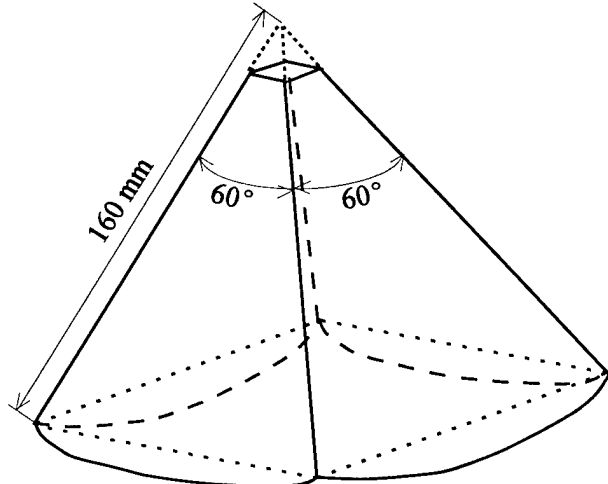


Figure 1. The truncated pyramid shape of 3D ultrasound volume frame.

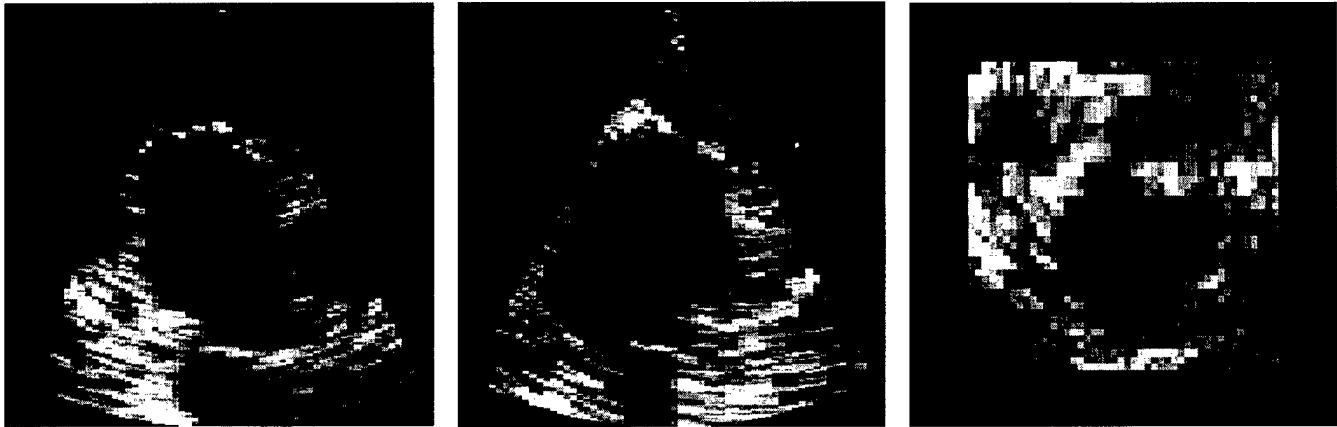


Figure 2. Three orthogonal views showing left ventricle of a scan converted 3D ultrasound frame.

3.2. Scan Conversion

The original polar data was scan converted to a rectilinear grid. The polar frames had a $64 \times 64 \times 512$ resolution with 512 samples along the radial direction. The scan converted frames were sized $128 \times 128 \times 512$ to maintain the native higher radial resolution. The scan conversion conceptually placed the smallest bounding box around the polar frame. Based on the value of acquisition parameters, the physical dimensions (in mm) of the bounding box were $167.2 \times 167.2 \times 160$. A byte described the ultrasound voxel intensity in both the native and scan converted data. Figure 2 shows an example of three orthogonal sections of a scan converted frame. The first two panels show two orthogonal long axis views of the left ventricle whereas the third panel shows a short axis view.

3.3. Subsampling and Speckle Reduction

The original $128 \times 128 \times 512$ sized frames were subsampled by a factor of two to keep computational needs of registration within reasonable limits. Uniform intra-frame averaging by a $2 \times 2 \times 2$ kernel helped achieve both subsampling and speckle reduction by spatial smoothing.

Temporal (inter-frame) filtering helped reduce speckles further. A weighted averaging over three adjacent frames was performed with a [$\frac{1}{4}, \frac{1}{2}, \frac{1}{4}$] kernel, i.e., each voxel was filtered with analogous voxels from the preceding and succeeding frames. The contribution of each neighboring voxel was half of that of the current voxel. Since the end diastolic frames were not end frames, the above-described temporal filtering was carried out without ambiguity. Registration was performed both with and without temporal filtering to understand its effects.

An implicit averaging and hence speckle reduction took place in the creation of histograms for MI calculation. By binning the intensities in the histogram, or equivalently, discarding a few lower bits of the voxel intensity, a further smoothing took place. The more intensity bits were rejected, the more smoothing took place. The effect of intensity binning on the outcome of registration was studied by repeating experiments six times by varying the number of intensity bits from all eight to upper three.

3.4. Data mask

While the rectilinear representation of data is suitable for image processing, a byproduct of scan conversion is inclusion of blank area outside the original pyramid into data representation. The black region of zero intensity around the image data in Figure 2 corresponds to the blank area. The blank area voxels must be rejected while computing probability density functions. To facilitate this, a bit mask was created that corresponded with the shape of the original image data. This mask was helpful in the determination of the overlapping zone of two frames. Although an analytical formulation for the region on overlap is possible, defining a mask was more convenient from implementation standpoint.

3.5. Inter-frame MI

As mentioned earlier, adjacent frame MI along a frameset was found a good indicator of cardiac phase. Inter-frame MI was also useful in appreciating the physical meaning of the mutual information as a measure of data similarity. To this end, MI was also computed between all possible pair of frames within a set.

3.6. Validation

Experiments were carried out to test the feasibility of MI based 3D spatial registration of cardiac ultrasound frames and to estimate its accuracy as a function of the number of bits used for computing MI and temporal inter-frame filtering. An intra-frameset approach was taken, as described earlier, where a known misalignment was created between perfectly pre-registered frames. The two frames selected were end diastolic frames separated by four frames or 250 ms. The initial misalignment was created by introducing a shift of seven units in each of the six transformation parameters. A seven unit shift in a translation parameter was equal to seven voxels or approximately 9 mm. A seven unit shift in a rotation parameter equaled seven degrees. The sign (positive or negative) of these shifts was chosen randomly. Simply reversing the signs of each transformation parameter created a second initial misalignment between a pair of frames. Overall, 3D spatial registration was performed on nine frame pairs originating from nine framesets and each frame pair was registered twice from two different starting misalignments. Furthermore, registration was launched six times for each starting misalignment to study the relationship of the accuracy of registration with the number of intensity bits used for computing MI.

If the registration worked perfectly, a pair of frames would have come back to the original alignment upon registration. In reality, the algorithm converged to a solution that did not fully annul the user-introduced misalignment. The difference in the expected and the actual solutions was our evaluation criterion. This difference was represented as a gross displacement and angle mismatch.

4. RESULTS

The adjacent frame MI versus the acquired ECG for two different frame sets is shown in the two panels of Figure 3. The midpoint of end diastole is typically about 200 ms left of the peak of R wave. The maximum of adjacent frame MI approximately coincided with end diastole. The low values along the MI curve depict phases where the movement of the heart between frames was more drastic. Another way to present the same concept is a surface plot of inter-frame MI between all pairs of frames in a frameset (see Figure 4). The frameset used for this illustration contained 32 frames. The tallest ridge corresponds to MI of a frame with

itself. The other peaks correspond to pair of frames with end diastolic phase. It should be noted that the frameset used to create the plot here spanned roughly two cardiac cycles and hence two end diastolic phase frames explaining the presence of multiple peaks.

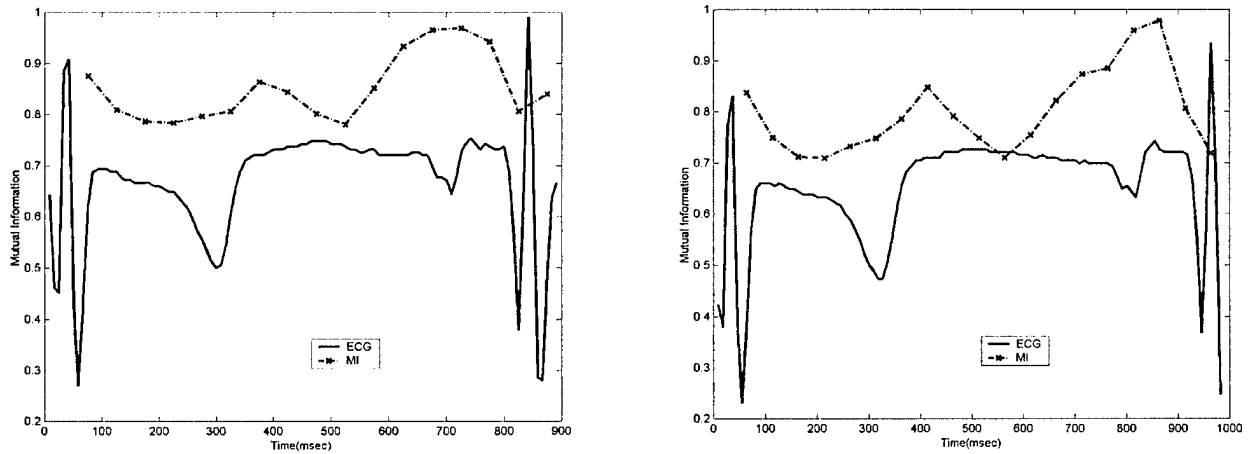


Figure 3. Two examples of "adjacent frame" mutual information versus ECG.

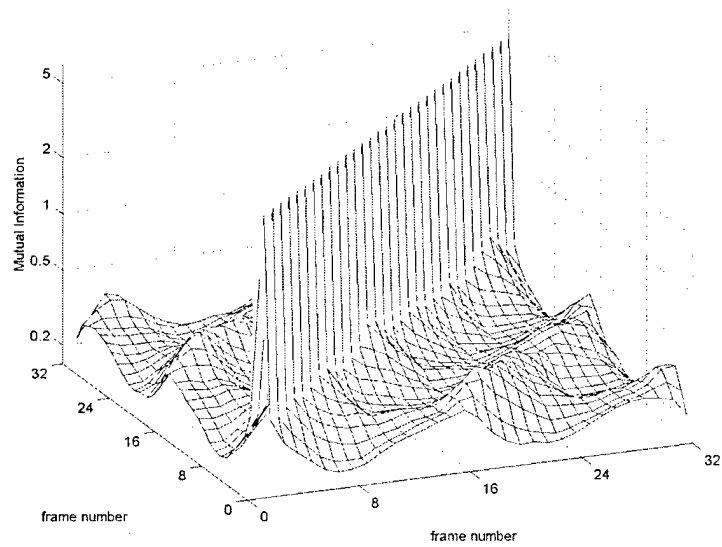


Figure 4. Mutual information between all pairs of 32 frames of a frameset: The diagonal ridge corresponds to MI of a frame with itself. Other peaks correspond to pair of frames with end diastolic phase.

Table 1 compiles the result of registration for three randomly selected pairs of frames. The displacement and angle mismatches from the expected solution is presented for six varying schemes of MI computation. The optimal number of intensity bits to use for MI computation is not evident from the three cases presented. A more comprehensive trend emerges from the complete results enumerated below.

Table 1. The accuracy of registration for three pairs of frames for six different schemes of computing MI.

Frameset ID and frame serial numbers	Number of intensity bits					
	8	7	6	5	4	3
[D12, frames 8 & 3]	1.27 mm. 1.16 deg	2.58 mm 2.51 deg	1.88 mm 1.59 deg	1.23 mm 0.17 deg	1.31 mm 0.46 deg	1.22 mm 0.33 deg
[D802, frames 17 & 12]	0.36 mm 1.19 deg	0.48 mm 0.07 deg	0.32 mm 0.75 deg	0.57 mm 0.30 deg	1.99 mm 9.25 deg	0.91 mm 0.15 deg
[D0b, frames 15 & 10]	1.77 mm 11.17 deg	1.23 mm 1.02 deg	1.09 mm 1.06 deg	1.23 mm 1.00 deg	0.81 mm 0.09 deg	0.89 mm 0.38 deg

Results of registration for all 18 combinations of nine framesets and two initial misalignments are presented in Table 2. Each row has results specific to the number of intensity bits used for MI calculation. Both root-mean-square (RMS) and median displacement and angle values are reported. The median values are reflective of the most common case without the influence of outliers that the RMS values suffer from. The last column has the number of outliers, which were the cases for which the result was off of the expected solution by more than the cutoff values of 6 mm and 6 degrees. The quantity "Deviation from maximal MI" measures the distance of search results for a given number of bits from the result associated with the largest MI upon convergence. This quantity helps us appreciate the spread of the search results. The RMS and medial values of displacement and angle with respect to maximal MI solution are tabulated in third and fourth columns of Table 2.

Table 2. Average mismatch upon convergence for six schemes of computing MI.

Number of intensity bits	RMS deviation from perfect solution (mm; degree)	Median deviation from perfect solution (mm; degree)	RMS deviation from maximal MI (mm; degree)	Median deviation from maximal MI (mm; degree)	Number of outliers
8	3.62; 6.98	1.40; 2.54	3.36; 6.88	0.58; 2.11	7
7	1.84; 4.02	1.27; 1.02	1.59; 3.93	0.81; 0.96	5
6	1.84; 1.04	1.08; 0.75	1.45; 0.95	0.56; 0.68	0
5	1.87; 2.45	1.27; 0.95	1.46; 2.40	0.51; 0.86	1
4	2.01; 2.79	1.43; 0.59	1.60; 2.70	0.80; 0.77	2
3	2.23; 4.22	1.16; 0.77	1.95; 4.19	0.54; 0.71	3

Table 3. Average mismatch upon convergence for six schemes of computing MI for temporally filtered frames.

Number of intensity bits	RMS deviation from perfect solution (mm; degree)	Median deviation from perfect solution (mm; degree)	RMS deviation from maximal MI (mm; degree)	Median deviation from maximal MI (mm; degree)	Number of outliers
8	2.17; 4.73	1.47; 0.70	1.85; 4.71	0.35; 0.59	3
7	1.67; 2.40	1.16; 0.51	1.27; 2.38	0.24; 0.45	2
6	1.57; 0.86	1.02; 0.70	1.18; 0.77	0.30; 0.29	0
5	1.64; 0.78	1.03; 0.51	1.26; 0.72	0.35; 0.55	0
4	1.63; 0.85	1.09; 0.54	1.27; 0.80	0.29; 0.41	0
3	1.77; 2.41	1.18; 0.77	1.37; 2.38	0.51; 0.68	1

The same results as presented in Table 2 are presented in Table 3 with the difference that registration was performed on temporally-filtered frames. Improvement in the accuracy of registration is obvious. The number of outliers also went down significantly. From Table 2 and Table 3, is evident that using either 5 or 6 intensity bits to compute MI, together with temporal filtering, produces most accurate results.

It deserves to mention that the value of MI for registered frames for all nine pairs ranged between 0.3 and 0.95 when using all 8 bits, and 0.11 and 0.30 when using 3 bits. This shows data dependency of MI function. An unexpected observation was a slightly larger MI value at the point of convergence than that at the zero point or perfect solution almost all the time. This demonstrates that the search algorithm behaved satisfactorily and that the unevenness of the MI function prevented the search to converge to the perfect solution.

Execution time for each registration equaled the product of time for the evaluation of MI and the total number of these evaluations along the search path. On an average, evaluation of MI took approximately 8 seconds on a 450 MHz Pentium-II processor computer. Most of this time was spent in trilinear interpolation of the secondary. Typically there were 150–250 such evaluations and therefore the total processing time was between 20-30 minutes.

Inter-frameset registration, an example of which is shown Figure 5, was performed although not quantitatively validated. The figure shows three pairs of long-axis views. The middle pair shows two views of the primary. The left pair shows the identical views of the secondary before registration. The right pair shows the same views of the secondary following registration. A visual inspection, at least qualitatively, demonstrates the success of inter-frameset registration.

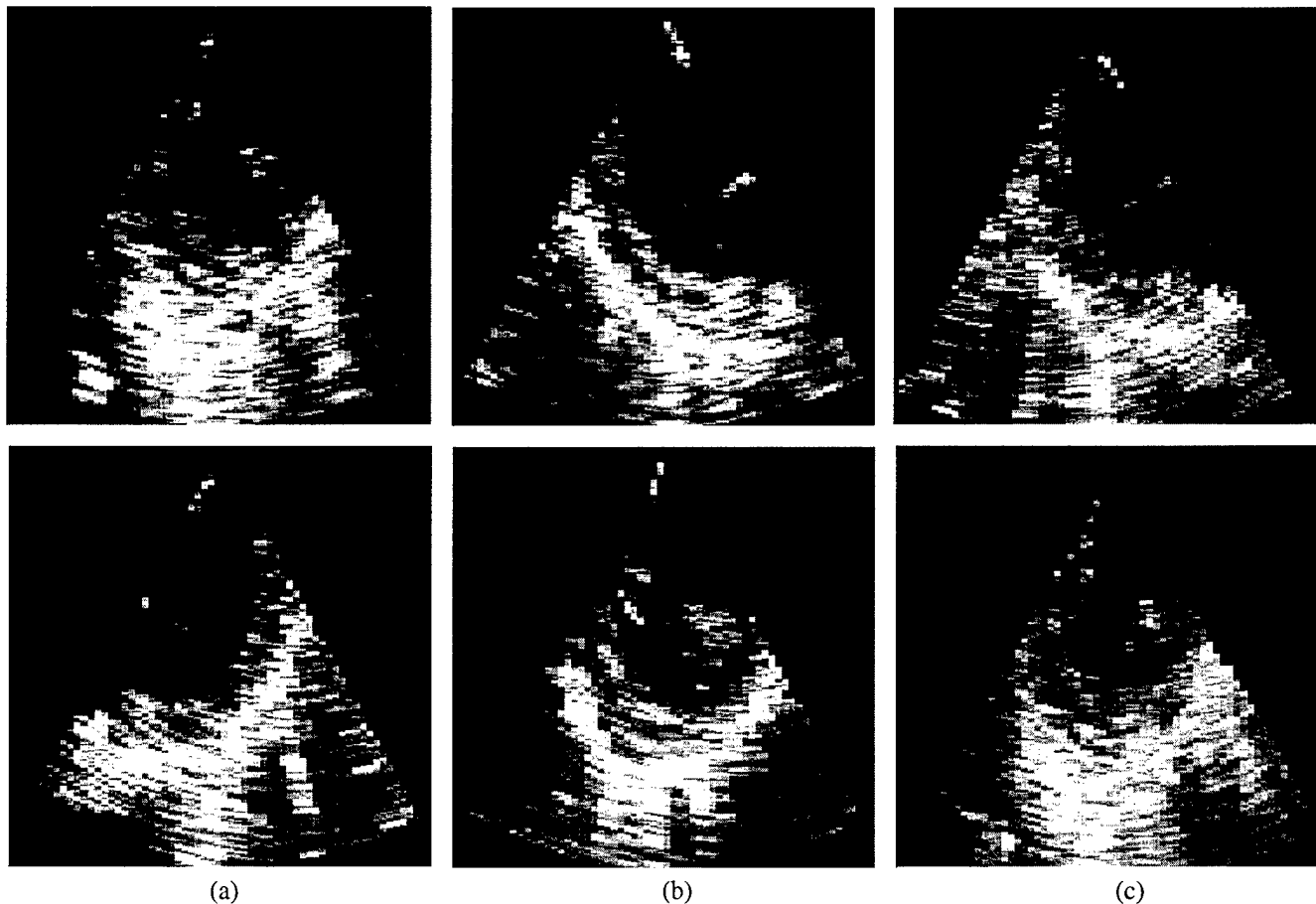


Figure 5. Example of inter-frameset registration: (a) secondary frame before registration, (b) fixed primary frame, and (c) secondary frame after registration. The x-z plane cross-sections are in the upper row and the y-z plane cross-sections in lower.

5. DISCUSSION AND CONCLUSIONS

We have demonstrated that mutual information based registration of ultrasound images is feasible. We have also presented a procedure to compute mutual information such that the success and accuracy of registration is maximized. A quantitative validation of registration was performed using two end diastolic frames from the same frameset. The overall accuracy was of the order of a voxel dimension. The present study provides a good foundation for further investigation and quantitative validation of inter-frameset registration and its application to real life applications.

The computation of mutual information is dependent on individual and joint histograms that in turn depend on voxel intensities. Presence of speckles in ultrasound images appears to cause unevenness in the mutual information function. This unevenness poses two problems: firstly, it can hide or diminish the desired global maximum and, secondly, it creates several local maxima that may confuse the search algorithm. An evidence of this was seen when the MI function did not have a global maximum at perfect solution. Therefore the search algorithm functioned as expected and the error can be attributed to MI function.

Temporal filtering was effective in creating a smoothly varying MI hypersurface as the accuracy of registration improved significantly with it. The intensity binning also had a significant effect on the shape of MI hypersurface and the overall accuracy. The experiments suggested that using five or six upper bits of intensity to compute MI was most effective. A possible explanation is that using all eight bits preserves the speckle noise what corrupts the underlying signal. As the lower bits were discarded gradually signal-to-noise ratio (SNR) first increased due to reduction in noise and then started to decrease due to faster loss of signal than noise. The SNR peaked for five or six bits of intensity. Stated differently, at intermediate levels (5 or 6 bits) the MI function is based on the most salient features of the histograms. At higher levels, noise starts interfering with the features whereas at lower levels salient features start to wash away.

The mutual information based registration does not have an infinite capture range (i.e., the maximum misalignment from which the search algorithm can still converge to the desired solution). If the initial misalignment is large, the convergence may not take place. A misalignment of seven units was large enough to be observable and yet small enough to be within the capture range for our datasets. Since volume of overlap factors into the MI calculation, the MI function can have very high values for very small overlap. Quite clearly, those values do not correspond to the desired solution where a considerable overlap is expected. The search algorithm seeks to converge to the global maximum within this capture range. The capture range is also dependent on the size of the initial pyramid in Nelder-Mead algorithm. However, the size cannot be made arbitrarily large without making the algorithm unstable.

The intra-frameset validation was a good indicator of the accuracy of the overall process. When MI function was computed in the most optimal way, the typical error was of the order of a voxel dimension. Achievement of subvoxel accuracy was beyond the scope of this study. Although we have achieved visually acceptable results of inter-frameset registration, a quantitative validation with expert data is desired.

Encouraged by the results of this preliminary investigation, our future work will focus on inter-frameset registration. We will investigate ways to compute MI function for further accuracy, perform rigorous validation, lower execution time and attempt clinical deployment of the developed methods.

ACKNOWLEDGMENTS

We would like to thank our collaborators Drs. James D. Thomas, Neil Greenberg and Takahiro Shiota of the Department of Cardiology at The Cleveland Clinic Foundation for the 3D ultrasound data used in the present study. We would also like to thank them for their continued support and input.

REFERENCES

1. A. Fenster and D. B. Downey, "3-D ultrasound imaging: A review," *IEEE Eng. Med. Biol.*, **15**(6), pp. 41-51, 1996.
2. J. West, J.M. Fitzpatrick, M.Y. Wang, B.M. Dawant, C.R. Maurer, R.M. Kessler, and R.J. Maciunas, "Retrospective intermodality registration techniques for images of the head: surface-based versus volume-based", *IEEE Trans. on Medical Imaging*, **18**(2), pp.144-150, 1999.

3. J.B.A.Maintz, and M.A.Viergever, "A survey of medical image registration", *Medical Image Analysis*, **2**(1), pp.1-36, 1998.
4. C.Studholme, D.L.G.Hill, and D.J.Hawkes, "Automated three-dimensional registration of magnetic resonance and positron emission tomography brain images by multiresolution optimisation of voxel similarity measures", *Medical Physics*, **24**(1), pp.25-35, 1997.
5. F.Maes, A.Collignon, D.Vandermeulen, G.Marchal and P.Suetens, "Multimodality image registration by maximization of mutual information", *IEEE Trans. on Medical Imaging*, **16**(2), pp.187-198, 1997.
6. C.R.Meyer, J.L.Boes, B.Kim, P.H.Bland, G.L.Lecarpentier, J.B.Fowlkes, M.A.Roubidoux, and P.L.Carson, "Semiautomatic registration of volumetric ultrasound scans", *Ultrasound in Medicine and Biology*, **25**(3), pp.339-347, 1999.
7. J.C.Lagarias, J.A.Reeds, M.H.Wright, and P.E.Wright, "Convergence Properties of the Nelder-Mead Simplex Method in Low Dimensions", *SIAM Journal on Optimization*, **9**(1), pp.112-147, 1998.